Electrohydrodynamic Modeling of Microdroplet Motion in Digital Microfluidic Systems

by

Ali Ahmadi

B.Sc., University of Tehran, 2004
M.Sc., University of Tehran, 2007

A THESIS SUBMITTED IN PARTIAL FULFILLMENT OF
THE REQUIREMENTS FOR THE DEGREE OF

DOCTOR OF PHILOSOPHY

in

The College of Graduate Studies

(Applied Science)

THE UNIVERSITY OF BRITISH COLUMBIA

(Okanagan)

September 2011

Abstract

Digital microfluidic devices provide a new technology platform for controlled motion of small volumes of fluid. These systems can provide high speed microdroplet transport on integrated electrode arrays. The generic nature of these electrode architectures offers versatility, scalability, and reconfigurability that is crucial for biomedical, chemical, and sensing applications.

The structural layout of digital microfluidic devices and the employed electrical activation schemes must be considered together in the design and operation of successful fluid actuation. Microfluidic models provide an effective tool for predicting this device performance and optimizing parameters to achieve high efficiency. Numerical simulation of the electrodynamics of microdroplet motion in digital microfluidic systems will provide better understanding of the effects of electrode shape on actuation forces, actuation voltage/frequency and liquid properties (e.g., conductivity, permittivity, and surface tension) on microdroplet actuation. However, the development of such models is far from trivial as many complex physicochemical phenomena become involved in the transport.

In this thesis, a novel numerical multiphysic approach is used to model the

microdroplet motion in digital microfluidic systems. The actuation force in the system of the interest is provided by applying voltage to the underlying electrodes. The main focus of this study is on the conductive liquids, however the electromechanical approach used in this research cab be readily extended to dielectric liquids. The proposed model employs an electrohydrodynamic approach for estimating the driving, wall and filler forces. Additionally, the effects of the evaporation are considered from two aspects: it is shown that an additional force is needed to balance the dynamic equation of the microdroplet motion, and the microdroplet interface is deformed due to the change in the microdroplet radius. Finally, the effects of the biomolecular adsorption are included by adding a new force to the dynamic equation of the microdroplet motion, and the adsorption rate is then related to the change in the interfacial tensions and the capacitance of the underlying layers. The results of the developed model are presented and verified with experimental data obtained from literature, and it is shown that the model provides an accurate representation of microdroplet transport in digital microfluidic systems.

Preface

This thesis is based on the work conducted at UBC's Digital Microfluidic Laboratory under supervision of Drs. Mina Hoorfar, Jonathan F. Holzman and Homayoun Najjaran. Parts of this thesis have been published in peer reviewed scientific journals and conference proceedings, and my supervisors are the co-authors of all of the publications.

The electrohydrodynamic approach described in the Chapter 3 is published in two journal articles [1, 2], and five conference proceedings [3–7]. I was responsible for developing the methodology, writing the computer program and writing the articles.

The biomolecular adsorption model described in the Chapter 3 is published in one conference proceeding [8]. I was responsible for developing the methodology, writing the computer program and writing the article.

The optimization results presented in the Chapter 4 is published in one journal article [9], and Kurt D. Devlin is one of the co-authors of the paper. I was responsible for developing the methodology, writing the computer program and writing the article, and Kurt D. Devlin was responsible for running the

computer program.

The capacitance sampling and contact angle measurement procedure described in Chapter 3 and Appendix A are based on the collaborative work with an undergraduate student, Kurt D. Devlin. The results obtained from the developed methodology have been published in a journal article [10] and a conference proceeding [11], and Kurt D. Devlin is one of the co-authors of the papers. I was responsible for developing the methodology and designing the experiments and writing the papers, and Kurt D. Devlin was responsible for conducting the experiments, and writing the computer programs.

The conductance sampling procedure described in Appendix B is based on collaborative work with an undergraduate student, Jackie Nichols. The results obtained from the developed methodology have been published in one journal article [12] and two conference proceedings [3, 13], and Jackie Nichols is one of the co-authors of the papers. I was responsible for writing the papers, and Jackie Nichols was responsible for designing the experiments and writing the computer programs.

List of publications

- **A. Ahmadi**, K. D. Devlin, and M. Hoorfar, *Numerical study of the microdroplet actuation switching frequency in digital microfluidic biochips* Microfluid. Nanofluid., 2011,(DOI) 10.1007/s10404-011-0872-8.

- **A. Ahmadi**, J. F. Holzman, H. Najjaran, M. Hoorfar, *Electrohydrody-*

namic modeling of microdroplet transient dynamics in electrocapillary-based digital microfluidic devices, Microfluid. Nanofluid., 10, 1019-1032, 2011.

- **A. Ahmadi**, K. D. Devlin, H. Najjaran, J. F. Holzman and M. Hoorfar, *In situ characterization of microdroplet interfacial properties in digital microfluidic systems*, Lab On a Chip, 10, 1429 - 1435, 2010.

- J. Nichols, **A. Ahmadi**, M. Hoorfar, H. Najjaran and J. F. Holzman, *In situ digital microfluidic conductance sampling*, Sens. Actuators A, 152, 13-21, 2009.

- **A. Ahmadi**, H. Najjaran, J. F. Holzman, and M. Hoorfar, *Two-dimensional flow dynamics in digital microfluidic systems*, J. Micromech. Microeng., 19, 065003-1-065003-7, 2009

- **A. Ahmadi**, and M. Hoorfar, *Numerical investigation of the combined effects of biomlecular adsorption and microdroplet evaporation on the performance of the electrocapillary-based digital microfluidic systems*, Proc. ICNMM2011, ICNMM2011-58166, Edmonton, Canada, 2011.

- **A. Ahmadi**, and M. Hoorfar, *Dynamics of evaporating microdroplets in digital microfluidic biochips*, Proc. CANCAM2011, Vancouver, Canada, 2011.

- **A. Ahmadi**, J. F. Holzman, H. Najjaran, and M. Hoorfar, *Numerical multiphysics modeling of microdroplet motion dynamics in digital*

microfluidic systems, ICNMM2010, FEDSM-ICNMM2010-30754, Montreal, Canada, 2010.

- **A. Ahmadi**, K.D. Devlin, H. Najjaran, J.F. Holzman, M. Hoorfar, *Biomolecular adsorption phenomena in electrowetting-based digital microfluidic devices*, Proc. Nanotech., 2, 452 - 455, Anaheim, USA, 2010.

- K. D. Devlin, **A. Ahmadi**, H. Najjaran, J. F. Holzman, M. Hoorfar, *Dynamic sampling in digital microfluidic devices*, Proc. SPIE, 7679, 76790C, Orlando, USA, 2010.

- **A. Ahmadi**, H. Najjaran, J. F. Holzman, and M. Hoorfar, *Determination of droplet shape in digital microfluidic systems using two-dimensional flow analysis*, Proc. Nanotech., 3, 351 354, Huston, USA, 2009.

- **A. Ahmadi**, J. Nichols, M. Hoorfar , H. Najjaran, and J. F. Holzman, *Digital implementations for integrated microfluidic sensing*, Proc. SPIE, 7318, 73181C, Orlando, USA, 2009.

- **A. Ahmadi**, H. Najjaran, J. F. Holzman, and M. Hoorfar, *Numerical modeling of microdrop motion on digital microfluidic multiplexer*, Proc. Nanotech., 3, 561 564, Boston, USA, 2008.

- J. Nichols, **A. Ahmadi**, M. Hoorfar, H. Najjaran, and J. F. Holzman, *Micro-drop actuation using multiplexer structures*, Proc. ICNMM, 1085-1092, Darmstadt, Germany, 2008.

Table of Contents

List of Tables

List of Figures

Acknowledgements

It is difficult to overstate my gratitude to my Ph.D. supervisors, Drs. Mina Hoorfar, Jonathan F. Holzman and Homayoun Najjaran. Their leadership, enthusiasm, inspiration, support, attention to detail and hard work have set an example I hope to match some day. Throughout this period, they provided encouragement, sound advice, good teaching, good company, and lots of good ideas. For everything you have done for me, I thank you.

I would like to thank the members of my doctoral committee, Drs. Vladan Prodanovic, Deborah Roberts, Rudolf Seethaler, Boris Stoeber, Karen Cheung, Kian Mehravaran, Cedric Saucier and Sushanta Mitra for their input, valuable discussions and accessibility.

This thesis would not have been possible without the support and help of the wonderful staff of UBC. I would like to gratefully and sincerely thank Maria Graziano, Karen Seddon (School of Engineering), Barbara Sobol (Library) and Jennifer Cook (College of Graduate Studies) for their ever willingness to assist.

The members of the research group have contributed immensely to my per-

sonal and professional time at UBC. The group has been a source of friendships as well as good advice and collaboration. Past and present group members that I have had the pleasure to work with or alongside of are Biddut Bhattacharjee, Milad Abolhasani, Mehdi Shahraeeni, Sina Jomeh, Kurt D. Devlin, Matt Buat, Jacqueline Nichols, Chris Collier, Brandon Born and Mike Wiltshire.

My time at UBC was made enjoyable in large part due to the many friends and groups that became a part of my life. I am grateful for time spent with roommates, friends and my soccer buddies. Particularly, I would like to thank Nima (Morteza) Farrokhsiar for being a supportive and kind friend. Nima, thank you for your "beautiful" singing, for making me laugh and for your good company.

My deepest gratitude goes to my family for their unlimited love and support throughout my life; this dissertation is simply impossible without them. I am indebted to my parents who raised me with a love of science and supported me in all my pursuits. I have no suitable word that can fully thank Rafie family for their everlasting love and constant support when I encountered difficulties. Finally, I want to express my deeply-felt thanks to my loving, supportive, encouraging, and patient girlfriend Monica Cella and her family whose faithful support during the final stages of this period is so appreciated.

Dedication

This thesis is dedicated to the memory of my Dad,

Davood Ahmadi (December 1, 1946 - May 10, 2006),

and to realising his hopes and dreams. He will always be loved

and shall forever live on in my heart.

Chapter 1

Introduction

In recent years, there has been a trend toward miniaturization of biomedical and electromechanical devices. One of the obvious advantages of this scaling down, from the decimeter scale to the micrometer scale, is the dramatic reduction in the required sample volumes. For instance, a linear size reduction by a factor of 10^3 results in a volume reduction by a factor of 10^9. Therefore, instead of handling one liter or one milliliter of fluid, a miniaturized system works with volumes as small as one nanoliter or one picoliter. Such small volumes allow for shorter analysis times and efficient detection schemes when large amounts of sample are unavailable. Moreover, the small volumes make it possible to develop compact and portable biomedical systems (known as lab-on-a-chip (LOC) devices) which integrate one or several laboratory functions on a single chip of only millimeter or centimeters scale. LOC systems [17–20] can be considered as the natural generalization of the existing electronic integrated circuits and micro-electro-mechanical systems (MEMS) [21–23]. It is expected that LOC systems will have a great impact in biotechnology, pharmacology, medical diagnostics, forensics, environmental monitoring and basic research. Finally, it is the hope that, similar to

microelectronics, manufacturing costs could be reduced by mass production of these microsystems.

1.1 Microfluidics

The main purpose of a LOC system is to handle fluids. Therefore, LOC systems essentially are microfluidic devices [24, 25]. Microfluidics signifies any kinds of experimental and theoretical research on liquid streams generated in chips comprising microsized channels, including fabrication, handling and practical use of these chips [25]. Microfluidics has developed remarkably over the past few decades. In the 1980s, microfluidics was introduced for accurate control in specific dispensing applications (i.e. ink jet printing). Today, biotechnology industrial sectors are witnessing numerous benefits from the microfluidic systems, as these technologies are well-suited for control of biological samples, aqueous solutions, and microscopic organisms [24–29]. Microfluidic devices have numerous advantages compared to conventional techniques, including reduced sample and reagent volumes, reduced processing costs and time, increased sensitivity levels (due to higher precision and selectivity of the process), and reduced risks associated with the manipulation of toxic or dangerous products. Inherently, these benefits are the result of the enhanced automation and parallelization in microfluidic systems.

Microfluidic technologies have certain well-defined challenges at the present time. The integration and miniaturization of numerous system components,

for example, is proving to be particularly challenging, as many process elements (such as pumps, valves and mixers) must be merged into individual chips. High levels of microfabrication complexity are needed to meet the design goals for this integrated system. In addition, structural challenges associated with micron-scale physics must be overcome, as high operational sensitivities are needed to accommodate reduced sample volumes, and enhanced capillary effects must be accommodated for the increased surface to volume ratio.

The first generation of microfluidic devices is based largely upon continuous flow structures. Design concepts for these first generation of microfluidic devices are basically adopted from macroscopic implementations, with combinations of microfluidic, electric, magnetic, optic, acoustic, and chemical processes performing the required functions. While these processing techniques can be carried out with continuous flow or discrete flow systems, it is discrete flow systems that are of particular interest in this thesis. This new generation of digital or droplet implementations provides enhanced reconfigurability and scalability with reduced sample volumes. This point is particularly evident from the scale in Figure 1.1. It has been shown that microdroplets can be manipulated in series using continuous flow in microchannels (see Figure 1.2) [30]. However, digital microfluidics is a distinct paradigm as each microdroplet can be dispensed, moved, merged and split into smaller microdroplet independently. In other words, each microdroplet can be addressed individually (see Figure 1.3) [31–33]. Moreover, since each

microdroplet acts as a discrete microvessel, reactions are carried out without cross-contamination between samples or reagents. Since digital microfluidics is inherently an array-based technique, it is the best choice for array-based biochemical applications [34–45]. Finally, due to the generalized nature of microdroplet transport, digital microfluidic systems are highly reconfigurable and scalable.

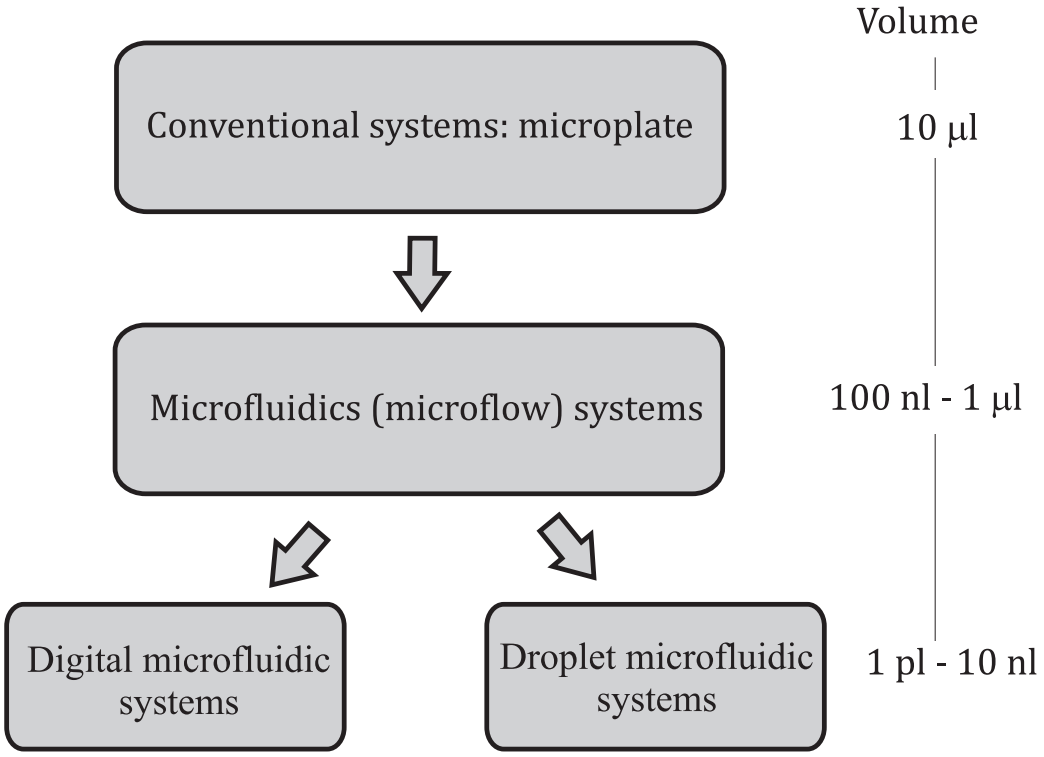

Figure 1.1: Volume scales for various microfluidic systems are shown.

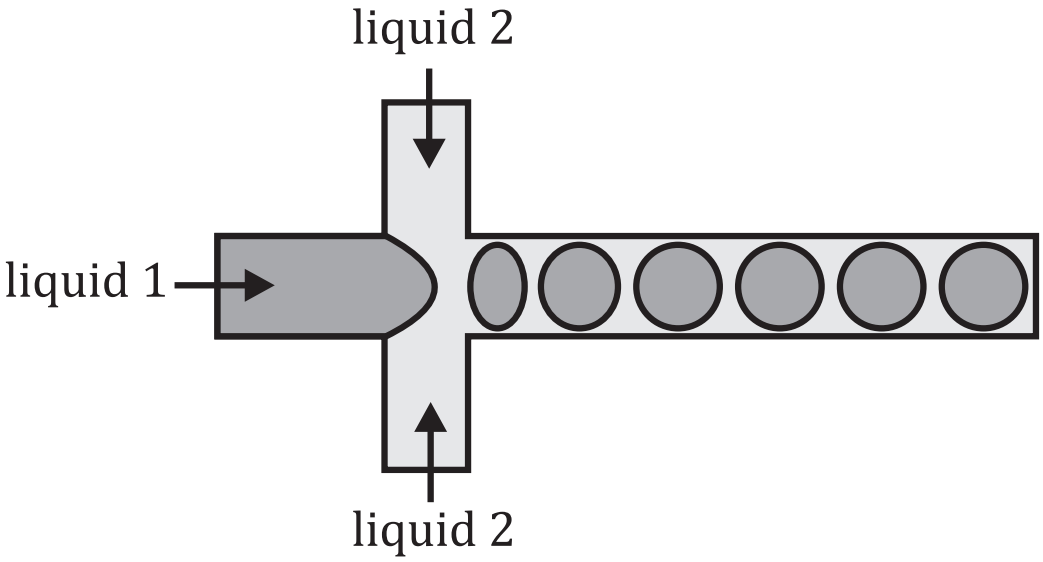

Figure 1.2: A droplet microfluidic system is shown.

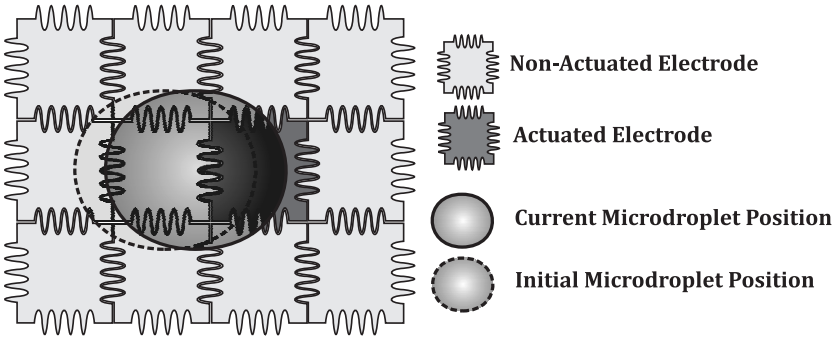

Figure 1.3: Microdroplet transport on electrode arrays is shown.

1.2 Digital microfluidics

Digital microfuidics is a relatively new technique for microscale liquid handling. In essence, digital microfluidic devices transport small volume of

microdroplets (ranging from microliter to picoliter) on arrays of electrodes [31, 32, 46]. Currently, digital microfluidic platforms are employed in a wide range of applications including airborne chemical detection, DNA sequencing by synthesis, and tissue engineering. The advantages of this new platform are reduced sample size, fast heat transfer and reaction rates, and increased integration capacity (for lab-on-a-chip applications).

1.2.1 Device configurations

Typically, there are two configurations for digital microfluidic implementation: closed systems and open systems. In closed systems, which are also known as two-plate systems, the microdroplet is sandwiched between two substrates patterned with electrodes (See Figure 1.4). In open systems, also known as single-plate systems, microdroplets are moving on top of a substrate (See Figure 1.5). To limit the current and power consumption and prevent electrolysis, the actuation electrodes are covered by an insulating layer of a dielectric material. Typically, an additional hydrophobic coating is deposited on top of the insulating layer to make the solid surface hydrophobic and reduce friction.

Both closed and open digital microfluidic configurations have their own advantages. Closed systems show more feasibility for a wide range of microdroplet operations (such as dispensing, moving, splitting, and merging [47]). Typically, in open systems, splitting and dispensing are not possible, and the

evaporation rate is higher. On the other hand, sample and reagent mixing is faster in open configurations [48], and larger microdroplets can be moved in the open systems. Finally, open configurations offer better access to samples for external detectors.

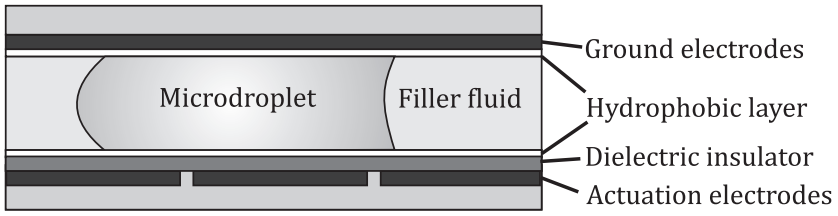

Figure 1.4: A closed (two-plate) digital microfluidic system is shown.

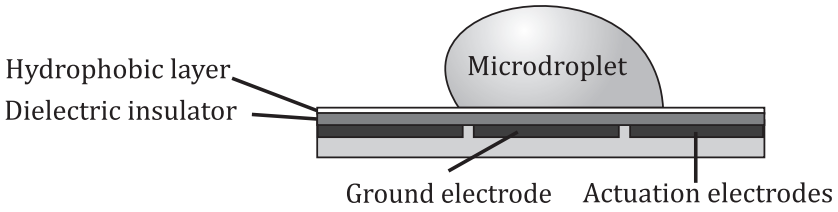

Figure 1.5: An open (single-plate) digital microfluidic system is shown.

1.2.2 Device fabrication

Conventional microfabrication techniques such as photolithography and etching (in a clean-room) are usually used to fabricate the digital microfluidic systems. The most common conductive films on the substrate are chromium, gold, indium-tin oxide (ITO), and doped polysilicon. A variety of techniques,

including vapor deposition (for parylene, amorphous fluoropolymers, and silicon nitride), thermal growth (for silicon oxide), or spin-coating (for PDMS or SU-8) are used to deposit the dielectric layer on top of the electrodes. Teflon-AF is currently the most popular hydrophobic layer which is typically deposited by spin-coating. Most of the current digital microfluidic designs use a liquid filler medium (such as silicone oil) to prevent the evaporation and bimolecular adsorption effects [14]. Liquid filler systems, however, have some drawbacks; normally, gaskets or other structures are required to contain the oil bath. Moreover, analytes can be diffused into the surrounding oil at the liquid-liquid (microdroplet-filler) interface [49]. Additionally, liquid filler systems have been shown to be incompatible with the oil-miscible liquids such as organic solvents [37]. For these cases, the microdroplet transport will be conducted in the air. One of the examples in which the transport in air is required is in proteomics where sample preparation involving the removal of unwanted impurities has been performed in an air medium by drying the sample on the digital microfluidic surface, and then rinsing the surface with a water droplet to dissolve and remove the hydrophobic impurities [37, 50].

Recently, it has been demonstrated that flexible substrates can be used to fabricate the digital microfluidic devices [49]. The new design is based on the microdroplet actuation on nonplanar surfaces which allows for the integration of multiple physicochemical environments on the same device [51]. The new technique uses inexpensive and accessible fabrication methods such as a microcontact printing [52], laser printing [53], and rapid marker masking

[54], which make digital microfluidic technology very accessible.

Electrode density is the main limitation of the all of the above mentioned fabrication methods; to address the electrodes, electrical contacts must be positioned in the limited space between the electrodes. To address this issue, the use of the cross-referenced (multiplexed) electrodes has been proposed [12, 55]. In the proposed design, two sets of linear electrodes are patterned on both the bottom and top plates of a closed digital microfluidic device, and the plates are aligned to be perpendicular to each other. Alternatively, the multilayer printed circuit board (PCB) fabrication can be used to isolate the contact wires from electrodes [56]. As another solution to the electrode density limitation, optically actuated virtual electrodes can replace the hard-wired electrical contacts [57]. In this method, different patterns of light are projected onto a photoconductive substrate, and the desired pattern of electrodes can be actuated. Although the above mentioned designs are more complicated than the conventional designs, they highly increase the scalability of the digital microfluidic systems.

1.2.3 Actuation mechanism

A number of methods have been used for manipulating microfluidic droplets. These techniques can be classified as being based on chemical, thermal, acoustical, and electrical principles.

Gallardo et al. [58] proposed an electrochemical method, whereby a voltage-

controlled, reversible electrochemical reaction is used to create or consume redox-active surfactants (surface-active molecules). This reaction generates a surface-tension gradient along a channel which is capable of driving the liquid droplets through a simple fluidic network. It was observed that the fluid velocity is a function of the applied potential; moderate velocities (2.5 mm/sec) were obtained at low voltages (smaller than 1 V). However, since the electrochemical gradient must be established along the entire length of the channel, this technique (similar to electrokinetic methods used in continuous-flow systems) does not provide a convenient way to independently control multiple droplets.

In another electrochemical method, Ichimura et al. [59] used a photoresponsive surface to generate surface-energy gradients to produce the droplet motion. However, the reported droplet movement velocities of 50 μm/sec are very low, and many liquids (including water) cannot be transported by this technique due to contact-angle hysteresis.

Another type of effect, namely thermocapillarity [60, 61], uses the temperature dependence of surface tension to move the droplet. Thermocapillarity-based systems incorporate multiple (independently) controllable micromachined heaters into a substrate to control multiple droplets. The design and analysis of these systems is complex due to the critical requirement of complete and complicated heat-transfer analysis. However, a relatively high temperature gradient (a differential of 20-40 °C) is needed to achieve a moderate

velocity (e.g., 20 mm/sec). Unfortunately, such large temperature variations are unacceptable for many biochemical applications.

Surface acoustic waves (SAW) [62] can be used to propagate across a piezoelectric substrate (similar to earthquakes), and force the droplets to move on the substrate surface. Using the right signal frequency, a mechanical wave is launched across the chip and the resulting forces (within this nano earthquake) are used to actuate the droplet on the surface. SAW-based technology can also be used to perform droplet mixing as SAW is converted into an internal flow in the droplet. In contrast to diffusion, the internal vortices lead to efficient mixing and stirring within the droplet. Moreover, quasi-chaotic mixing [62] can be obtained by applying different frequencies.

In addition to the above mentioned chemical and thermal methods, electrical methods to actuate droplets have received considerable attention in recent years. Dielectrophoresis (DEP) [63, 64] and electrowetting-on-dielectric (EWOD) [65–78] are the two most common electrical methods. DEP is based on the application of high frequency AC voltages, and EWOD is based on DC (or low-frequency AC) voltages. Both these techniques use electrohydrodynamic forces, and they can provide high droplet speeds with relatively simple geometries.

Liquid DEP actuation is defined as the attraction of polarizable liquid masses into the regions of increasing or decreasing electric field intensity (according to the physical properties of liquid). In the first case, the force is called

positive dielectrophoresis (pDEP), while in the second case it is called negative dielectrophoresis (nDEP). The DEP-based microfluidic systems usually rely on coplanar electrodes patterned on a substrate, coated with a thin dielectric layer, and actuated with AC voltage (typically 200-300 Vrms at 50-200 kHz). Rapid dispensing of large numbers of picoliter-volume droplets and a voltage-controlled array mixer have been demonstrated using DEP [63, 63, 64]. However, excessive Joule heating is recognized to be a challenge for DEP actuation.

EWOD uses DC (or low-frequency AC) electric fields to directly control the interfacial energy between solid and liquid phases [32, 79–82]. Compared to DEP actuation, Joule heating is virtually eliminated as the dielectric layer covering the electrodes blocks DC electric current. As a consequence, aqueous solutions with salt concentrations as high as 0.15 M can be actuated with little heating at a very high speed (up to 250 mm/s [83]).

1.2.4 Biological applications

The digital microfluidic platform is well suited to biological applications with expensive or precious reagents. However, nonspecific adsorption of the biological molecules (which leads to sample loss, cross contamination and increased microdroplet sticking) is the main challenge in the implementation of this new technology. Srinivasan et al. [34] have shown that by suspending the microdroplet in an immiscible oil, fouling can be minimized. The feasi-

bility of the proposed technique was tested for a variety of fluids containing high concentrations of potential surface-fouling molecules, including blood, serum, plasma, urine, saliva, sweat, and tears. Alternatively, to facilitate the actuation of serum and other concentrated solutions, Wheeler et al. [84] proposed the use of low concentrations of amphiphilic polymer (Pluronic F127) (which is a solution additive) as a simple and effective method for limiting the extent of protein adsorption.

In summary, it seems that digital microfluidics is a promising technology for a new generations of biological systems. In the following subsections several examples of biological applications of digital microfluidic systems are described.

DNA extraction, repair, and amplification

Recently, DNA handling, purification, and characterization have been performed using digital microfluidic systems [49]. Aqueous droplets containing a mixture of DNA and proteins were driven into and out of a pool of phenolic oil using all-terrain droplet actuation (ATDA) [49], and as a result, the nucleic acid was purified. Chang et al. [85] developed a digital microfluidic device with an embedded microheater to implement the polymerase chain reaction (PCR). In their work, microdroplets containing an oligonucleotide and PCR reagents were merged, mixed, and then delivered to the integrated heater.

Proteomics and enzyme assays

Although a completely integrated proteomic digital microfluidic setup has not yet been developed, research is underway in this direction. In one of the earliest work, a digital microfluidic setup was developed to purify peptides and proteins from heterogeneous mixtures [35, 86]. Recently, as an important step toward integrated proteomic sample processing, on-chip enzymatic digestion has been demonstrated [84].

Srinivasan et al. [34] demonstrated a fully automated digital microfluidic glucose assay for a range of physiological fluids (serum, saliva, plasma, and urine). In their work, microdroplets containing glucose oxidase were merged and mixed with sample microdroplets spiked with glucose, and finally, the glucose concentration was measured using an integrated LED/photodiode detector.

Cell assays

In recent years, cell-based assay processes have been miniaturized due to the high cost of the reagents and other materials. However, until very recently, cell-based assays have not been considered as a potential application for digital microfluidic systems. This trend changed when cell manipulation was performed successfully on the digital microfluidic chips [87–89]; Zhou et al. [87] showed that the digital microfluidic actuation had no significant effect on cell vitality. Barbulovic-Nad et al. [87] merged microdroplets containing

Jurkat-T cells and microdroplets containing the surfactant Tween 20 (lethal to cells) and viability dyes. In their technique, microdroplets were analyzed using a fluorescence plate reader.

Immunoassays

Recently, analyte detection in biological samples (immunoassays) with high selectivity has been found to be another application for digital microfluidic setups. Sista et al. [90] used the digital microfluidic technique to detect insulin and Interleukin-6. In their work, microdroplets containing magnetic beads (modified with immobilized antibodies) were merged with microdroplets carrying known concentrations of analyte. The beads were separated from the supernatant using a magnetic field, and resuspended in a new microdroplet afterwards. Finally, immobilized analyte was detected by chemiluminescence.

Digital microfluidics is a revolutionary technology which is distinctly different from continuous flow-based microfluidic systems. Of all the potential applications discussed above, proteomics is the most attractive target for digital microfluidic systems. However, it seems that the ultimate killer application [51] may not yet be known as there exist several challenges and unanswered questions about digital microfluidic systems. In fact, a consensus on the physics of microdroplet motion has to be reached by the digital microfluidic community. Numerical simulations of the electrodynamics of microdroplet motion in digital microfluidic systems will provide better understanding of the effects of electrode shape on actuation forces, actuation voltage/frequency

and effects of liquid properties (e.g., conductivity, permittivity, and surface tension) on microdroplet actuation.

1.3 Modeling

The structural layout of digital microfluidic devices and the employed electrical actuation schemes must be considered together in the design and operation of successful fluid actuation systems [91–93]. The physical layout and electrode actuation are closely linked, so one must carefully consider the architecture, materials, and fluid characteristics in developing the appropriate electrode voltage switching algorithm. Ultimately, the optimal actuation scheme will provide rapid droplet transport between neighboring electrodes, while inappropriate control can make continuous droplet motion impossible.

Microfluidic models provide an effective tool for predicting device performance and developing optimal designs. However, the development of such models is far from trivial as many complex physicochemical phenomena become involved in the transport. Driving forces [94] are balanced against opposing forces [15, 95–97]; while threshold voltage conditions [32, 95] and saturation phenomena [98] impede the droplet motion at low and high actuation voltages, respectively. Moreover, for the systems which use air as filler, effects of the evaporation and molecular adsorption on the microdroplet motion have to be considered.

1.4 Previous modeling efforts and their limitations

Given the above challenges in quantifying the electrical/physical characteristics of digital microfluidic architectures, the most recent microdroplet modeling efforts have treated these phenomena in isolation.

In one of the earliest modeling efforts, Ren et al. [95] developed a steady-state transport model for electrowetting-induced microdroplet motion. The developed model was based on the principle of balancing the work done by the capillary force with the energy transformed and dissipated during the microdroplet transport. In their model, they derived the driving force based on the change of the solid/liquid interfacial tension created at the interface between the microdroplet and the insulator due to the applied voltage. The components of energy dissipation were contributed by the viscous flow inside the microdroplet during transport, the microdroplet viscous effect, the filler resistance, as well as the friction around the contact line. Moreover, a threshold initiation force term was added to the dynamic equation to take into account contact angle hysteresis between the front and back of the microdroplet and/or any other static friction (such as friction from adsorption). This constant threshold force represented the decrease in the external force once transport is initiated. This work is a very important benchmark as for the first time the authors identified the critical operating parameters in the performance of electrowetting-based digital microfluidic systems. However,

in their work, all the forces opposing the microdroplet motion were represented by semi-empirical models consisting of multiple fitting parameters, which were obtained from experimental results.

As was mentioned above, Ren et al. [95] identified the key parameters to be the microdroplet and filler viscosity, contact-line friction, system geometry, and surface tension. Most recent modeling efforts have focused on these phenomena in isolation as explained below.

Driving force

Baird and Mohseni [99] studied pressure effects for a variety of actuation forces, including electrowetting on dielectric, continuous electrowetting, dielectrophoresis, and thermocapillary forces. The researchers expressed these actuating forces in terms of pressure differences, although a one dimensional flow was assumed inside the droplet, and an analytical relation was used to consider the hysteresis effects.

Later, Baird et al. [94] used a theoretical and numerical approach to calculate the force distribution on the advancing and receding fluid faces. Dependence of the force distribution and its integral on the system geometry, droplet position, and material properties were described.

Bahadur and Garimella [96] developed an energy-based model for estimating the electrowetting actuation force acting on the microdroplet during its motion. They showed that the results obtained from their model are similar

to those obtained from an electromechanical model. Therefore, the authors concluded that electrowetting-induced droplet motion is essentially an electromechanical phenomenon, rather than being the result of the contact-angle change. In their analytical approach, they combined the actuation force model with semi-empirical models (from Ren et al. [95]) to develop a mean to predict transient microdroplet motion. They investigated the origins and the fundamental physics behind the conductive microdroplet actuation, and used parametric variation to find the conditions which maximize the driving force. In their analytical approach, the size of the conductive microdroplet, however, was restricted to the electrode size, and a simple one-dimensional flow was assumed inside the microdroplet.

To include the effects of the microdroplet size, Bhattacharjee and Najjaran [93] used energy minimization analyses (presented by Bahadur and Garimella [96]), and modeled the digital microfluidic systems for different microdroplet sizes, actuation voltages, dielectric thicknesses and electrode sizes. However, in their work, electrode shapes were assumed to have a simple square geometry.

Kumari et al. [97] used the energy minimization analyses presented by Bahadur and Garimella [96], and developed a model for studying the electrical actuation of dielectric microdroplets.

Chatterjee et al. [100] presented an electromechanical model that enabled calculation of the forces acting on conductive and dielectric liquids in closed

digital microfluidic devices. The device was modeled as an equivalent circuit in which the dielectric layers and filler medium (air or oil) were modeled as capacitors, while the liquid being actuated is described as a resistor and capacitor in parallel. The total electromechanical force and the relative contributions of electrowetting and dielectrophoresis forces on the microdroplet were calculated. However, the effects of the viscous and interfacial forces that impede droplet movement were not included.

Fluid dynamics

In one of the earliest work on modeling electrocapillary dynamics, the dynamics of a liquid slug in a capillary tube was studied [65, 66]. In this work the pressure difference (due to electrowetting along the slug) was approximated using the Poiseuille flow assumption for the central part of the slug. Since Poiseuille flow is fundamentally a one-dimensional flow approximation, an end-correction length for the curvature of the streamlines near the ends of the slug was introduced. Moreover, Young's equation was used to take into account the friction forces at the three phase contact line (with the assumption of linear dependence of the friction force on the average slug velocity).

Kuo et al. [101] modeled the electrowetting-induced pressure gradient in terms of the contact-angle change due to the applied voltage. In their model, the pressure gradient (due to the electrowetting) was used to compute the internal velocity profile and estimate the droplet velocity by solving the Navier-Stokes equation subject to the appropriate boundary conditions. A typical

parabolic flow profile was assumed, and the Navier-Stokes equation was integrated over the directions orthogonal to the flow direction to obtain a spatial average velocity.

Walker et al. [102] presented a partial differential equation model capable of capturing the evolution of the liquid-gas interface in two dimensions. Hele-Shaw type equations including the relevant boundary phenomena were used to model the fluid dynamics.

Fair [103] developed a hydrodynamic scaling model of droplet actuation in a digital microfluidic systems. The proposed analytical model included the effects of the contact angle hysteresis, drag from the filler fluid, drag from the solid walls, and the change in the actuation force while a microdroplet traverses a neighboring electrode. It was shown that reliable operation is possible as long as the device is operated within the limits of the Lippmann-Young equation.

Interface

Walker and Shapiro [104] used the level set method to model droplet motion, mixing and separation phenomena. To simplify the model, they used a Hele-Shaw flow assumption for the viscous flow region of the fluid in the narrow gap between the parallel plates. However, the scope of their work was limited, as the hysteresis and saturation effects were not included in their model.

Clime et al. [105, 106] developed a three-dimensional multiphase Lattice-

Boltzmann model to study basic operations such as transport, merging and splitting of microdroplets actuated by electrowetting in digital microfluidic devices. The model was employed to study the dynamics of the splitting processes at different contact angles and different geometries of the system.

Keshavarz-Motamed et al. [107] investigated the electrowetting phenomenon in parallel plate microchannel, and concluded that ignoring dynamic features of wetting leads to the overestimation of the effect of electrowetting actuation on various parameters including contact angle, aspect ratio and velocity of the droplet.

Electrohydrodynamics

Arzpeyma et al. [108] developed a numerical model based on coupling the hydrodynamic and electrostatic governing equations to investigate the optimum actuation condition. They investigated the effects of the switching frequency on the microdroplet motion and proposed a position-based actuation algorithm for achieving higher microdroplet velocities. They also recognized the limitations of their model in terms of hysteresis effects.

In a recent modeling effort, SadAbadi et al. [109] investigated the effects of electrode switching frequency on the maximum possible microdroplet velocity. They showed that the best time for switching/actuating the next electrode is when the microdroplet leading edge contacts that electrode, and late or early actuation will result in discontinuity in the microdroplet velocity.

1.5 Motivation and purpose of thesis

Currently, electrowetting (EW) or electrowetting-on-dielectric (EWOD) is the most popular actuation technique. The term EWOD was used by the pioneers of the digital microfluidic field [32, 33] and refers to the reduction in the microdroplet contact angle due to the applied voltage. In this scheme, microdroplet motion was understood as being a consequence of capillary pressure arising from non-symmetrical contact angles on either side of the microdroplet. However, the electrowetting description cannot explain the microdroplet actuation for dielectric liquids or for low-surface tension liquids (that show no apparent changes in the contact angle with the applied voltage). Moreover, using the electrowetting description, microdroplet contact-angle saturation and its effects on the microdroplet dynamics cannot be explained. A better understanding of the physics of microdroplet actuation can be derived from an electromechanical analysis [94, 110, 111]. The electromechanical analysis explains the microdroplet actuation force as the electrical force acting on the free charges in the microdroplet meniscus (in the case of conductive liquids) or on the dipoles inside the microdroplet (in the case of dielectric liquids).

Unlike the current digital microfluidic modeling efforts which have focused on some particular aspects of the microdroplet motion in isolation, in this work a novel numerical mutiphysic approach is used to model the microdroplet motion with different aspects mentioned above. The actuation force

in the system of interest is provided by applying voltage to the underlying electrodes. The main focus of this study is on conductive liquids. However, the electromechanical approach used in this research can readily be extended to dielectric liquids. Due to the numerous complex physicochemical phenomena influencing the microdroplet motion, the proposed model has different submodules which are explained briefly here and in detail in Chapter 2.

1.5.1 Dynamics

As described by Ren et al. [95], the most important forces in the microdroplet dynamic equation are the driving force, wall force (due to the solid walls), filler force and contact line force. However, as it will be shown in the present work, for the systems which use air as filler, two additional forces must be added into the dynamic equation to take into account the effects of evaporation and adsorption. In this work, an electrohydrodynamic approach is employed to develop a model for estimating the driving, wall and filler forces. Electrostatic and hydrodynamic governing equations are solved simultaneously, and the obtained electric and velocity fields and the electrostatic and hydrodynamic pressures are then used to calculate the electromechanical driving force, velocity gradient (and the resulting shear force) and the filler drag force. The electromechanical driving force is estimated by integrating the electrostatic pressure along the microdroplet-filler interface. The wall force is calculated by integrating the shear force over the wetted area, and the filler force is obtained by integrating the hydrodynamic pressure along

the microdroplet-filler interface.

1.5.2 Interface

After finding the electrostatic and hydrodynamic pressures, the Laplace law [112] is used to find the curvature of the advancing and receding interfaces. A method based on the fractional volume of fluid (VOF) [108, 113] is developed to model the microdroplet moving boundary. The VOF method is based on the averaging of phases at the interface, in which the volume fraction is advected with the fluid flow. Moreover, the effects of the dynamic contact angle and contact angle saturation are implemented using Frenkel-Eyring activated rate theory of transport in liquids [107, 114].

1.5.3 Evaporation

Although the energy equation is not solved (i.e., the constant temperature assumption), the effects of evaporation are considered from two aspects: 1) it is shown that an additional force is needed to balance the dynamic equation of the microdroplet motion, and 2) at each time step the microdroplet interface has to be deformed due to the change in the microdroplet radius. In the present work, Fick's law [115] is used to relate the mass loss due to evaporation to the curvature of the microdroplet-filler interface. The Laplace law is then coupled with Fick's law to correct the microdroplet boundary condition.

1.5.4 Biomolecular adsorption

The rate of the change in the interfacial tensions is a strong function of the concentration of the solution. This change is very important in applications where the microdroplet carries biomolecules. In such systems, the biomolecule concentration changes due to permanent adsorption to the solid surface and the evaporation, if the air is used as a filler medium. Therefore, the effects of evaporation have to be considered simultaneously with the effects of adsorption. The effects of protein adsorption are modeled by adding a new force to the dynamic equation of the microdroplet motion. The Ward and Tordai equation [116] is used to model the diffusion-controlled protein adsorption. The adsorption rate is then related to the change in the interfacial tensions and the capacitance of the underlying layers.

1.6 Overview

In the following chapters the theory and proposed methodology for modeling the microdroplet motion are explained, and the results obtained from the model are presented and discussed. In Chapter 2 the theory behind the physics of microdroplet motion is explained. Microdroplet motion dynamic equations and electrohydrodynamic governing equations and their boundary conditions are introduced. The developed model for evaporation and biomolecular adsorption are explained, and finally, the algorithm for simultaneous solution of the governing equations is described. In Chapter 3 the de-

tails of the numerical procedure used for solving the governing equations and implementing the boundary conditions are explained. A numerical scheme based on the Finite Volume Method (FVM) used here to solve the governing equations numerically by expressing the partial differential equations in a volume integral form. Discretization is based on the evaluation of volume integrals over small control volumes, and the overall solution is represented by control volume averages. In Chapter 4 the results of the developed model are presented and verified with experimental results, and it is shown that the model provides an accurate representation of digital microfluidic transport. Moreover, an extensive parametric variation is used to derive the Maximum Actuation Switching Frequency for different microdroplet sizes, gap spacings between the top and bottom plates and electrode pitch sizes. As a result of this study, an adjustable force-based actuation switching frequency implementation is proposed, and it is shown that faster microdroplet motion is obtained by in-situ adjusting of the switching frequency. Finally, Chapter 5 concludes this work and lists suggestions for future research.

Chapter 2

Theory

In this chapter, the theory behind the dynamics of the motion of a conductive microdroplet in a covered (electrocapillary-based) digital microfluidic system is studied. The most important physiochemical phenomena (such as electrohydrodynamics, protein adsorption, evaporation) influencing the microdroplet motion are described, and effects of each phenomenon on the microdroplet dynamics are explained.

The system under study consists of a microdroplet sandwiched between two plates (see Figure 2.1). A two-dimensional array of electrodes is patterned on the bottom plate, and both top and bottom plates are covered with dielectric/hydrophobic layers. The incorporated actuation process is largely based upon electrocapillarity [32, 79–82] between underlying electrodes and conductive liquids.

In the following sections, an electromechnical approach is used to derive the driving force (due to the applied voltage to the underlying electrodes) and resisting forces (due to the walls and the filler fluid). Moreover, an electrohydrodynamic approach is presented to include the effects of the biomolecular

adsorption and evaporation in the microdroplet dynamics.

2.1 Electrohydrodynamics

The applied voltage and the resulting electric field have two major effects on the microdroplet kinetics. The first effect is present in the electromechanical driving force acting on the microdroplet-filler interface. In the present work, an electromechanical approach [108, 110, 111, 117] is used to calculate the horizontal force exerted due to the applied voltage to the underlying electrodes. The second effect, on the other hand, is manifested in the change of the shape of the drop-filler interface. The shape of the microdroplet-filler interface is also a function of the hydrodynamic pressure inside and outside the microdroplet. Therefore, the hydrodynamic governing equations have to be solved to obtain the hydrodynamic pressure distribution and the shear and drag forces due to the walls and the filler. In the following subsections, the electrostatic and hydrodynamic governing equations are introduced and the calculation of driving, wall and filler forces are explained. Finally, the coupling of the hydrodynamic and electrostatic solutions are described.

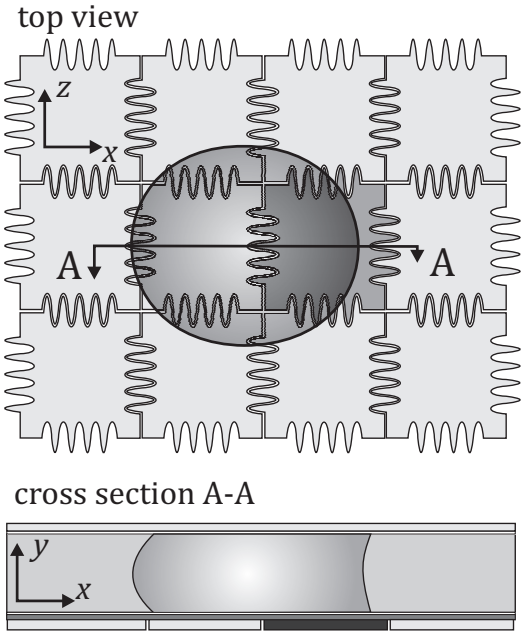

Figure 2.1: Schematic of a covered digital microfluidic system is shown.

2.1.1 Electrostatics

In the presence of an electric field, the net force acting on the microdroplet can be obtained by an integration of the Korteweg-Helmholtz [118] defined by

$$\vec{f_k} = \sigma_s \vec{E} - \frac{1}{2}|\vec{E}|^2 \vec{\nabla}\epsilon + \vec{\nabla}\left[\frac{1}{2}|\vec{E}|^2 \frac{\partial \epsilon}{\partial \rho}\rho\right], \tag{2.1}$$

where $\vec{f_k}$ is the Korteweg-Helmholtz body force density, ρ and σ_s are the mass density and free electric charge density of the media, respectively. Here, $\vec{E}$ is the electric field vector and ϵ is the permittivity of the medium. Since σ_s is zero within a conductive fluid, the first term on the right hand side of the

equation (2.1) disappears. The second term on the right hand side of the equation (2.1) is known as the ponderomotive force density and is proportional to the dielectric constant gradient of the media. This term vanishes everywhere inside the microdroplet, but remains finite at the surface [118]. Since the mass density of the liquid remains constant, the last term in the equation (2.1) describing electrostriction can be neglected.

It has been shown that the integration of the momentum flux density (Maxwell stress tensor [118]) over the surface of the microdroplet leads to the same results as the integration of the equation (2.1) over the microdroplet volume. The Maxwell stress tensor is defined as

$$T_{ij} = \epsilon(E_i E_j - \frac{1}{2}\delta_{ij} E_{kk}), \tag{2.2}$$

where δ_{ij} is the Kronecker delta ($\delta_{ij} = 0$ if $i \neq j$ and $\delta_{ij} = 1$ if $i = j$), and E_i and E_j are the components of the electric field. The net force acting on a volume element (as shown in Figure 2.2) is

$$F_i = \oint_{\partial \mathrm{d}V} T_{ij} n_j \mathrm{d}A, \tag{2.3}$$

where $\partial \mathrm{d}V$ represents the surface of the volume element, $\mathrm{d}V$. For a conductive microdroplet, integrating the Maxwell stress tensor along the surface of the volume element shows that the only nonzero component of the force is

directed along the outward surface normal ($\vec{n}$), with

$$\frac{\mathrm{d}\vec{F}}{\mathrm{d}A} = \frac{\epsilon}{2}(\vec{E}\cdot\vec{E})\vec{n} = \frac{\epsilon}{2}(|\vec{E}|^2)\vec{n}. \tag{2.4}$$

In this relationship, $\mathrm{d}A$ is the element of the surface area of the microdroplet-filler interface. This normal electromechanical force can be expressed by introducing the electrostatic pressure (p_{el}) which has a negative contribution to the total pressure of the liquid as

$$p_{\mathrm{el}} = \frac{\epsilon|\vec{E}|^2}{2}. \tag{2.5}$$

Using the electrostatic pressure definition, the electromechanical force acting on the microdroplet-filler interface, F_{el}, can be expressed as

$$\mathrm{d}\vec{F}_{\mathrm{el}} = p_{\mathrm{el}}\mathrm{d}A\vec{n}. \tag{2.6}$$

Although it has been shown before that the electric field (force) is singular at the three-phase contact line [119], the electrostatic pressure is integrable along the microdroplet-filler interface. The driving (electromechanical) force acting on the microdroplet interface can be calculated by integrating the electrostatic pressure along the microdroplet-filler interface as [1]

$$F_{\mathrm{driving}} = \int \mathrm{d}F_{\mathrm{el},x}, \tag{2.7}$$

in which $F_{\mathrm{el},x}$ is the x-component of the electromechanical force acting on the microdroplet-filler interface, and x is the direction of the microdroplet motion (see Figure 2.1).

To obtain the electrostatic pressure, p_{el}, the electric field has to be found. The electric field is obtained by solving the Maxwell equation [120]

$$\vec{\nabla} \cdot \vec{D} = \vec{\nabla} \cdot (\epsilon \vec{E}) = \vec{\nabla} \cdot (-\epsilon \vec{\nabla} \Phi) = 0, \tag{2.8}$$

where $\vec{D}$ is the electric displacement field vector, and Φ is the electric potential. Note that the equation (2.8) must be solved in three material regions: the dielectric layers, filler and microdroplet interior.

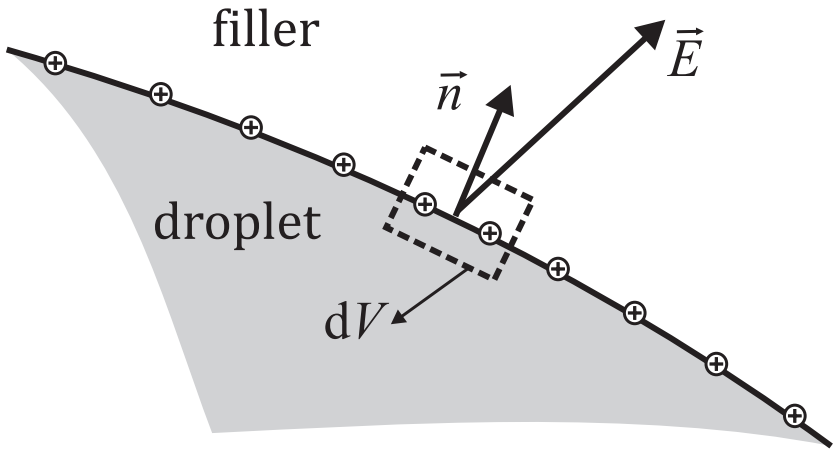

Figure 2.2: Electric force acting on the droplet-filler interface is shown.

2.1.2 Hydrodynamics

To take into account the effects of the microdroplet viscosity (which causes the wall force) and the filler (which causes the drag force), the continuity and Navier-Stokes equations have to be solved in the microdroplet and filler regions. The continuity equation for the incompressible flow is

$$\vec{\nabla} \cdot \vec{v} = 0, \tag{2.9}$$

where $\vec{v}$ is the velocity vector of the fluid particles. The Navier-Stokes equation for the motion of the fluid is

$$\rho[\partial_t \vec{v} + (\vec{v} \cdot \vec{\nabla})\vec{v}] = -\vec{\nabla} p_{\text{hyd}} + \mu \nabla^2 \vec{v} + \rho \vec{g} + \sigma_{\text{s}} \vec{E}, \tag{2.10}$$

where ρ and μ are the fluid density and the viscosity, respectively, $\vec{g}$ is the gravitational acceleration (which is ignored in the digital microfluidic field as the Bond number is smaller than 1 [108]), and σ_{s} is the free charge density. Since the Navier-Stokes equation is solved inside the conductive liquid microdroplet and a dielectric filler fluid, the last term of the equation (2.10) vanishes. While both the velocity and hydrodynamic pressure of the fluid are unknown, it has been shown [121] that the continuity equation (2.9) and Navier-Stokes the equation (2.10) can be solved simultaneously using the numerical methods.

After solving equations (2.9) and (2.10), the velocity vector inside the micro-

droplet is then used to find the wall (shear) force on the wall (F_{wall}) as

$$F_{\text{wall}} = \int_{\text{walls}} \tau \, \mathrm{d}A, \tag{2.11}$$

where τ is the shear stress which is defined as

$$\tau = \mu \left(\frac{\partial u}{\partial y} + \frac{\partial v}{\partial x} \right), \tag{2.12}$$

in which u and v are the x- and y-components of the fluid particle velocities, respectively.

Moreover, using the filler hydrodynamic pressure (which is obtained from the solution of the equations (2.9) and (2.10)) at the microdroplet-filler interface, the filler drag force, F_{filler}, can be calculated as

$$F_{\text{filler}} = \int p_{\text{hyd}} dA_{\text{interface,y}}, \tag{2.13}$$

where $dA_{\text{interface,y}}$ is the projection of the microdroplet-filler interface area element on the y-z plane.

2.1.3 Electrohydrodynamics

Using the Laplace law, the relation between the electrostatic pressure, hydrodynamic pressure and microdroplet surface curvature can be expressed as

[122]

$$[[p_{\mathrm{el}}]]\vec{n} - [[p_{\mathrm{hyd}}]]\vec{n} = \gamma_{\mathrm{df}}(\vec{\nabla}\cdot\vec{n})\vec{n}, \tag{2.14}$$

where $[[p_{\mathrm{el}}]]$ and $[[p_{\mathrm{hyd}}]]$ are the respective electrostatic and hydrodynamic pressure changes across the microdroplet-filler interface, $\vec{n}$ is the normal unit vector to the interface, and γ_{df} is the droplet-filler surface tension. This discontinuity equation can be simplified by noting that the surface force density of the electric origin must have no shearing component [111, 117]. The simplified form of the equation (2.14) can be written as

$$[[p_{\mathrm{el}}]] - [[p_{\mathrm{hyd}}]] = \gamma_{\mathrm{df}}k = \gamma_{\mathrm{df}}\left(\frac{1}{r_1} + \frac{1}{r_2}\right), \tag{2.15}$$

where r_1 and r_2 are the radii of curvature shown in Figure 2.3, and k is the mean curvature. The curvature of the interface can then be extracted from the equation (2.14) by determining the electrostatic pressure from the electric potential and field in the system, and by determining the hydrodynamic pressure from the Navier-Stokes and continuity equations inside the microdroplet and filler.

The boundary conditions used for the microdroplet and filler along the solid surfaces are the no-slip, no-penetration and zero pressure gradient conditions. The microdroplet-filler interface is moving with the microdroplet transport velocity, $v_{\mathrm{transport}}$, and is implemented by defining *fictitious* velocities within solid cells adjacent to fluid cells [123].

A method based on the fractional Volume Of Fluid (VOF) method [108, 113] is used for modeling the moving boundary of the microdroplet. This volume fraction, f, for each small computational grid cell is defined as

$$f = \frac{V_{\text{liq}}}{V_{\text{tot}}}, \tag{2.16}$$

where V_{liq} and V_{tot} are the volume occupied by the liquid and total volume of the computational grid cell (which will be discussed in the next chapter in detail), respectively. The volume fraction function of the cells must satisfy the advection equation

$$[\partial_t f + v_{\text{transport}} \partial_x f] = 0. \tag{2.17}$$

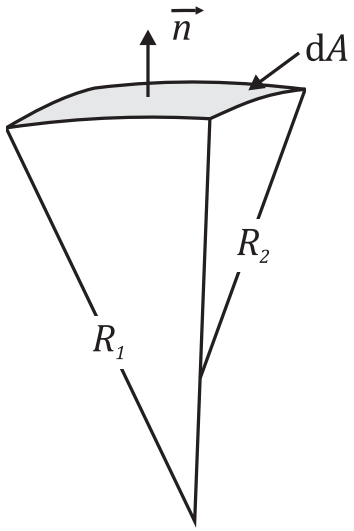

Figure 2.3: Radii of curvature of the microdroplet-filler interface are shown.

2.2 Adsorption

Nonspecific adsorption of the biological molecules, which leads to sample loss, cross contamination and increased microdroplet sticking, is the main challenge in the implementation of the digital microfluidic technology. Most of the current digital microfluidic designs use a liquid filler medium (such as silicone oil) to prevent the evaporation and bimolecular adsorption effects [14]. However, some applications require microdroplet transport in the air. Therefore, to predict the microdroplet behavior in such systems which use air as filler, the effects of the biomolecular adsorption have to be included in the model. Biomolecular adsorption has two major effects on the microdroplet kinetics. The first effect is the change in the interfacial properties of the microdroplet. The second effect is the permanent change of the solid surface (and hence capacitance of the underlying layers) due to the irreversible biomolecular adsorption to the surface. In this section, the physics behind the bimolecular transport inside the microdroplet and adsorption of the molecules to the surface are first explained. The adsorption is then related to the change in the interfacial tensions and the change in the capacitance of the underlying layers. Finally, the changes in the interfacial tension and capacitance are included in the microdroplet kinetics by deriving a new adsorption force.

In the digital microfluidic systems which use air as filler the interfacial tension at the liquid-vapor or solid-liquid interface decreases due to adsorption

of protein molecules. The kinetics of these interfacial tension changes are very complex, since the presence of adsorbed protein molecules, and also the arrangement and conformation of the adsorbed molecules, determine the change in the interfacial tension values. As it can be seen in Figure 2.4, proteins diffuse toward an interface and adsorb. Subsequently, proteins may desorb or undergo conformational changes from their native state to adapt to a state of minimal interfacial tension.

There are two main models for molecule transport and adsorption, and these are shown in Figure 2.5. In these models, a subsurface is taken as an imaginary plane, a few molecular diameters distant from the interface. The models are described as follows:

1. The diffusion controlled model - it assumes the molecules diffuse from the bulk into the subsurface, and once in the subsurface they directly adsorb at the interface. In this model the diffusion process from the bulk to the subsurface is the rate-controlling step, and the timescale of adsorption from the subsurface to the interface is very fast.

2. The mixed kinetic-diffusion model - it assumes that the molecules diffuse from the bulk to the subsurface, but the rate-controlling process is the transfer of these molecules to the interface. Once the molecules have diffused to the subsurface, there may be an adsorption barrier present preventing the molecule from adsorbing. This barrier may be due to an increased surface pressure, or attributed to there being less

vacant sites available for adsorption. There may also be steric restraints on the molecule in the proximity of the interface, and it may have to be in the correct orientation to adsorb. This will cause the molecule to back diffuse into the bulk rather than adsorbing, thereby increasing the timescale of the dynamic surface tension decay.

Since digital microfluidic microdroplet transport is a fast process, the molecular transport can be assumed to be purely a diffusion controlled process (the first model mentioned above). In the following section, the relationship between the biomolecular adsorption process and the change in the interfacial tensions is shown.

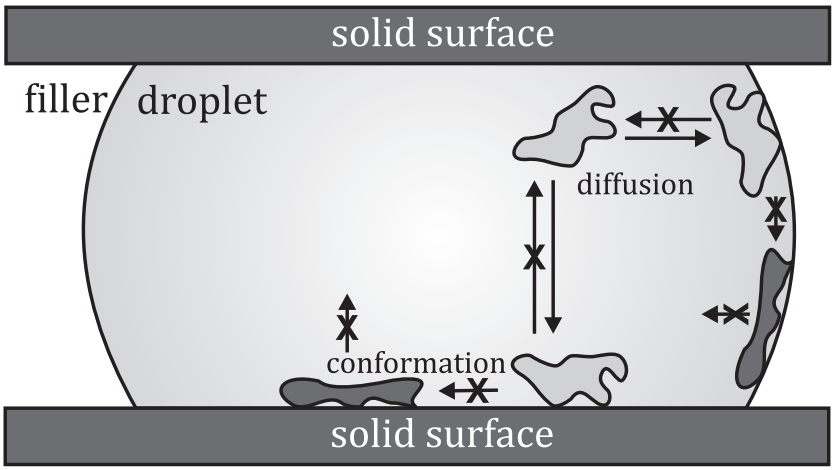

Figure 2.4: Transport of monomer to the interface is shown.

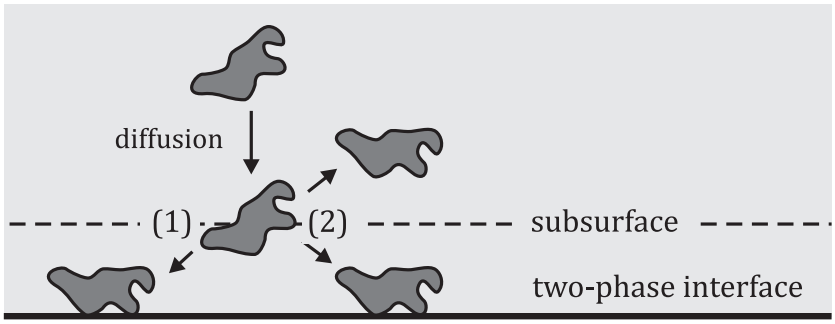

Figure 2.5: Proteins diffuse toward an interface and adsorb. Subsequently, proteins may desorb or undergo conformational changes from their native state to adapt a state of minimal interfacial tension.

2.2.1 Interfacial tension

There are several models available to describe the interfacial tension as a function of the adsorption time [124, 125]. Serrien and Joos [126] proposed a model that accounts for the contributions of both diffusion-controlled adsorption and subsequent conformational changes of adsorbed molecules to the decrease in the interfacial tension value. In this model, adsorption of native protein molecules is assumed to be reversible; while adsorbed molecules may undergo conformational changes that causes an irreversible adsorption state with a rate constant k. Accordingly, the interfacial tension is described by

$$\gamma(t) = \gamma_\infty + [\alpha \exp(-\sqrt{\frac{-4t}{\pi\tau_D}} + \beta] \exp(-kt), \tag{2.18}$$

in which τ_D is the diffusion relaxation time and $(\alpha + \beta)$ represents the maximal change in the interfacial tension, $\gamma(0) - \gamma_\infty$. In this equation α has

been interpreted as the fraction of the the equilibrium interfacial pressure, $\Pi(t) = \gamma(0) - \gamma(t)$, due to diffusion-controlled adsorption, and β is the fraction of the equilibrium interfacial pressure due to the conformational changes at the interface. Equation (2.18) does not account for an adsorption energy barrier and, consequently, τ_D is not related to the real protein diffusion coefficient, but only to an apparent diffusion coefficient including diffusion and adsorption. When the conformational changes at the interface are ignored, i.e., when k and β are set to zero, a simpler equation is derived which accounts for purely diffusion-controlled adsorption. This equation is called the Ward and Tordai equation [116] which accounts for the diffusion of monomers from the bulk to the interface, and also the back diffusion into the bulk as the interface becomes more crowded. At the start of the process, monomers from the subsurface adsorb directly with the assumption being that every molecule arriving at the interface is likely to arrive at an empty site. This is a reasonable postulate for the start of the adsorption process. However, as the surface becomes crowded with the absorbed molecules, there is an increased probability that a monomer will arrive at a site which is already occupied. Back diffusion from the subsurface to the bulk must then be considered. If the subsurface concentration is known, then the diffusion of molecules from the subsurface to the bulk can be treated with Fick's diffusion equations.

The classic Ward and Tordai equation correlating the interfacial tension (or

surface excess, $\Gamma(t)$) to the concentration of the biomolecules is described as

$$\Gamma(t) = 2\mathcal{C}\sqrt{\frac{Dt}{\pi}} - 2\sqrt{\frac{D}{\pi}}\int_0^{\sqrt{t}} \mathcal{C}_s \mathrm{d}\sqrt{t-t'}, \tag{2.19}$$

where D is the diffusion coefficient, t is the adsorption time, $\mathcal{C}$ and $\mathcal{C}_s$ are the protein bulk and subsurface concentration, respectively, and t' is a dummy variable of integration. Including a convolution integral, the equation (2.19) cannot be solved to find back diffusion. However, at the start of the adsorption process there will be no back diffusion (see the crossed processes shown in Figure 2.5). Therefore, the Ward and Tordai equation is simplified to

$$\Gamma(t) = 2\mathcal{C}\sqrt{\frac{Dt}{\pi}}. \tag{2.20}$$

Since the microdroplet transport is very fast, it can be assumed that all molecules arrive at the surface by diffusion, and adsorb irreversibly (perfect sink condition [124, 125]). Thus, the decrease in the interfacial tension is a linear function of the number of adsorbed segments per molecule, and can be described as

$$\Pi(t) = \gamma(0) - \gamma(t) = 2n\mathcal{C}RT\sqrt{\frac{Dt}{\pi}}, \tag{2.21}$$

where $\gamma(0)$ is the initial interfacial tension, and $\Pi(t)$ is the interfacial pressure. In this equation n is equal to 1 for non-ionic surfactants, neutral molecules or ionic surfactants in the presence of excess electrolyte, and is equal to 2 for 1:1 ionic surfactants. The use of the equations (2.20) and (2.21) is justified

as long as the interface acts as a sink. Consequently, linearity between γ and $t^{1/2}$ can only be found at small concentrations or in the beginning of the adsorption process [127, 128]. Also in the case of reversible adsorption, the equation (2.20) is still applicable for the initial stage of the adsorption process. With respect to adsorption kinetics, not only diffusion but also the actual interaction between the protein and the interface (denoted as the reaction component) should be considered. However, in digital microfluidic applications, since the transport time is short, the adsorption can be assumed to be diffusion controlled.

Protein adsorption causes a time dependent change in both the solid-liquid and liquid-vapor interfacial tensions. Using Young's equation, the interfacial tensions can be related to the microdroplet contact angle as

$$\gamma_{\mathrm{lv}}(t)\cos\theta(t) + \gamma_{\mathrm{sl}}(t) - \gamma_{\mathrm{sv}} = 0 \tag{2.22}$$

where $\gamma_{\mathrm{sl}}(t)$, $\gamma_{\mathrm{lv}}(t)$ and γ_{sv} are the solid-liquid, liquid-vapor and solid-vapor interfacial tensions, and $\theta(t)$ is the static contact angle of the microdroplet (see Figure 2.6).

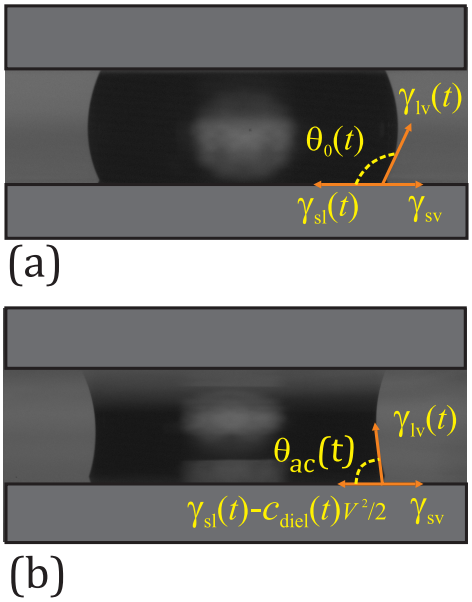

Figure 2.6: The balance of the interfacial tensions (a) before the applied voltage and (b) after the applied voltage are shown.

2.2.2 Capacitance

From an energy perspective, in electrocapillary-based digital microfluidic systems, the driving force is provided by change of the solid-liquid interfacial tension via an applied voltage to the underlying electrode. Using the Lippmann law, the change in the solid-liquid interfacial tension can be determined as

$$\gamma_{\mathrm{sl,ac}} = \gamma_{\mathrm{sl}}(t) - \frac{c(t)V^2}{2} \tag{2.23}$$

where $\gamma_{\mathrm{sl}}(t)$ and $\gamma_{\mathrm{sl,ac}}$ are the solid-liquid interfacial tensions before and after applying voltage, V is the applied voltage and $c(t)$ is the capacitance per unit area of the underlying layer(s) (see Figure 2.6). As it can be seen in Fig-

ure 2.7, in the absence of adsorption the cosine of the contact angle increases from its initial value, $\cos\theta$, to its actuated value, $\cos\theta_{\mathrm{ac}}$, by the amount of $c_0V^2/(2\gamma_{\mathrm{lv0}})$, where c_0 and γ_{lv0} are the capacitance and the liquid-vapor interfacial tension without adsorption (which could be considered as the values for $c(t)$ and $\gamma_{\mathrm{lv}}(t)$ at time zero). However, it has been observed that in the presence of biomolecular adsorption, both θ and θ_{ac} will change with respect to time. The time dependent change of the non-actuated contact angle, $\theta(t)$, is due to the change in the liquid-vapor and solid-liquid interfacial tensions; whereas the change in the actuated contact angle, $\theta_{\mathrm{ac}}(t)$, is due to the change in the liquid-vapor and solid-liquid interfacial tensions as well as capacitance, $c(t)$. If the biomolecular adsorption is included, the change in the capacitance will be due to not only the applied voltage but also the formation of a thin layer of the molecules on top of the dielectric and hydrophobic layer. This layer decreases the total capacitance of the system as

$$c(t) = \frac{1}{1/c_0 + 1/c_{\mathrm{ads}}(t)}, \tag{2.24}$$

where $c_{\mathrm{ads}}(t)$ is the capacitance per unit area of the protein layer on the surface (see Figure 2.8) which can be related to the solid-liquid surface protein concentration, Γ_{sl}, as

$$c_{\mathrm{ads}}(t) = \frac{\Gamma_{\mathrm{sl}}(t)}{\Gamma_{\mathrm{sl}\infty}} c_\infty, \tag{2.25}$$

where $\Gamma_{\mathrm{sl}\infty}$ and c_∞ are the saturated solid-liquid surface protein concentration and capacitance, respectively.

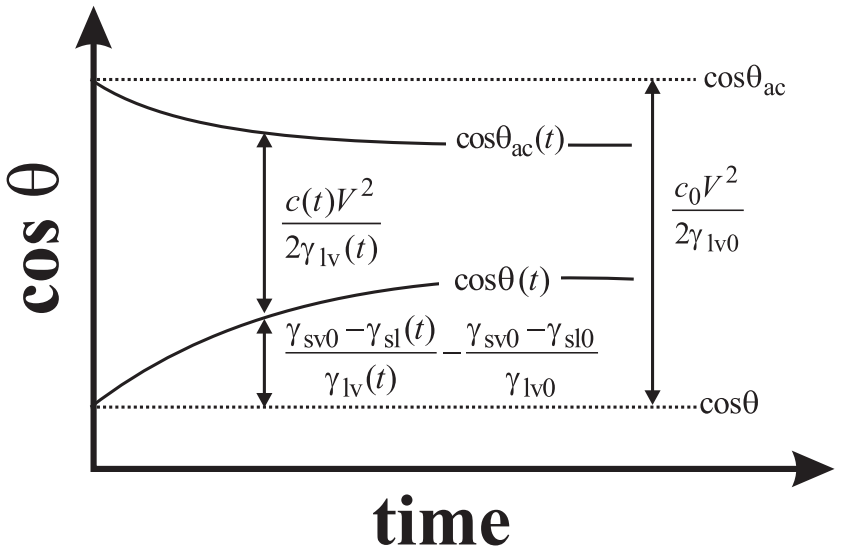

Figure 2.7: Effects of the interfacial tension and capacitance changes on the microdroplet contact angle are shown.

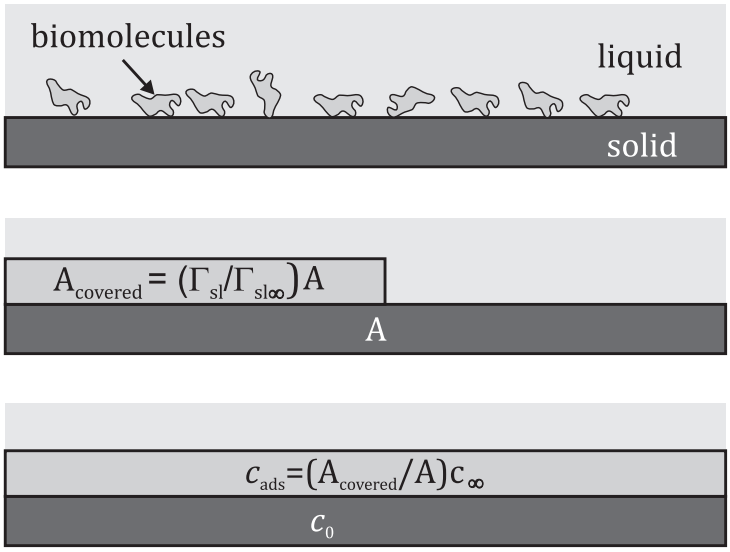

Figure 2.8: The capacitance of the protein layer on the surface is shown.

2.2.3 Adsorption force

The force due to adsorption, F_{ads}, can be derived by using the energy minimization method. The negative derivative of the energy variation due to adsorption provides the adsorption force. Using the Lippmann law the microdroplet free energy, E, can be written as

$$E = \left(\gamma_{\text{sl0}} - \frac{c_{\text{l}}(t)V_1^2}{2} - \Delta\gamma_{\text{sl,ads}}(t)\right) A_1 + \left(\gamma_{\text{sl0}} - \frac{c_{\text{l}}(t)V_2^2}{2} - \Delta\gamma_{\text{sl,ads}}(t)\right) A_2 + \left(\gamma_{\text{sl0}} - \frac{c_{\text{u}}(t)V_3^2}{2} - \Delta\gamma_{\text{sl,ads}}(t)\right) A_3 + \gamma_{\text{df}} A_{\text{df}}(t), \tag{2.26}$$

where γ_{df} is the droplet-filler interfacial tension, and A_{df} is the microdroplet-filler interface area. As it is shown in Figure 2.9, A_1 represents the bottom surface area covering the activated electrode(s), A_2 represents the bottom surface area not covering the actuated electrode(s), and A_3 represents the top surface area of the microdroplet, and V_1, V_2 and V_3 are the voltage differences across each capacitance, respectively. Here, $c_{\text{l}}(t)$ and $c_{\text{u}}(t)$ are the capacitance per unit area of the lower and upper plates. The change in the microdroplet free energy is due to two effects: electrocapillarity [96] and adsorption. Therefore, the microdroplet free energy can be written as

$$E = E_0 - \Delta E_{\text{electrocap}} - \Delta E_{\text{ads}}, \tag{2.27}$$

where E_0 is the initial microdroplet free energy defined as

$$E_0 = \gamma_{\mathrm{sl0}} A_{\mathrm{w}} + \gamma_{\mathrm{lv0}} A_{\mathrm{p}}, \tag{2.28}$$

where A_{w} and A_{p} are the solid-liquid and droplet-filler interface areas. The changes in the microdroplet interfacial energy due to the electrocapillarity, $\Delta E_{\mathrm{electrocap}}$, and adsorption, ΔE_{ads}, are

$$\Delta E_{\mathrm{electrocap}} = \frac{c_{\mathrm{l}}(t) V_1^2}{2} A_1 + \frac{c_{\mathrm{l}}(t) V_2^2}{2} A_2 + \frac{c_{\mathrm{u}}(t) V_3^2}{2} A_3 \tag{2.29}$$

and

$$\Delta E_{\mathrm{ads}} = (\gamma_{\mathrm{sl0}} - \gamma_{\mathrm{sl}}(t)) A_{\mathrm{w}} + (\gamma_{\mathrm{lv0}} - \gamma_{\mathrm{lv}}(t)) A_{\mathrm{p}}. \tag{2.30}$$

The force acting on the microdroplet can be obtained by finding the negative derivative of the microdroplet free energy as

$$F = -\frac{\mathrm{d}E}{\mathrm{d}x} = -\frac{\mathrm{d}(E_0 - \Delta E_{\mathrm{electrocap}} - \Delta E_{\mathrm{ads}})}{\mathrm{d}x}. \tag{2.31}$$

This force can be written as

$$F = -\frac{\mathrm{d}(E_0 - \Delta E_{\mathrm{electrocap}})}{\mathrm{d}x} - \frac{\mathrm{d}(-\Delta E_{\mathrm{ads}})}{\mathrm{d}x}. \tag{2.32}$$

The first term on the right hand side of the equation (2.32) is the original driving force acting on the microdroplet in the absence of adsorption, and it has been shown that it can be obtained using an electromechanical approach

(the equation (2.7)). Therefore, the equation (2.32) can be re-written as

$$F = F_{\text{driving}} - F_{\text{ads}}, \tag{2.33}$$

where the adsorption force, F_{ads} is defined as

$$F_{\text{ads}} = -\frac{\mathrm{d}}{\mathrm{d}x}\left[(\gamma_{\text{sl0}} - \gamma_{\text{sl}}(t))A_{\text{w}} + (\gamma_{\text{lv0}} - \gamma_{\text{lv}}(t))A_{\text{p}}\right]. \tag{2.34}$$

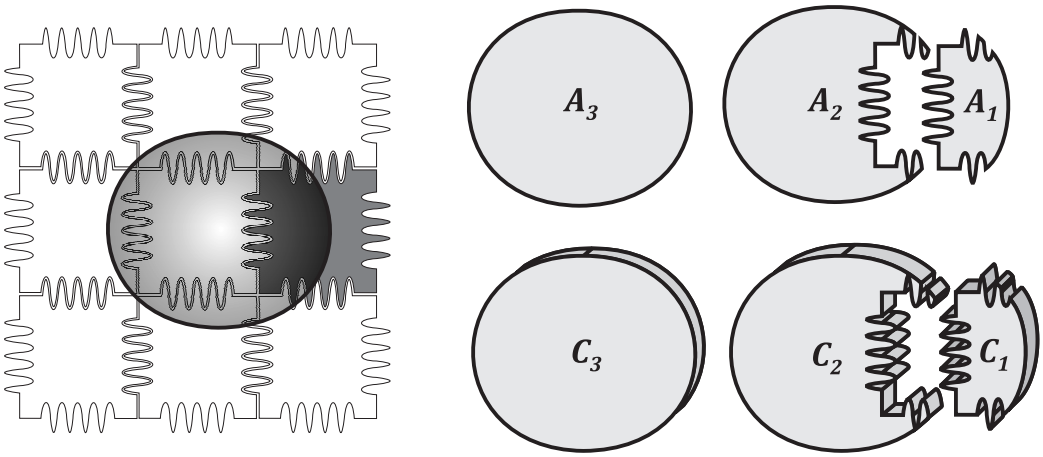

Figure 2.9: Three different areas are shown: A_1 represents the bottom surface area covering the activated electrode(s), A_2 represents the bottom surface area not covering the actuated electrode(s), and A_3 represents the top surface area of the microdroplet.

2.2.4 Protein bulk concentration

It was assumed that all molecules arrive at the surface by diffusion, and adsorb irreversibly (the perfect sink condition [124, 125]). Therefore, the

protein bulk concentration will change due to the adsorption of the molecules to the interfaces. The bulk concentration of the proteins is related to the surface protein concentration, Γ, as

$$\frac{\mathrm{d}(m_{\mathrm{protein}})}{\mathrm{d}t} = \frac{\mathrm{d}(\mathcal{C}V)}{\mathrm{d}t} = \frac{\mathrm{d}((\Gamma_{\mathrm{sl}}(\mathrm{t})\mathrm{A}_{\mathrm{wet}} + \Gamma_{\mathrm{df}}(\mathrm{t})\mathrm{A}_{\mathrm{p}})\mathcal{M})}{\mathrm{dt}}, \tag{2.35}$$

where m_{protein} is the mass of the protein in the microdroplet, and V is the microdroplet volume. Here, Γ_{sl} and Γ_{df} are the solid-liquid and droplet-filler surface protein concentration, and $\mathcal{M}$ is the protein molecular weight.

The rate of change in the interfacial tensions is a strong function of the concentration of the biomolecules. For the systems which use air as a filler medium, however, the biomolecule concentration changes due to two main reasons: 1) adsorption of the molecules to the interfaces and 2) evaporation. Therefore, the effects of evaporation have to be considered simultaneously with the effects of adsorption. In the following sections, the effects of evaporation on the microdroplet dynamics are modeled and described.

2.3 Evaporation

Although the evaporation theory was introduced in the 1910s, a more complete understanding of the evaporation process of microdroplets has just recently been obtained. It has been observed experimentally [129] that wetting and non-wetting droplets do not evaporate in the same way. As it is shown

in Figure 2.10, in the case of a hydrophilic droplet the contact radius remains constant during the evaporation process (except at the very end, when a very small amount of the drop volume remains). This phenomenon is attributed to contact line pinning. In the case of a hydrophobic droplet, on the other hand, the contact angle remains constant (except at the very end of the evaporation process). It has been shown that in both cases, the mass flow rate of liquid loss is proportional to the height of the drop [129, 130]. In the case of a wetting substrate the contact angle decreases linearly with time; whereas in the case of a non-wetting substrate the droplet radius decreases as the square root of time [131].

In digital microfluidic applications, however, the microdroplet evaporation is more complicated as the microdroplet shows both hydrophobic and hydrophilic behavior. Moreover, a different trend in contact angle (and radius) changes is expected due to microdroplet motion and the resulting pinning and dynamic contact angle effects. Finally, due to the mass loss during evaporation, the microdroplet dynamics must be re-considered, and an additional force due to evaporation has to be added to the force balance equation.

Using Fick's law, the evaporation rate for the microdroplet can be obtained as [115]

$$\frac{\mathrm{d}m}{\mathrm{d}t} = -D_v \int \nabla \mathcal{C}_v \cdot \mathrm{d}\vec{S}, \tag{2.36}$$

where D_v is the diffusion coefficient of the vapor and $\mathcal{C}_v$ is its concentration. Equation (2.36) can be developed under the form of

$$\frac{\mathrm{d}m}{\mathrm{d}t} = -D_v \int \frac{\partial \mathcal{C}_v}{\partial n} \mathrm{d}S, \tag{2.37}$$

where n is the direction normal to the microdroplet-air interface.

Most of recent studies have focused on calculating the concentration gradient for a spherical microdroplet [115, 130, 131]. Due to the spherical isotropy, the gradient of the vapor concentration is uniform. Using the boundary conditions of $\mathcal{C}_v = \mathcal{C}_{v\infty}$ at $r \to \infty$, and $\mathcal{C}_v = \mathcal{C}_{v0}$ at $r = r_d$, and taking into account that the diffusion profile around a sphere varies as $1/r$, the concentration gradient can be approximated by [115]

$$\frac{\partial \mathcal{C}_v}{\partial n} = -\frac{\mathcal{C}_{v0} - \mathcal{C}_{v\infty}}{r_d}, \tag{2.38}$$

where r_d is the radius of the spherical liquid drop, and $\mathcal{C}_v = \mathcal{C}_{v0}$ and $\mathcal{C}_{v\infty}$ are the concentrations of the vapor at the droplet-vapor interface (saturated vapor at the temperature of the drop) and far from the interface, respectively. However, in the covered digital microfluidic systems (see Figure 2.11), the microdroplet shape cannot be assumed to be spherical. To address this issue, in the present work it is assumed that the concentration gradient is directed

radially outward and equal to

$$\frac{\partial \mathcal{C}_v}{\partial n} = -(\mathcal{C}_{v0} - \mathcal{C}_{v\infty})\frac{k}{2}, \tag{2.39}$$

where k is the mean curvature of the interface, and can be expressed as

$$k = \frac{1}{r} + \frac{1}{R}, \tag{2.40}$$

where R is the microdroplet radius, and r is the interface radius of curvature in the $x - y$ plane. The curvature of the interface can be extracted from Laplace law by determining the electrostatic pressure from the electric potential and field in the system and the hydrodynamic pressure from the Navier-Stokes and continuity equations inside the microdroplet and the filler as

$$[[p_{\mathrm{el}}]] - [[p_{\mathrm{hyd}}]] = \gamma_{\mathrm{df}} k = \gamma_{\mathrm{df}}(\frac{1}{r} + \frac{1}{R}). \tag{2.41}$$

Therefore, the microdroplet evaporation rate can be obtained as

$$\frac{\mathrm{d}m}{\mathrm{d}t} = -\frac{2D}{\gamma_{\mathrm{df}}} \int -(\mathcal{C}_{v0} - \mathcal{C}_{v\infty})([[p_{\mathrm{el}}]] - [[p_{\mathrm{hyd}}]])\mathrm{d}S. \tag{2.42}$$

Finally, the evaporation force, F_{evp}, is introduced as

$$F_{\mathrm{evp}} = \frac{\mathrm{d}m}{\mathrm{d}t} v_{\mathrm{transport}}. \tag{2.43}$$

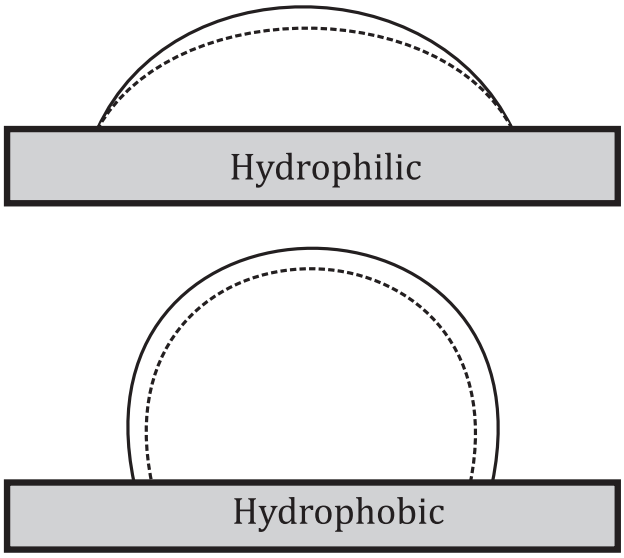

Figure 2.10: Evaporation schemes for hydrophilic and hydrophobic droplets are shown.

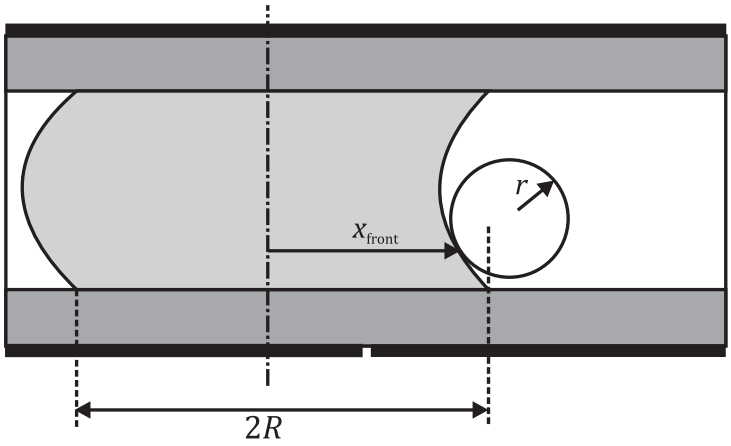

Figure 2.11: The implementation of Laplace Law for the advancing face is shown where R is the radius of the microdroplet, and r is the radius of curvature of the interface in the $x - y$ plane.

2.4 Multiphysics

In the previous sections, the effects of the electrohydrodynamics, adsorption and evaporation were included to model the *ideal* behaviour of the microdroplet. However, it has been shown that due to the microscopic surface defects and roughness and dissipation effects in the submillimeter liquid phase, additional effects have to be included in the model. In the following subsection the implementation of the three-phase contact line force, dynamic contact angle and hysteresis effects are explained.

2.4.1 Three-phase contact line force

The molecular-kinetic theory [114] states that the attachment or detachment of fluid particles is the main source of energy dissipation at the moving three-phase contact line. Although dynamics of wetting can be described by the microdroplet velocity and the dynamic contact angle [107, 114], it was shown [15, 95] that an additional force has to be added to the dynamic equation of the microdroplet motion. Using the molecular-kinetic theory, this three-phase contact line force can be expressed as

$$F_{\text{tpcl}} = 2P\xi v_{\text{transport}}, \tag{2.44}$$

where P is the perimeter length of the microdroplet, and ξ is the friction factor. This linearly dependent friction force is especially accurate at low

and intermediate velocities [15, 95].

2.4.2 Microdroplet dynamic contact angle

It is shown that the contact angle of a moving microdroplet (dynamic contact angle) differs from its static value (static contact angle) at equilibrium [107, 114]. Using Frenkel-Eyring activated rate theory of transport in liquids [107, 114], the static contact angle, θ_{S}, and the dynamic contact angle, θ_{D}, can be related to the microdroplet transport velocity as

$$\cos\theta_{\mathrm{S}} - \cos\theta_{\mathrm{D}} = \frac{v_{\mathrm{transport}}\xi}{\gamma_{\mathrm{df}}}. \tag{2.45}$$

2.4.3 Threshold condition

It has been shown before that there exists a threshold force caused by pinning and hysteresis which prevents droplet motion prior to a sufficient applied voltage [132]. However, implementing the threshold condition to the proposed algorithm is not a trivial task. Most of recent modeling efforts propose the subtraction of a constant threshold force from the driving force [15, 95–97]. However, since the threshold force cannot be greater than the driving force, subtracting a constant threshold force leads to inaccurate results. Therefore, in this thesis the hysteresis condition is implemented by considering an effective voltage as

$$V_{\mathrm{eff}} = \sqrt{V_{\mathrm{app}}^2 - V_{\mathrm{tr}}^2}, \tag{2.46}$$

where V_{eff} and V_{tr} are the effective and the threshold voltage, respectively.

2.5 Dynamics

Taking into account the effects of electrohydrodynamics, evaporation and adsorption in microdroplet dynamics, the governing transient equation for the microdroplet in the direction of the motion can be written as

$$m\frac{\mathrm{d}v_{\text{transport}}}{\mathrm{d}t} = F_{\text{driving}} - F_{\text{wall}} - F_{\text{tpcl}} - F_{\text{evp}} - F_{\text{ads}}, \tag{2.47}$$

where m is the mass of the microdroplet, $v_{\text{transport}}$ is the microdroplet transport velocity, and F_{driving}, F_{wall}, F_{tpcl} are the driving, wall and three-phase contact line forces. Two new forces, F_{evp} and F_{ads}, are added to compensate for the effects of evaporation and adsorption.

It is important to note that the microdroplet transport velocity, $v_{\text{transport}}$, must be known for implementing accurate boundary conditions to the equations (2.9) and (2.10). A dilemma arises here as, in calculating the transport velocity from the equation (2.47), equations (2.9) and (2.10) have to be solved first to find the accurate shear and filler forces acting on the microdroplet, F_{wall} and F_{filler}. With this in mind, an iterative numerical procedure is proposed here for solving the hydrodynamic equations (2.9) and (2.10) and electrostatic equation (2.8) and linking these solutions to the transport described by the equation (2.47). In the proposed iterative algorithm, at

each time step, the electrostatic and hydrodynamic equations are numerically solved simultaneously using the Finite Volume Method (FVM). As a result, the electrostatic and hydrodynamic pressures, and hence the new shape of the microdroplet is calculated. In the next step, the driving force, resisting forces, adsorption and evaporation forces are calculated. Moreover, the change in the microdroplet radius due to the evaporation is calculated. Equation (2.47) is now solved to find the transient velocity of the microdroplet. Finally, the transient velocity is used in a Volume Of Fluid (VOF) based method to model the moving boundary of the microdroplet. The algorithm used for these analyses is shown in Figure 2.12, and the details of the numerical procedure for solving the governing equations are explained in the following chapter. .

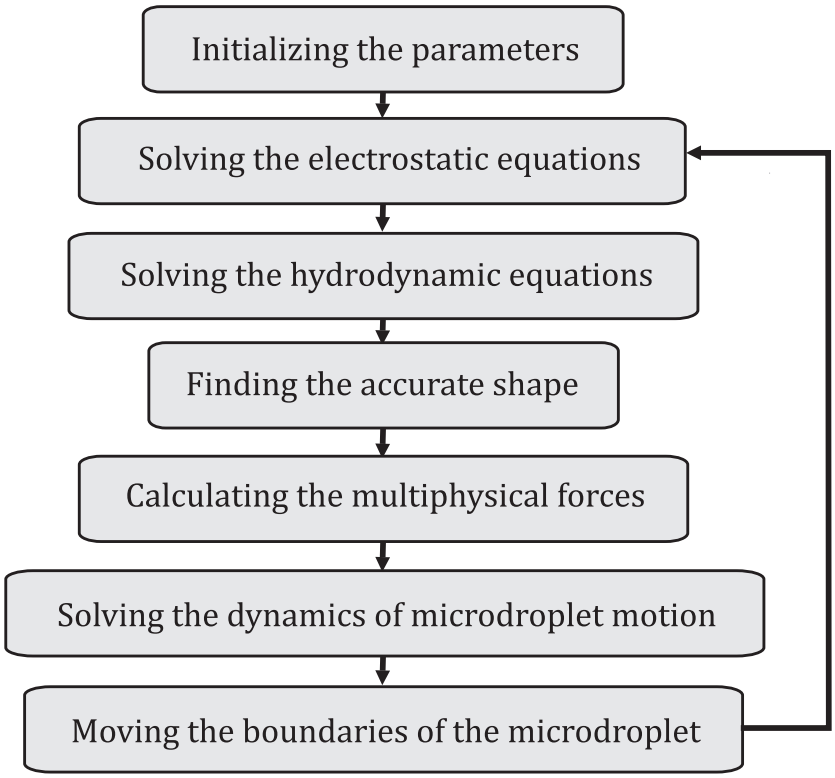

Figure 2.12: The flowchart of the numerical algorithm is shown.

Chapter 3

Methodology

In this chapter, the numerical procedure used for solving the overall electro-hydrodynamic equations is explained. The Finite Volume Method (FVM) is used here to numerically solve the electrostatic and hydrodynamic governing equation by expressing the partial differential equations (PDEs) in a volume integral form. Discretization is based on the evaluation of volume integrals over small control volumes, and the overall solution is represented by the control volume averages.

It has been shown before [15, 133] that velocity fields inside the microdroplet deviate from the parabolic assumption used in most recent modeling efforts [96, 102]. As it is shown in Figure 3.1, although significant recirculation has been observed near the microdroplet interface, streamlines are parallel far from the interfaces [133]. Therefore, a pseudo-three-dimensional approach [15] is employed in this work (see Figure 3.2 and Figure 3.3), and a standard two-dimensional grid is used for the FVM solution of the equations in the meridian plane (cross section A-A in Figure 3.1). Governing equations are solved in the meridian plane, and the microdroplet is analyzed as a collection of planes parallel to this meridian plane. This analysis is carried out

in dimensionless form such that the solution for the meridian plane can be extended to all the planes.

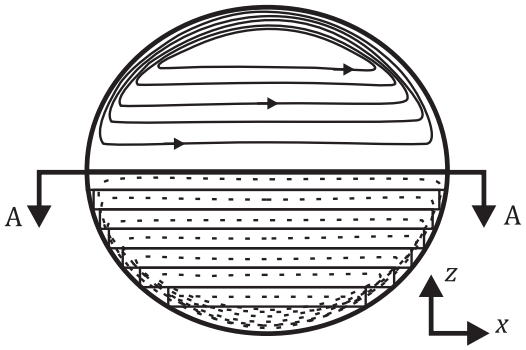

Figure 3.1: It is shown that although significant recirculation has been observed near the microdroplet interface, streamlines are parallel far from the interfaces.

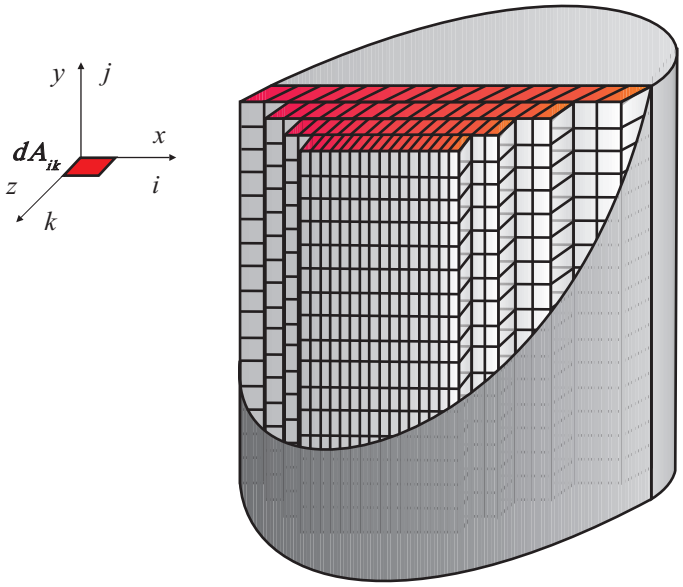

Figure 3.2: Schematic of discretization of the microdroplet is shown. Elements for calculating shear force are shown.

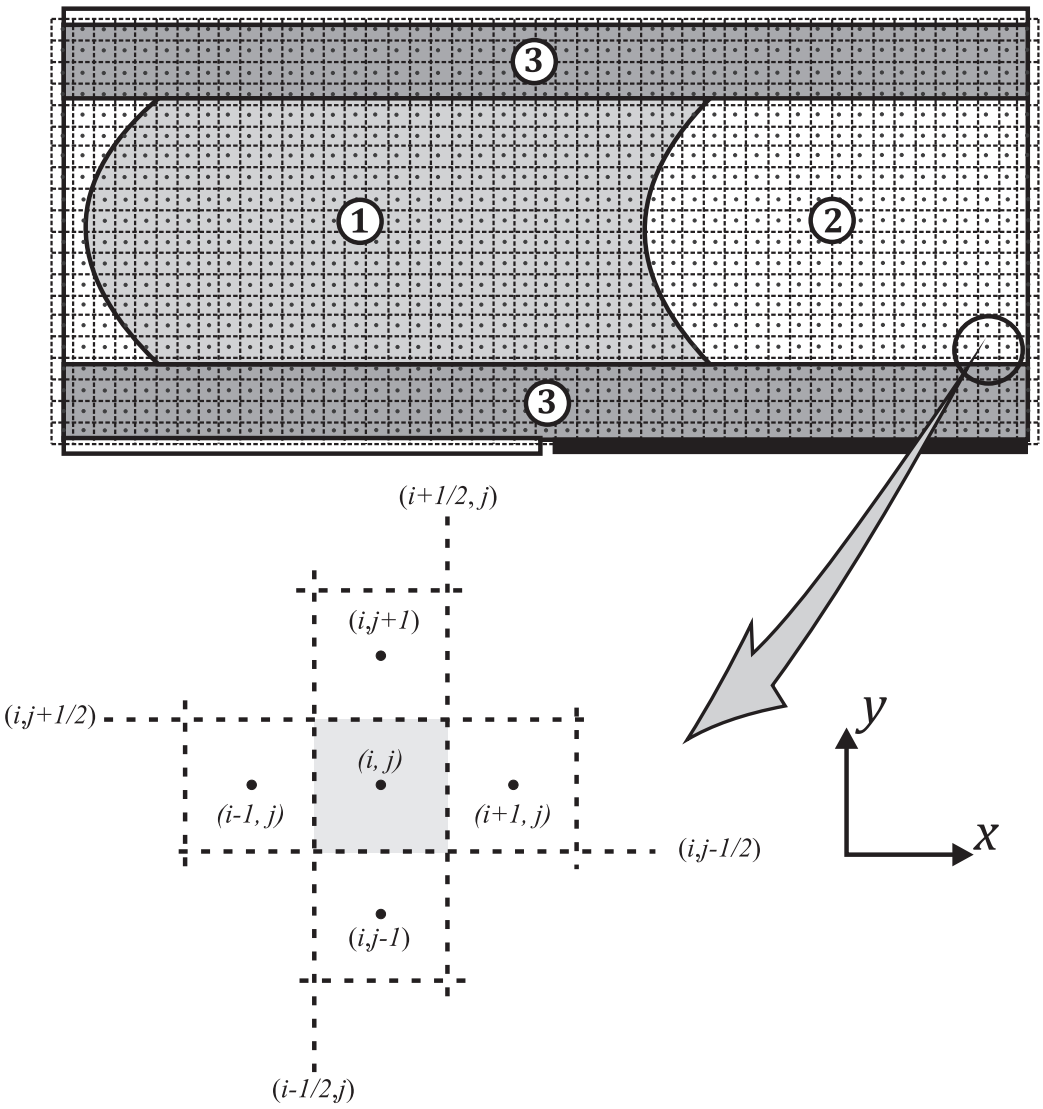

Figure 3.3: The discretized regions of the digital microfluidic system are shown: microdroplet (region 1), filler (region 2) and dielectric layers (region 3). Black circles show the center of each cell, and the dashed lines show the borders of each cell.

3.1 Hydrodynamics

3.1.1 Discretization scheme

The incompressible Navier-Stokes equations are mathematically complicated as they are a coupled system of non-linear elliptic partial differential equations (PDEs). There are a reasonably large number of similarity transformations that can be applied to these equations. Furthermore, the continuity equation is physically not an evolution equation but a partial differential constraint on the velocity field.

The combination of these attributes makes the incompressible Navier-Stokes equations difficult to solve numerically. There are a number of approaches for solving this system, each characterized in a way that the continuity equation is satisfied.

In the present work, the artificial compressibility method is used to satisfy the continuity equation. The artificial compressibility method adds a physical time derivative of pressure to the continuity equation. This derivative is scaled by a parameter β that effectively sets the pseudo-compressibility of the fluid. The addition of the time derivative of the pressure couples the continuity equation more tightly to the momentum equations and allows us to advance pressure and velocity in time together. It should be noted that the right choice of the parameter, β, is very crucial, as it affects the final solution of a problem. In this work, the artificial compressibility value, β,

is chosen according to the mesh size and numerical parameters to accelerate the convergence of the procedure.

The non-dimensional continuity and Navier-Stokes equations in artificial compressibility form can be written as

$$\frac{\partial p^*}{\partial t} + \frac{1}{\beta}\frac{\partial u^*}{\partial x^*} + \frac{1}{\beta}\frac{\partial v^*}{\partial y^*}, \tag{3.1}$$

$$\frac{\partial u^*}{\partial t} + \frac{\partial u^{*2}}{\partial x^*} + \frac{\partial u^* v^*}{\partial y^*} = -\frac{\partial p^*}{\partial x^*} + \frac{1}{Re}\left(\frac{\partial u^{*2}}{\partial x^{*2}} + \frac{\partial u^{*2}}{\partial y^{*2}}\right) \tag{3.2}$$

and

$$\frac{\partial v^*}{\partial t} + \frac{\partial u^* v^*}{\partial x^*} + \frac{\partial v^{*2}}{\partial y^*} = -\frac{\partial p^*}{\partial y^*} + \frac{1}{Re}\left(\frac{\partial v^{*2}}{\partial x^{*2}} + \frac{\partial v^{*2}}{\partial y^{*2}}\right), \tag{3.3}$$

where p^* is the dimensionless hydrodynamic pressure, Re is the Reynolds number, and u^* and v^* are the x- and y-components of the dimensionless velocity vector which are defined as

$$\begin{aligned} u^* &= \frac{u}{L_{\text{ref}}} \\ v^* &= \frac{v}{L_{\text{ref}}} \\ p^* &= \frac{p}{\rho V_{\text{ref}}^2} \\ Re &= \frac{\text{inertia}}{\text{viscosity}} = \frac{\rho V_{\text{ref}} L_{\text{ref}}}{\mu}, \end{aligned} \tag{3.4}$$

where ρ and μ are the density and viscosity of the fluid, and V_{ref} and L_{ref} are the reference velocity and length.

Equations (3.1)-(3.3) can be re-written as

$$\frac{\partial U}{\partial t} + \frac{\partial F}{\partial x} + \frac{\partial G}{\partial y} = 0, \tag{3.5}$$

where

$$U = \begin{pmatrix} p^* \\ u^* \\ v^* \end{pmatrix} \quad F = \begin{pmatrix} \frac{u^*}{\beta} \\ u^{*2} + p^* - \frac{1}{Re}\frac{\partial u^*}{\partial x^*} \\ u^* v^* - \frac{1}{Re}\frac{\partial v^*}{\partial x^*} \end{pmatrix} \quad G = \begin{pmatrix} \frac{v^*}{\beta} \\ u^* v^* - \frac{1}{Re}\frac{\partial u^*}{\partial y^*} \\ v^{*2} + p - \frac{1}{Re}\frac{\partial v^*}{\partial y^*} \end{pmatrix}. \tag{3.6}$$

Equation (3.5) can be written in a vector form as

$$\frac{\partial U}{\partial t} + \vec{\nabla} \cdot \vec{P} = 0, \tag{3.7}$$

where $\vec{P}$ is defined as

$$\vec{P} = F\hat{i} + G\hat{j}. \tag{3.8}$$

In this equation, $\hat{i}$ and $\hat{j}$ are the unit vectors in the x- and y-direction. Equation (3.5) can be integrated over the two-dimensional control volume shown in Figure 3.3. Therefore, it can be written as

$$\int_{\mathrm{CV}} \frac{\partial U}{\partial t} \mathrm{d}V + \int_{\mathrm{CV}} \vec{\nabla} \cdot \vec{P} \mathrm{d}V = 0. \tag{3.9}$$

Now the divergence theorem can be used to convert the second integral in the equation (3.9) to surface integral over boundaries of the control volume

as

$$\int_{\mathrm{CV}} \frac{\partial U}{\partial t} \mathrm{d}V + \int_{\partial \mathrm{CV}} \vec{P} \cdot \hat{n} \mathrm{d}A = 0, \tag{3.10}$$

where $\hat{n}$ is the outward unit normal vector, and ∂CV represents the boundaries of the control volume CV. The implementation of the equation (3.10) is shown in Figure 3.4, and this equation can be written in a discrete form for the control volume cell (i, j) as

$$\begin{aligned} \frac{\partial U_{i,j}}{\partial t} \Delta x \Delta y = \vec{P}_{i+\frac{1}{2},j} \cdot \vec{n}_{i+\frac{1}{2},j} \Delta y + \vec{P}_{i-\frac{1}{2},j} \cdot \vec{n}_{i-\frac{1}{2},j} \Delta y + \\ \vec{P}_{i,j+\frac{1}{2}} \cdot \vec{n}_{i,j+\frac{1}{2}} \Delta x + \vec{P}_{i,j-\frac{1}{2}} \cdot \vec{n}_{i,j-\frac{1}{2}} \Delta x, \end{aligned} \tag{3.11}$$

where Δx and Δy are the dimensions of the control volumes in the x and y directions. Considering the components of $\vec{P}$, equation (3.11) can be written as

$$\frac{\partial U_{i,j}}{\partial t} \Delta x \Delta y + (F_{i+\frac{1}{2},j} - F_{i-\frac{1}{2},j}) \Delta y + (G_{i,j+\frac{1}{2}} - G_{i,j-\frac{1}{2}}) \Delta x = 0. \tag{3.12}$$

Equation 3.12 can be written as

$$\frac{\partial U_{i,j}}{\partial t} + \frac{F_{i+\frac{1}{2},j} - F_{i-\frac{1}{2},j}}{\Delta x} + \frac{G_{i,j+\frac{1}{2}} - G_{i,j-\frac{1}{2}}}{\Delta y} = 0. \tag{3.13}$$

The time-derivative term can be discretized as

$$\frac{U^{n+1}_{i,j} - U^{n}_{i,j}}{\Delta t} + \frac{F^{n}_{i+\frac{1}{2},j} - F^{n}_{i-\frac{1}{2},j}}{\Delta x} + \frac{G^{n}_{i,j+\frac{1}{2}} - G^{n}_{i,j-\frac{1}{2}}}{\Delta y} = 0, \tag{3.14}$$

where n and $n+1$ represent the values at time t and $t+\Delta t$. This discretization uses the explicit Euler time advance scheme. The explicit case is simple to implement, as it only requires the computation and differentiation of the fluxes. However, the explicit schemes often prove to be inefficient. The implicit discretization of the conservation law would be in the form of

$$\frac{U_{i,j}^{n+1} - U_{i,j}^{n}}{\Delta t} + \frac{F_{i+\frac{1}{2},j}^{n+1} - F_{i-\frac{1}{2},j}^{n+1}}{\Delta x} + \frac{G_{i,j+\frac{1}{2}}^{n+1} - G_{i,j-\frac{1}{2}}^{n+1}}{\Delta y} = 0. \tag{3.15}$$

However, calculating the terms in the implicit form is not straightforward. For instance, according to the equation (3.6), $F_{i+\frac{1}{2},j}^{n+1}$ is a function of $U_{i,j}^{n+1}$ and $U_{i+1,j}^{n+1}$. However, we can approximate

$$F_{i+\frac{1}{2},j}^{n+1} \equiv F(U_{i,j}, U_{i+1,j})^{n+1} \approx F(U_{i,j}, U_{i+1,j})^{n} + \Delta t \; \frac{\partial F(U_{i,j}, U_{i+1,j})}{\partial t}|^{n} \tag{3.16}$$

and

$$\frac{\partial F(U_{i,j}, U_{i+1,j})}{\partial t}|^{n} = \frac{\partial F}{\partial U_{i,j}} \frac{\partial U_{i,j}}{\partial t}|^{n} + \frac{\partial F}{\partial U_{i+1,j}} \frac{\partial U_{i+1,j}}{\partial t}|^{n}. \tag{3.17}$$

In practice, it is easier to write this equation in a so-called δ-form by replacing $U_{i,j}^{n+1}$ with $U_{i,j}^{n} + \delta U_{i,j}^{n+1}$. The δ-form is much more convenient near the steady-state condition, where round off errors in the calculation of U can easily exceed δU, i.e., the change in U from one time level to the next. Therefore,

the equation (3.16) can be written as

$$\begin{aligned} F^{n+1}_{i+\frac{1}{2},j} &= F(U^{n+1}_{i,j}, U^{n+1}_{i+1,j}) = F(U^{n}_{i,j} + \delta U^{n+1}_{i,j}, U^{n}_{i+1,j} + \delta U^{n+1}_{i+1,j}) \\ &\approx F(U^{n}_{i,j}, U^{n}_{i+1,j}) + \frac{\partial F^{n}_{i+\frac{1}{2},j}}{\partial U_{i,j}} \delta U^{n+1}_{i,j} + \frac{\partial F^{n}_{i+\frac{1}{2},j}}{\partial U_{i+1,j}} \delta U^{n+1}_{i+1,j}. \end{aligned} \tag{3.18}$$

This result requires that we calculate the flux Jacobians which are the derivatives of the fluxes with respect to the unknowns in nearby control volumes. As an example, one of the Jacobians can be obtained as

$$\frac{\partial F^{n}_{i+\frac{1}{2},j}}{\partial U_{i,j}} = \begin{bmatrix} 0 & \frac{1}{2\beta} & 0 \\ \frac{1}{2} & \frac{u^{*}_{i,j}+u^{*}_{i+1,j}}{2} + \frac{1}{\Delta x.Re} & 0 \\ 0 & \frac{v^{*}_{i,j}+v^{*}_{i+1,j}}{4} & \frac{u^{*}_{i,j}+u^{*}_{i+1,j}}{4} + \frac{1}{\Delta x.Re} \end{bmatrix}. \tag{3.19}$$

By substituting the expanded fluxes into the fully-discrete equation, we obtain

$$\begin{aligned} \left(\frac{I^{*}}{\Delta t} + \frac{1}{\Delta x} \frac{\partial F^{n}_{i+\frac{1}{2},j}}{\partial U_{i,j}} - \frac{1}{\Delta x} \frac{\partial F^{n}_{i-\frac{1}{2},j}}{\partial U_{i,j}} + \frac{1}{\Delta y} \frac{\partial G^{n}_{i,j+\frac{1}{2}}}{\partial U_{i,j}} - \frac{1}{\Delta y} \frac{\partial G^{n}_{i,j-\frac{1}{2}}}{\partial U_{i,j}} \right) \delta U^{n+1}_{i,j} \\ + \frac{1}{\Delta x} \frac{\partial F^{n}_{i+\frac{1}{2},j}}{\partial U_{i+1,j}} \delta U^{n+1}_{i+1,j} - \frac{1}{\Delta x} \frac{\partial F^{n}_{i-\frac{1}{2},j}}{\partial U_{i-1,j}} \delta U^{n+1}_{i-1,j} \\ + \frac{1}{\Delta y} \frac{\partial G^{n}_{i,j+\frac{1}{2}}}{\partial U_{i,j+1}} \delta U^{n+1}_{i,j+1} - \frac{1}{\Delta y} \frac{\partial G^{n}_{i,j-\frac{1}{2}}}{\partial U_{i,j-1}} \delta U^{n+1}_{i,j-1} \\ = - \frac{F^{n}_{i+\frac{1}{2},j} - F^{n}_{i-\frac{1}{2},j}}{\Delta x} - \frac{G^{n}_{i,j+\frac{1}{2}} - F^{n}_{i,j-\frac{1}{2}}}{\Delta y}, \end{aligned} \tag{3.20}$$

where I^* is the unit matrix. Multiplying by Δt and labeling the terms, the above equation can be written as

$$\begin{aligned} &\left(I^* + \Delta t B_x^* + \Delta t B_y^*\right) \delta U_{i,j}^{n+1} \\ &\Delta t C_x^* \delta U_{i+1,j}^{n+1} + \Delta t A_x^* \delta U_{i-1,j}^{n+1} \\ &\Delta t C_y^* \delta U_{i,j+1}^{n+1} + \Delta t A_y^* \delta U_{i,j-1}^{n+1} \\ = -\Delta t &\frac{F_{i+\frac{1}{2},j}^n - F_{i-\frac{1}{2},j}^n}{\Delta x} - \Delta t \frac{G_{i,j+\frac{1}{2}}^n - F_{i,j-\frac{1}{2}}^n}{\Delta y}. \end{aligned} \tag{3.21}$$

Equation (3.21) can be re-written as

$$\left(I^* + \Delta t D_x^* + \Delta t D_y^*\right) \begin{bmatrix} \delta U_{1,1}^{n+1} \\ \delta U_{2,1}^{n+1} \\ \vdots \\ \delta U_{i-1,j}^{n+1} \\ \delta U_{i,j}^{n+1} \\ \delta U_{i+1,j}^{n+1} \\ \vdots \\ \delta U_{I-1,J}^{n+1} \\ \delta U_{I,J}^{n+1} \end{bmatrix} = -\Delta t \left(\frac{F_{i+\frac{1}{2},j}^n - F_{i-\frac{1}{2},j}^n}{\Delta x} - \frac{G_{i,j+\frac{1}{2}}^n - F_{i,j-\frac{1}{2}}^n}{\Delta y} \right), \tag{3.22}$$

where I and J are the maximum number of the cells in x- and y-directions, and D_x^* and D_y^* are

$$D_x^* = \begin{bmatrix} B^*_{x;1,1} & C^*_{x;1,1} & & & & & \\ A^*_{x;2,1} & B^*_{x;2,1} & C^*_{x;2,1} & & & & \\ \ddots & \ddots & \ddots & & & & \\ & A^*_{x;i-1,j} & B^*_{x;i-1,j} & C^*_{x;i-1,j} & & & \\ & & A^*_{x;i,j} & B^*_{x;i,j} & C^*_{x;i,j} & & \\ & & & A^*_{x;i,j+1} & B^*_{x;i,j+1} & C^*_{x;i,j+1} & \\ & & & \ddots & \ddots & \ddots & \\ & & & & A^*_{x;I-1,J} & B^*_{x;I-1,J} & C^*_{x;I-1,J} \\ & & & & & A^*_{x;I,J} & B^*_{x;I,J} \end{bmatrix}$$

and

$$D_y^* = \begin{bmatrix} B^*_{y;1,1} & & C^*_{y;1,1} & & & & \\ & B^*_{y;2,1} & & C^*_{y;2,1} & & & \\ & \ddots & & \ddots & & & \\ A^*_{y;i-1,j} & & B^*_{y;i-1,j} & & C^*_{y;i-1,j} & & \\ & A^*_{y;i,j} & & B^*_{y;i,j} & & C^*_{y;i,j} & \\ & & A^*_{y;i,j+1} & & B^*_{y;i,j+1} & & C^*_{y;i,j+1} \\ & & \ddots & & \ddots & & \ddots \\ & & & A^*_{y;I-1,J} & & B^*_{y;I-1,J} & C^*_{y;I-1,J} \\ & & & & A^*_{y;I,J} & & B^*_{y;I,J} \end{bmatrix}. \tag{3.23}$$

This system of equations can be solved using the Thomas algorithm [121]. It should be noted that in this case, each line problem is a 3∗3 block tridiagonal problem. The details of the solution of the block tridiagonal problems are explained elsewhere [121].

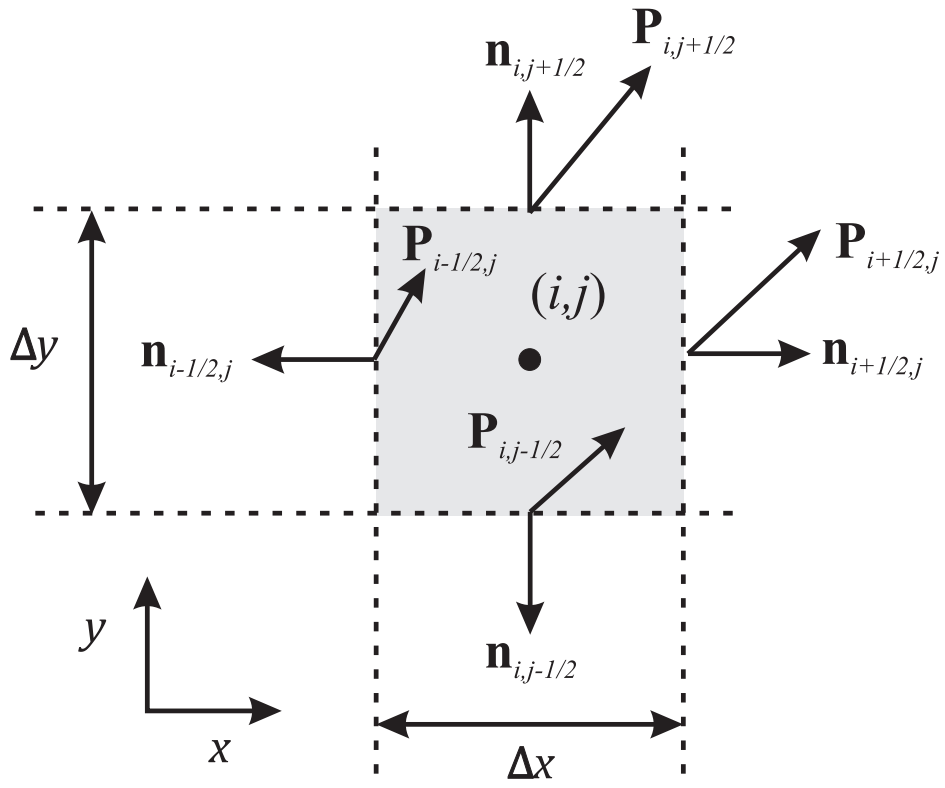

Figure 3.4: The implementation of equation (3.11) is shown.

3.1.2 Boundary condition

The boundary conditions used for the microdroplet and filler along the solid surfaces are the no-slip, no-penetration and zero pressure gradient conditions. Thus, implicit Neumann boundary conditions can be used. The microdroplet-filler interface is moving with the microdroplet transport velocity, $v_{\text{transport}}$, and is implemented by defining *fictitious* velocities within solid cells adjacent to fluid cells [123]. As it can be seen in Figure 3.5, a method based on the VOF method [108, 113] is used for modeling the moving boundary of the microdroplet. The VOF method is based on the averaging of phases at the interface, in which the volume fraction, f, is advected with the fluid flow. The volume fraction, f, for each cell is defined as

$$f = \frac{V_{\text{liq}}}{V_{\text{cell}}}, \tag{3.24}$$

where V_{liq} and V_{cell} are the (microdroplet) liquid volume and total cell volume, respectively.

As it is shown in Figure 3.6, the main idea for the implementation is that the microdroplet-filler interface is moving with the transport velocity of the microdroplet, and in each time step the volume fraction of each cell, f, is updated according to the motion of the boundaries. This volume fraction of the cells must satisfy the advection equation

$$[\partial_t f + v_{\text{transport}} \partial_x f] = 0. \tag{3.25}$$

Using the volume fraction of each cell, density and viscosity of each cell are defined as

$$\rho_{i,j} = f_{i,j}\rho_{\text{microdroplet}} + (1 - f_{i,j})\rho_{\text{filler}} \tag{3.26}$$

and

$$\mu_{i,j} = f_{i,j}\mu_{\text{microdroplet}} + (1 - f_{i,j})\mu_{\text{filler}}, \tag{3.27}$$

where $\rho_{\text{microdroplet}}$ and ρ_{filler} are the microdroplet and filler densities, and $\mu_{\text{microdroplet}}$ and μ_{filler} are the microdroplet and filler viscosities, respectively.

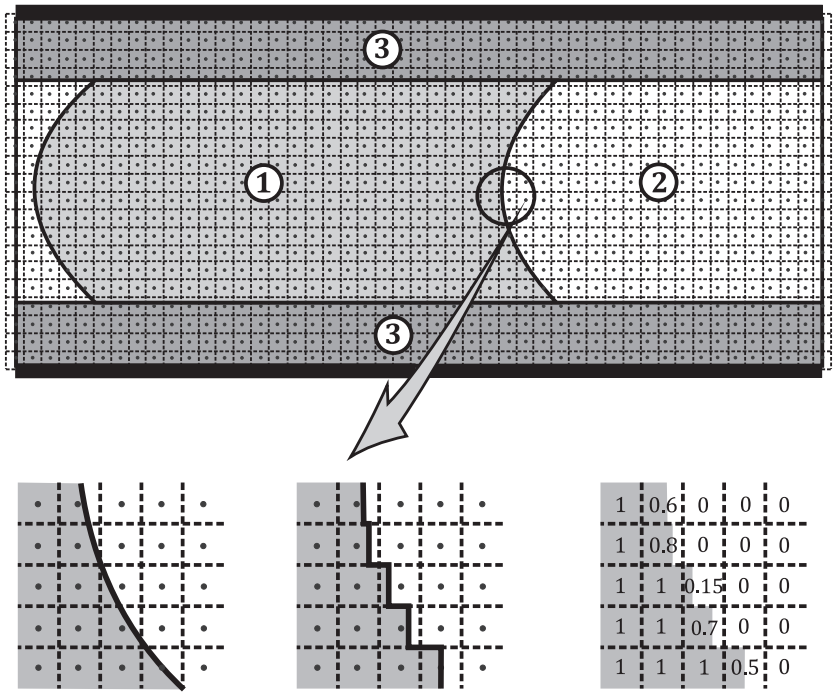

Figure 3.5: The concept of the fractional VOF method is shown. This method is based on averaging of phases at the interface, in which the volume fraction, f, is advected with the fluid flow.

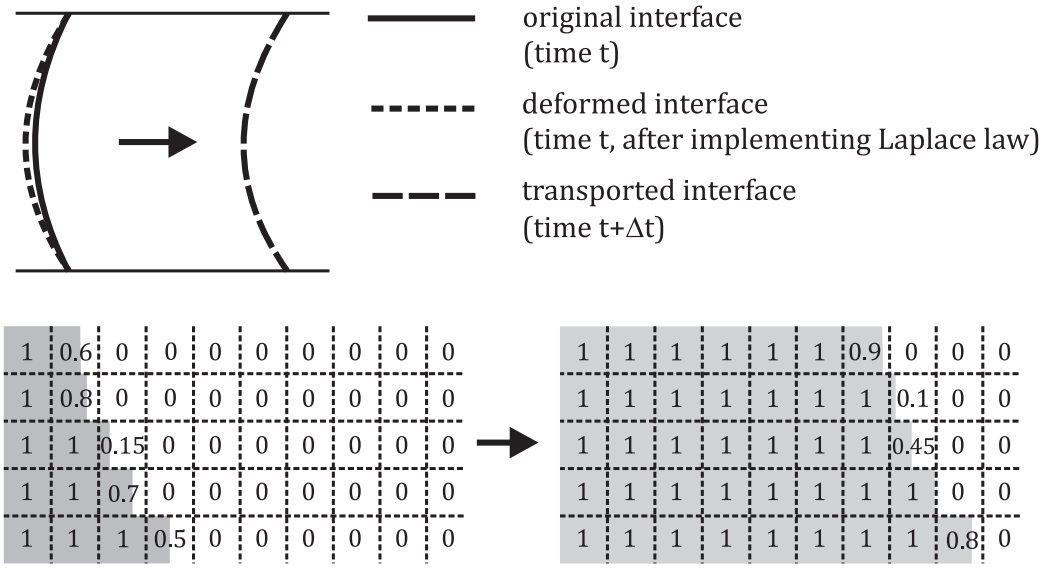

Figure 3.6: The updating process for the shape of the advancing interface is shown. The volume fraction of each cell, f, is updated according to the motion of the boundaries.

3.1.3 Stability

Solutions obtained from three mesh sizes $M1$, $M2$, and $M3$ are $\hat{u}|_{M1}$, $\hat{u}|_{M2}$ and $\hat{u}|_{M3}$, respectively, where $M2$ has twice as many mesh points as $M1$, and $M3$ has twice as many as $M2$. The error in each solution is proportional to its mesh spacing to some power k (which is 2 in the developed FVM scheme [121]); then the solutions can be written as

$$\hat{u}|_{M1} = u_e + \hat{C}(\Delta x)^k, \tag{3.28}$$

$$\hat{u}|_{M2} = u_e + \hat{C}(\frac{\Delta x}{2})^k \tag{3.29}$$

and

$$\hat{u}|_{M3} = u_e + \hat{C}(\frac{\Delta x}{4})^k. \tag{3.30}$$

The norm of the difference of the solutions can be obtained as

$$\|\hat{u}|_{M1} - \hat{u}|_{M2}\| = \hat{C}(1 - \frac{1}{2^k}) \tag{3.31}$$

and

$$\|\hat{u}|_{M2} - \hat{u}|_{M3}\| = \hat{C}(\frac{1}{2^k} - \frac{1}{4^k}). \tag{3.32}$$

This difference should get smaller as the mesh is refined. The ratio of these last two expressions can be written as

$$\frac{\|\hat{u}|_{M1} - \hat{u}|_{M2}\|}{\|\hat{u}|_{M2} - \hat{u}|_{M3}\|} = \frac{1}{2^k}. \tag{3.33}$$

The results of stability analysis for number of meshes on the vertical line are shown in table 3.1, and they indicate that the minimum number of 160 meshes in the vertical direction is needed for obtaining accurate results.

$M1$	$M2$	$M3$	k
10	20	40	1.15
20	40	80	1.56
40	80	160	1.96

Table 3.1: The minimum number of 160 meshes in the vertical direction is needed for obtaining accurate results.

3.1.4 Force calculation

After solving the hydrodynamic equations, the velocity vector inside the microdroplet is then used to find the shear force on the wall as

$$F_{\text{wall}} = \int_{\text{walls}} \tau \, \mathrm{d}A, \tag{3.34}$$

where τ is the shear stress which is defined as

$$\tau = \mu \left(\frac{\partial u}{\partial y} + \frac{\partial v}{\partial x} \right), \tag{3.35}$$

where u and v are the x- and y-components of the fluid particle velocities. Therefore, as it is shown in Figure 3.7, shear stress can be written as

$$\tau_{i,j} = \mu_{i,j\text{wall}} \left(\frac{u_{i,j\text{wall}}}{\Delta y} + \frac{v_{i+1,j\text{wall}} - v_{i,j\text{wall}}}{\Delta x} \right). \tag{3.36}$$

Equation 3.34 now can be written as

$$F_{\text{wall}} = \sum_{i} \tau_{i,j} \Delta x. \tag{3.37}$$

Moreover, using the filler hydrodynamic pressure (which is obtained from the solution of the equations (2.9) and (2.10)) at the microdroplet-filler interface, the filler (drag) force, F_{filler}, can be calculated as

$$F_{\text{filler}} = \int p_{\text{hyd}} \mathrm{d}A_{\text{interface,y}}, \tag{3.38}$$

where $dA_{\text{interface,y}}$ is the projection of the microdroplet-filler interface area element on the y-z plane. Therefore, the equation (3.39) can be written as

$$F_{\text{filler}} = \int p_{\text{hyd},i,j} \Delta y. \tag{3.39}$$

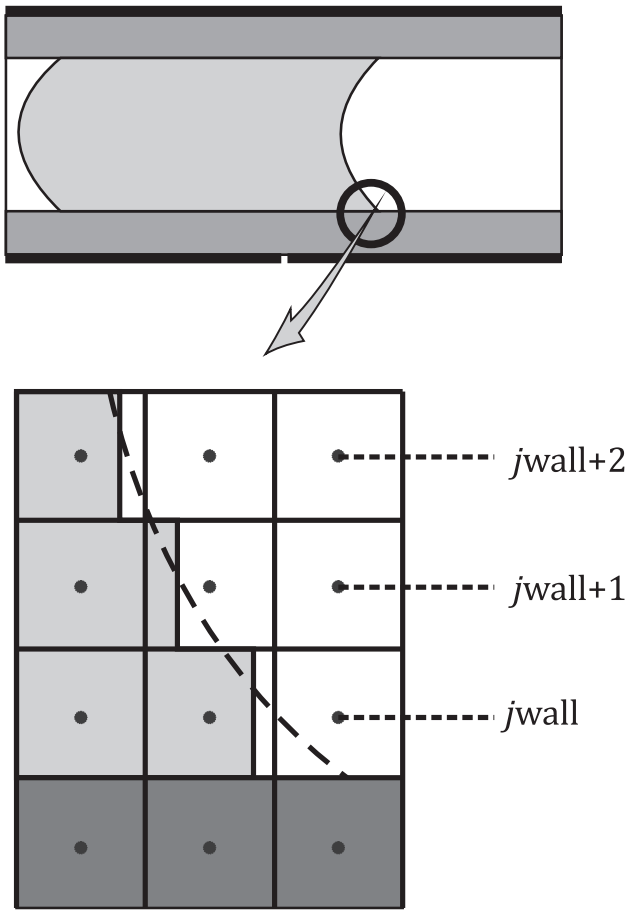

Figure 3.7: The cells adjacent to the wall are shown.

3.2 Electrostatics

3.2.1 Discretization scheme

In the present work, an electromechanical approach [108, 122] is used to calculate the horizontal force acting on the microdroplet interface. A volume integral form of the Maxwell equation (2.8) can then be written as

$$\int_{\mathrm{CV}} \vec{\nabla} \cdot \vec{D} \, \mathrm{d}V = \oint_{\partial \mathrm{CV}} \vec{D} \cdot \vec{n} \, \mathrm{d}A = 0, \tag{3.40}$$

where CV represents the control volume, and ∂CV represents the control volume cell boundary. The divergence theorem allows the volume integral within the interior to be performed as a surface integral over the control volume cell boundary.

The implementation of the equation (3.40) is shown in Figure 3.8, and this equation can be written in a discrete form for the control volume cell (i, j) as

$$\begin{aligned} \oint_{\partial \mathrm{CV}_{(i,j)}} \vec{D} \cdot \vec{n} \, \mathrm{d}A = \vec{D}_{i+\frac{1}{2},j} \cdot \vec{n}_{i+\frac{1}{2},j} \Delta y \\ + \vec{D}_{i-\frac{1}{2},j} \cdot \vec{n}_{i-\frac{1}{2},j} \Delta y \\ + \vec{D}_{i,j+\frac{1}{2}} \cdot \vec{n}_{i,j+\frac{1}{2}} \Delta x \\ + \vec{D}_{i,j-\frac{1}{2}} \cdot \vec{n}_{i,j-\frac{1}{2}} \Delta x, \end{aligned} \tag{3.41}$$

where Δx and Δy are the dimensions of the control volumes in the x- and y-directions. Since the electric displacement vector, $\vec{D}$, has two components, (D_x, D_y), and the normal vectors are oriented either horizontal or vertical, the equation (3.41) can be written as

$$D_{x,i+1/2,j}\Delta y - D_{x,i-1/2,j}\Delta y - D_{y,i,j-1/2}\Delta y + D_{y,i,j+1/2}\Delta y = 0. \tag{3.42}$$

Equation (3.42) expresses the Maxwell equation for the cell (i, j) in terms of the electric displacements at the boundaries of the cell. The electric displacement can then be written as the electric field gradient as

$$\vec{D} = (D_x, D_y) = \epsilon(E_x, E_y) = -\epsilon(\frac{\partial \Phi}{\partial x}, \frac{\partial \Phi}{\partial y}), \tag{3.43}$$

where E_x and E_y are the x- and y-components of the electric field, respectively. Using the equation (3.43), the equation (3.42) can be written as

$$\begin{aligned} \left[\epsilon_{i+1/2,j}a + \epsilon_{i-1/2,j}a + \epsilon_{i,j+1/2} + \epsilon_{i,j-1/2}\right]\Phi_{i,j} \\ -\epsilon_{i+1/2,j}a\Phi_{i+1,j} \\ -\epsilon_{i,j+1/2}\Phi_{i,j+1} \\ -\epsilon_{i-1/2,j}a\Phi_{i-1,j} \\ -\epsilon_{i,j-1/2}\Phi_{i,j-1} = 0, \end{aligned} \tag{3.44}$$

where $a = \frac{\Delta y}{\Delta x}$, and $\epsilon_{i+1/2,j}$, $\epsilon_{i-1/2,j}$, $\epsilon_{i,j+1/2}$ and $\epsilon_{i,j-1/2}$ are the permittivities at the boundaries of the cell (i, j). There are three distinct permittivity

regions in the overall system, and for sufficiently small cells, two distinct permittivity regions within cells along the microdroplet-filler interface. It should be noted that the mesh size is adjusted in a way that the cells at the microdroplet-solid and filler-solid interfaces contain one phase. Acquiring the permittivity values for interface cells is not a trivial task. Using the volume fraction method, the permitivity of each interphase cell can be calculated as

$$\epsilon_{i,j} = f_{i,j}\epsilon_{\text{microdroplet}} + (1 - f_{i,j})\epsilon_{\text{filler}}, \tag{3.45}$$

where $f_{i,j}$ is the volume fraction of the cell (i, j), and $\epsilon_{\text{microdroplet}}$ and ϵ_{filler} are the microdroplet and filler permitivities, respectively.

Finally, the equation (3.44) is solved using the Gauss-Seidel approach, and the electric potential, Φ, is found in all the regions. To accelerate the iterative procedure, the Successive Overelaxation by Lines (SLOR) method [121] is implemented. Thus, the equation (3.44) can be written as

$$\begin{aligned}
&\left[\epsilon_{i+1/2,j}a + \epsilon_{i-1/2,j}\beta + \epsilon_{i,j+1/2} + \epsilon_{i,j-1/2}\right]\delta^{k+1}_{i,j} \\
&\quad -\epsilon_{i+1/2,j}a\delta^{k+1}_{i+1,j} - \epsilon_{i-1/2,j}a\delta^{k+1}_{i-1,j} = \\
&\quad +\epsilon_{i+1/2,j}a\Phi^{k}_{i+1,j} + \epsilon_{i-1/2,j}a\Phi^{k}_{i-1,j} \\
&\quad +\epsilon_{i,j+1/2}\Phi^{k}_{i,j+1} + \epsilon_{i,j-1/2}\Phi^{k}_{i,j-1} \\
&-\left[\epsilon_{i+1/2,j}a + \epsilon_{i-1/2,j}a + \epsilon_{i,j+1/2} + \epsilon_{i,j-1/2}\right]\Phi^{k}_{i,j},
\end{aligned} \tag{3.46}$$

where k is an index for the iteration number, and δ is the increase (or decrease) in the electric potential, Φ, at each iteration. As the update to the solution is always smaller than necessary, it is possible to increase the update by an SOR factor defined as

$$\Phi_{i,j}^{k+1} = \Phi_{i,j}^{k} + \omega \delta_{i,j}^{k+1}, \tag{3.47}$$

where ω is the over-relaxation parameter which must be less than two for stability [121]. Since the equation (3.46) is stated for each independent cell, a system of equations must be solved in each iteration.

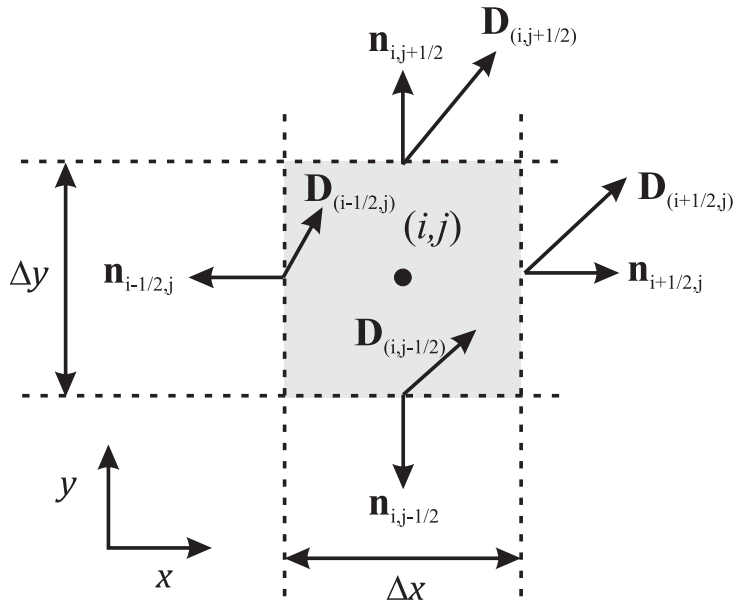

Figure 3.8: The implementation of equation (3.40) is shown. The electric displacement vector, $\vec{D}$, has two components, (D_x, D_y), and the normal vectors are oriented either horizontal or vertical.

3.2.2 Boundary condition

An implicit Neumann boundary conditions is used. The electric potential at the actuated electrode is $\Phi = V_{\text{applied}}$, and the other electrodes are grounded.

3.2.3 Driving force calculation

After finding the electrostatic potential, Φ, the electric field and electrostatic pressure, p_{el}, can be found at the cells adjacent to the microdroplet-filler interface. This electrostatic pressure distribution is used to determine both the curvature of the interface and the driving force, F_{driving}, acting on the microdroplet.

To obtain the curvature and driving force, the electric field is first calculated for the cells adjacent to the interface by way of

$$\begin{aligned}\vec{E}_{i,j} = (E_{x,i,j}, E_{y,i,j}) = -(\frac{\partial \Phi_{i,j}}{\partial x}, \frac{\partial \Phi_{i,j}}{\partial y}) = \\ (\frac{\Phi_{i,j} - \Phi_{i+1,j}}{\Delta x}, \frac{\Phi_{i,j} - \Phi_{i,j+1}}{\Delta y}).\end{aligned} \tag{3.48}$$

Using this relationship, the electrostatic pressure can be calculated for the cells using the following relationship:

$$p_{\text{el},i,j} = \frac{\epsilon |\vec{E}_{i,j}|^2}{2}. \tag{3.49}$$

The driving force can be calculated by integrating the electrostatic pressure along the interface [94, 111]. The force element acting on one cell is therefore

$$\Delta F_{i,j} = p_{\mathrm{el},i,j} \Delta A_{i,j}, \tag{3.50}$$

where $F_{i,j}$ is the force acting on the interface. As it is shown in Figure 3.9, this force is perpendicular to the surface element area $\Delta A_{i,j}$. Thus, considering the direction of the interface, the horizontal component of the force can be written as

$$\Delta F_{x,i,j} = p_{\mathrm{el},i,j} \Delta A_{i,j} \sin(\theta_{i,j}), \tag{3.51}$$

where $\theta_{i,j}$ is the angle of the interface at the point of interest. It should be noted that the effect of the vertical component of the electrostatic force on the microdroplet dynamics are neglected here. Although it has been shown before that the electric field (force) is singular at the three-phase contact line [119], the electrostatic pressure is integrable along the interface as

$$F_{x,\mathrm{interface}} = \sum_{j} p_{\mathrm{el},i,j} \Delta A_{i,j} \sin(\theta_{i,j}). \tag{3.52}$$

Finally, the total horizontal driving force will be sum of the forces acting on the advancing and receding faces given as

$$F_{\mathrm{driving,meridian}} = F_{x,\mathrm{advancing}} - F_{x,\mathrm{receding}}. \tag{3.53}$$

This force is summed over planes parallel to the meridian plane to give the total driving force.

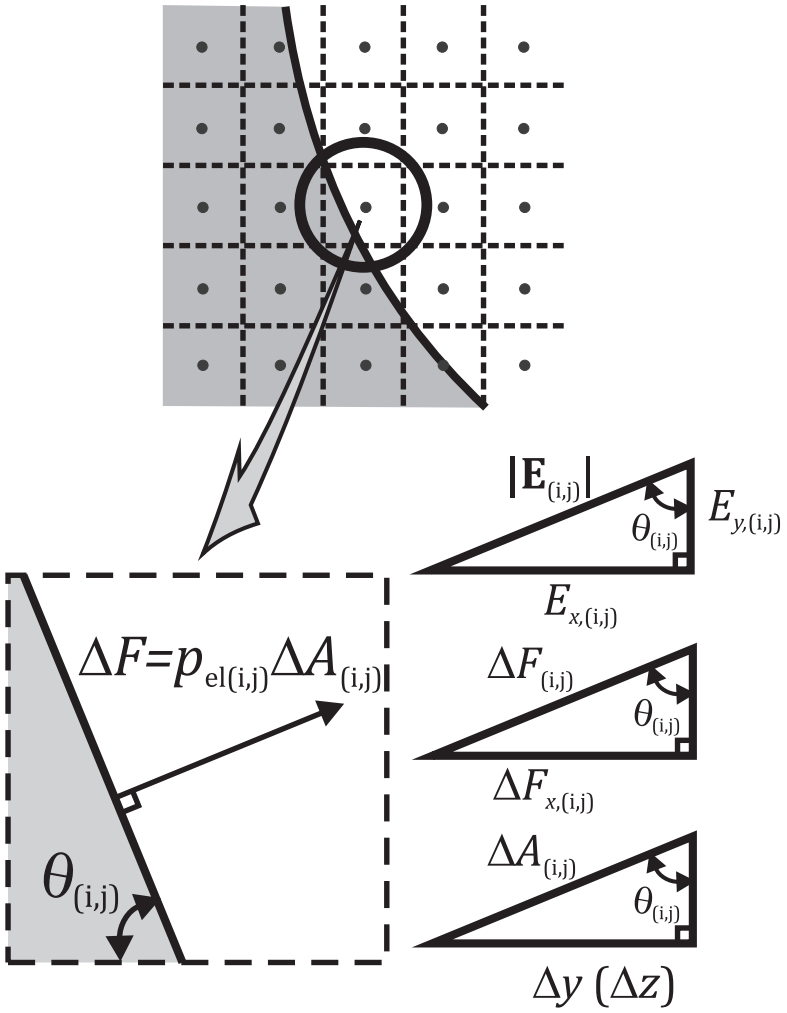

Figure 3.9: The direction of the electrostatic force acting on the microdroplet interface is shown.

3.3 Electrohydrodynamics

After finding the electrostatic and hydrodynamic pressures, the equation (2.14) can be used to find the curvature of the advancing and receding surfaces. For conductive liquids, the electrostatic pressure inside the microdroplet is zero. Thus, as it is shown in Figure 3.10, the equation (2.14) (for the advancing face) becomes

$$\begin{aligned} p_{\mathrm{el},i+1,j} + p_{\mathrm{hyd},i+1,j} - p_{\mathrm{hyd},i-1,j} &= \gamma_{\mathrm{df}}(\frac{1}{r} + \frac{1}{R}) = \gamma_{\mathrm{df}}(\frac{\mathrm{d}^2 x_{\mathrm{interface},i,j}}{\mathrm{d}y^2} + \frac{1}{R}) \\ &= \gamma_{\mathrm{df}}(\frac{x_{\mathrm{interface},i,j+1} - 2x_{\mathrm{interface},i,j} + x_{\mathrm{interface},i,j-1}}{\Delta y^2} + \frac{1}{R}), \end{aligned} \tag{3.54}$$

where R is the microdroplet radius, and r is the interface radius of curvature in the $x-y$ plane. Equation (3.54) is solved for $x_{\mathrm{interface},i,j+1}$ for all the droplet-filler interface cells to obtain $\theta_{i,j}$ for calculating the force in the equation (3.52).

Since the microdroplet voltage is known from the electrostatic solution, the Lippmann-Young equation can then be used to extract the static contact angle as

$$\cos\theta_{\mathrm{S,bottom,adv}} = \cos\theta_0 + \frac{c}{2\gamma_{\mathrm{df}}}(V_{\mathrm{app}} - V_{\mathrm{drop}})^2, \tag{3.55}$$

where $\theta_{\mathrm{S,bottom,adv}}$ is the advancing lower (static) contact angle of the microdroplet, θ_0 is the initial contact angle, c is the capacitance of the dielectric layers, V_{app} is the applied voltage, and V_{drop} is the microdroplet voltage

(which is uniform inside the conductive microdroplet).

Since the electrode underlying the receding interface is grounded, the equation (3.58) for the receding face can be written in an analogous form as

$$\cos\theta_{\mathrm{S,bottom,rec}} = \cos\theta_0 + \frac{c}{2\gamma_{\mathrm{df}}}(V_{\mathrm{drop}})^2, \tag{3.56}$$

where $\theta_{\mathrm{S,bottom,rec}}$ is the receding lower (static) contact angle of the microdroplet. It is shown that the contact angle of a moving microdroplet (dynamic contact angle) differs from its static value (static contact angle) at equilibrium [107, 114]. Using the Frenkel-Eyring activated rate theory of transport in liquids [107, 114], the static contact angle, θ_{S}, and the dynamic contact angle, θ_{D}, can be related to the microdroplet transport velocity as

$$\cos\theta_{\mathrm{S}} - \cos\theta_{\mathrm{D}} = \frac{v_{\mathrm{transport}}\xi}{\gamma_{\mathrm{df}}}, \tag{3.57}$$

where $\xi = 0.04$ is the friction factor [95]. As it is shown in Figure 3.10, the shape of the interface for the first two cells now can be expressed as

$$\frac{x_{\mathrm{interface},i,j\mathrm{wall}+1} - x_{\mathrm{interface},i,j\mathrm{wall}}}{\Delta y} = \frac{1}{\tan(\theta_{\mathrm{D,bottom}})}. \tag{3.58}$$

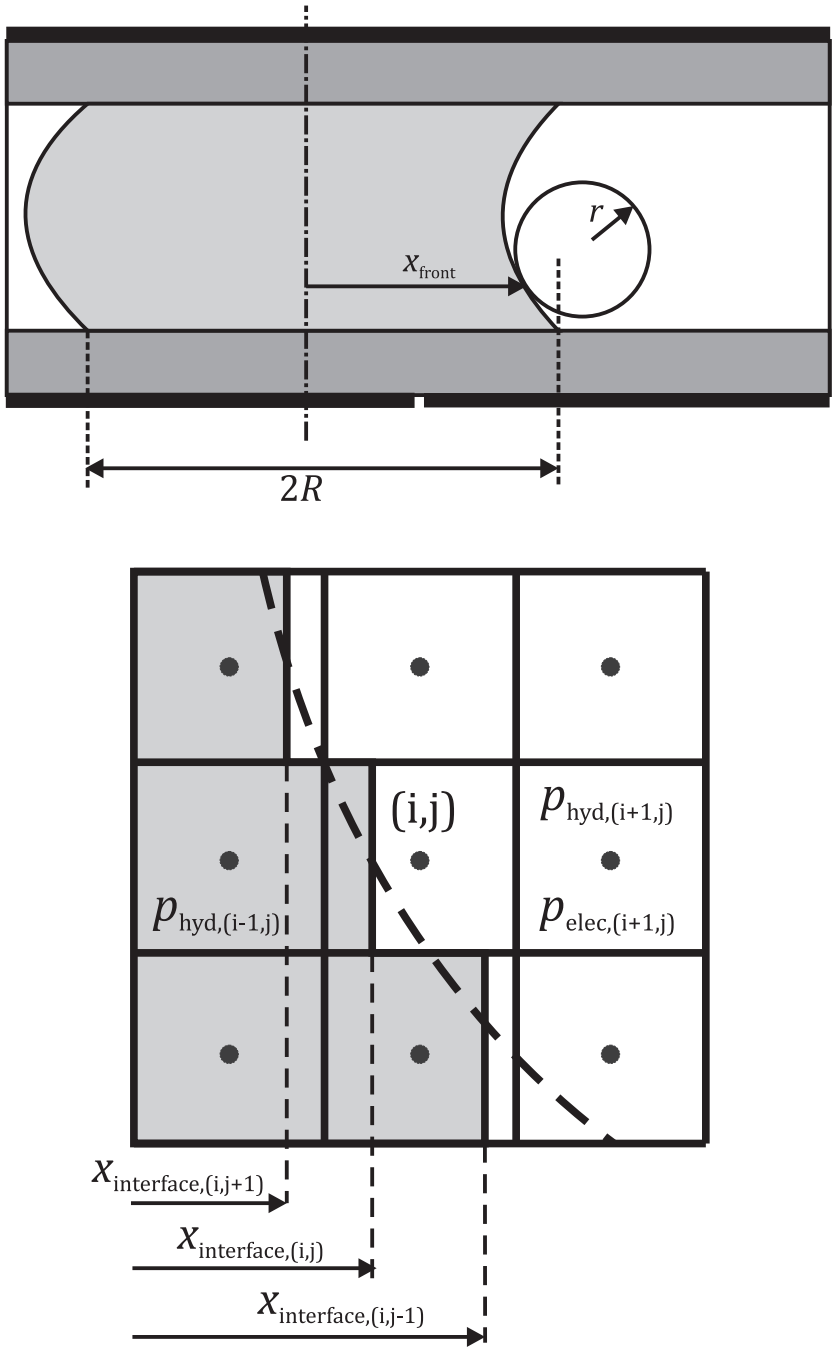

Figure 3.10: The implementation of the Laplace Law for the advancing face where R is the radius of the microdroplet is shown, and r is the radius of curvature of the interface in the $x-y$ plane.

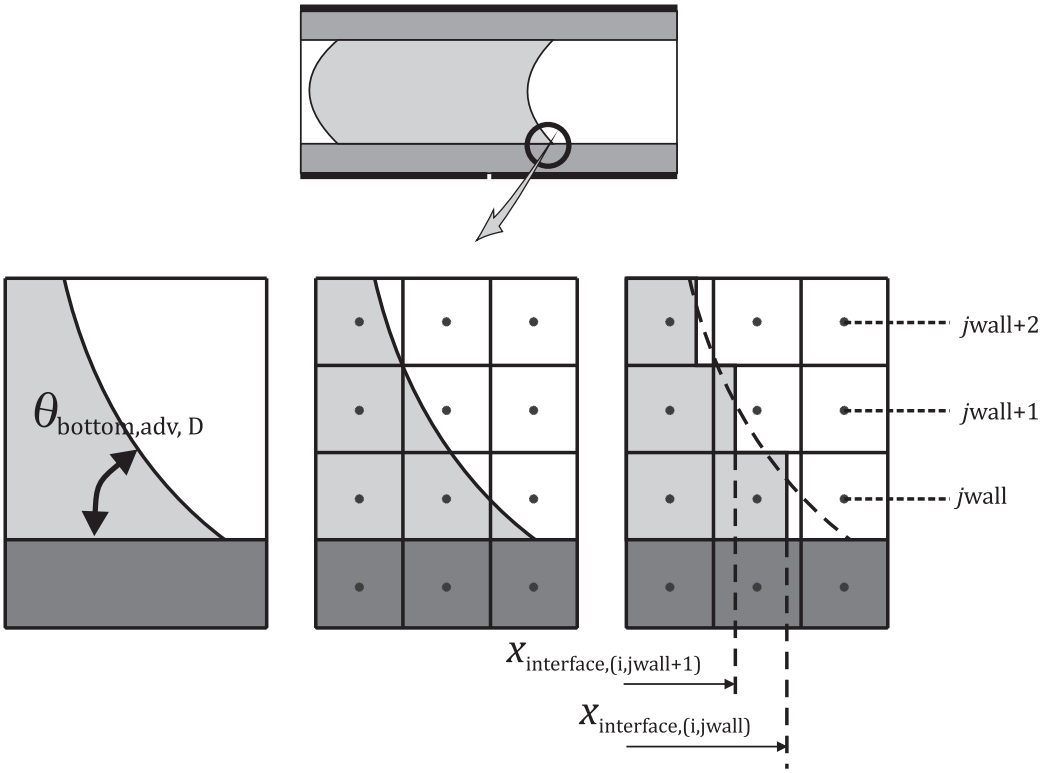

Figure 3.11: Use of the Lippmann-Young equation is shown for the advancing interface.

3.4 Adsorption

3.4.1 Force calculation

As explained in Chapter 2, the adsorption force, F_{ads}, is defined as

$$F_{\mathrm{ads}} = -\frac{\mathrm{d}}{\mathrm{d}x}\left[(\gamma_{\mathrm{sl0}} - \gamma_{\mathrm{sl}}(t))A_{\mathrm{w}} + (\gamma_{\mathrm{lv0}} - \gamma_{\mathrm{lv}}(t))A_{\mathrm{p}}\right]. \tag{3.59}$$

Therefore, the adsorption force at each time step can be calculated as

$$\begin{aligned} F_{\text{ads}} = -([(\gamma_{\text{sl0}} - \gamma_{\text{sl}})A_{\text{w}} + (\gamma_{\text{lv0}} - \gamma_{\text{lv}})A_{\text{p}}]^{n+1} \\ - [(\gamma_{\text{sl0}} - \gamma_{\text{sl}})A_{\text{w}} + (\gamma_{\text{lv0}} - \gamma_{\text{lv}})A_{\text{p}}]^{n})/ (v_{\text{transport}}\Delta t) , \end{aligned} \tag{3.60}$$

where $n+1$ and n represent the values at time t and $t + \Delta t$.

3.4.2 Capacitance change

As it was mentioned in Chapter 2, the adsorbed proteins to the solid surface form a new layer on top of the dielectric and hydrophobic layer, which decreases the total capacitance of the system as

$$c(t) = \frac{1}{1/c_0 + 1/c_{\text{ads}}(t)}, \tag{3.61}$$

where $c_{\text{ads}}(t)$ is the capacitance per unit area of the protein layer on the surface which can be related to the solid-liquid surface protein concentration, Γ_{sl}, as

$$c_{\text{ads}}(t) = \frac{\Gamma_{\text{sl}}(t)}{\Gamma_{\text{sl}\infty}} c_{\infty}, \tag{3.62}$$

where $\Gamma_{\text{sl}\infty}$ and c_{∞} are the saturated solid-liquid surface protein concentration and capacitance, respectively. However, in this equation, c_{∞} is the saturated capacitance which has to be measured for each surface and protein. In the present work, a new methodology for in-situ characterization of the system capacitance is introduced and implemented as explained below.

Experimental setup

The setup for this sampling protocol is shown in Figure 3.12. The electrodes are activated by a high voltage DC power supply (Stanford Research System, PS350) that is triggered by a relay (SANYOU, DSY2Y-S-205L) and a computer. A large resistor R_{major} is used to match the resistance of the microfluidic system, and a small resistor R_{minor} creates a voltage divider by a digital oscilloscope (Tektronix, TDS 2004B) for sampling. The digital oscilloscope has an internal finite resistance, R_{osc}, and capacitance, C_{osc}. The time-variant waveform recorded by the oscilloscope is processed by the computer to extract the microfluidic capacitance values, i.e., C_{diel} and C_{drop}, and microfluidic resistance values, i.e., R_{diel} and R_{drop}.

The contact angle values of the microdroplet are determined simultaneously to the capacitance values by means of digital imaging using a microscope (Leica Z6 APO) which is connected to a high resolution digital CCD camera. The digital CCD camera is used for accurate measurement of the microdroplet contact angle (see Appendix A).

Capacitance sampling

The sampling technique is applied here to digital microfluidic architectures with a capacitance sampling submodule. The capacitance sampling is well suited to the systems with dielectric layers covering the electrodes, and it is an alternative method to the conductance sampling method (see Appendix

B). The time variation of the internal dielectric properties can be effectively mapped onto the recorded voltage forms by measuring the time-varying capacitance. The capacitance of the structure is recorded as an effective capacitance (C_{eff}) of the multilayered system with contributions from all internal dielectric regions (C_{diel}) and fluid regions (C_{drop}). The method employed to sample capacitance must be particularly sensitive, as capacitance values are exceedingly small for micro- and milli-scale fluid structures. To provide this high level of sensitivity, voltage actuation signals used for the digital microfluidic control are incorporated directly into the capacitance sampling process. This also omits the need for an additional capacitance measuring voltage signal which would be applied by an external capacitance measuring instrument. The complete configuration for this submodule is shown in Figure 3.12. The displayed circuit quantifies the conduction and displacement effects within the droplet with the resistor R_{drop} and capacitor C_{drop}, respectively, between overlying and underlying dielectric layers with resistance and capacitance values of R_{diel} and C_{diel}, respectively. The capacitor across the complete digital microfluidic system is the parameter of interest, and it can be extracted by way of time contstant curve fitting with the voltage divider external circuitry shown in Figure 3.12. The resistor $R_{\text{major}} = 50$ MΩ is made to be sufficiently large, in comparison to the resistor $R_{\text{minor}} = 500$ kΩ, to 1) provide an observable time constant, 2) minimize the effects of the voltage sampling oscilloscope's finite input resistance $R_{\text{osc}} = 1$ MΩ, and 3) to scale down the oscilloscope input voltage.

The circuitry is energised at time $t = 0$ sec by a high voltage DC power supply with a fixed voltage V_{applied}. The high voltage is switched on using a computer-controlled high-voltage relay. The resulting voltage waveform across R_{minor} is then recorded by the computer-controlled data acquisition system. The time-varying evolution of this transient $V_{C2}(t)$ provides a measure of the charge build-up and discharge across the microdroplet. It is important to note that the time-dependent response is also a function of the oscilloscope capacitance C_{osc}. These two capacitors control the charging and discharging of the structure, and the voltage across the oscilloscope terminals can be found through the transient circuit analysis. The complete result is

$$\begin{aligned} V_{C2}(t) = \tfrac{V_{\text{applied}}}{(s_1 - s_2)} \left(\tfrac{1}{R_3 C_2} + \tfrac{R_2 s_2}{R_1 + R_2 + R_3} \right) (e^{s_1 t} - e^{s_2 t}) + \\ \tfrac{V_{\text{applied}}\, R_2}{R_1 + R_2 + R_3} (1 - e^{s_2 t}), \end{aligned} \tag{3.63}$$

where

$$s_{1,2} = -b/(2a) \pm \left[b^2 - 4ac \right]^{1/2} \Big/ (2a) \tag{3.64}$$

and

$$\begin{aligned} a &= R_1 R_2 R_3 C_1 C_2 \\ b &= R_1 R_2 C_1 + R_1 R_2 C_2 + R_1 R_3 C_1 + R_2 R_3 C_2 \\ c &= R_1 + R_2 + R_3. \end{aligned} \tag{3.65}$$

The capacitance values here are defined across the microfluidic structure, $C_1 = (1/C_{\text{drop}} + 2/C_{\text{diel}})^{-1}$, and the measurement oscilloscope, $C_2 = C_{\text{osc}}$.

The resistance values are defined with $R_1 = R_{\text{drop}} + 2R_{\text{diel}}, R_2 = (R_{\text{osc}} + R_{\text{minor}})^{-1}$ and $R_3 = R_{\text{major}}$. The rise of the voltage waveform will initially be dominated by the oscilloscope capacitor as it charges while the fall of the voltage waveform back down towards zero is dominated by the microdroplet capacitance.

The capacitance sampling module extracts the voltage waveform from the oscilloscope and uses a curve fitting algorithm to determine the capacitance across the digital microfluidic system, C_1, as a function of time. This process is repeated at the discrete time steps that are used to actuate the microdroplets, and the transient voltage waveform is recorded during this process. The details of these in-situ measurements are explained in Appendix A.

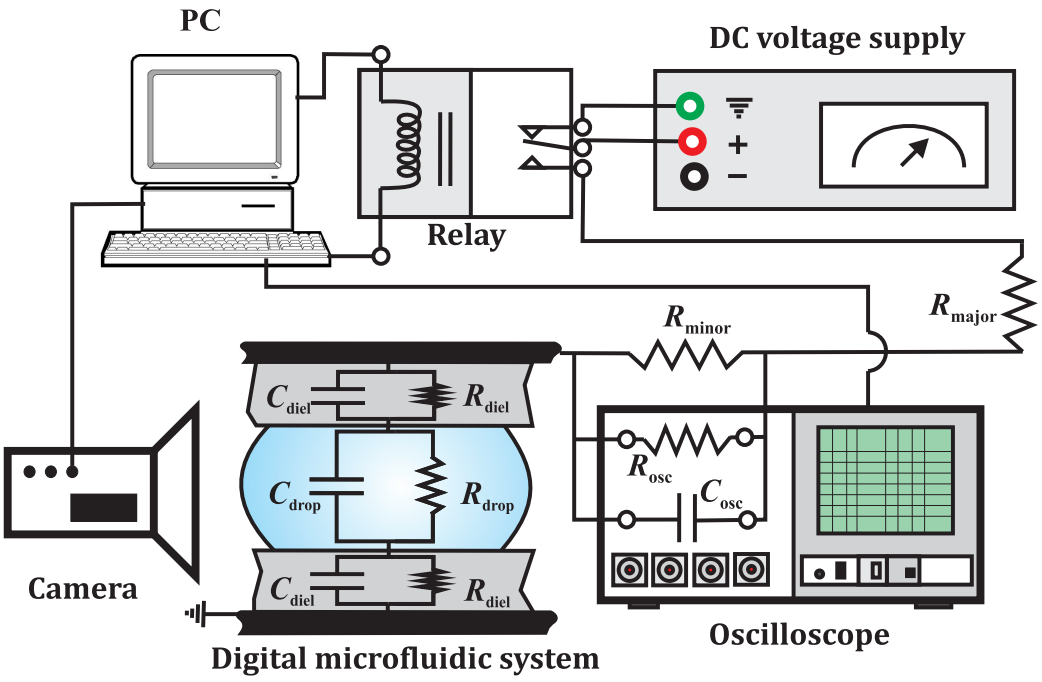

Figure 3.12: The setup for the capacitance sampling.

3.4.3 Evaporation

In the present work it is assumed that the concentration gradient is directed radially outward and equal to

$$\frac{\partial \mathcal{C}_v}{\partial n} = -(\mathcal{C}_{v0} - \mathcal{C}_{v\infty})\frac{k}{2}, \tag{3.66}$$

where k is the mean curvature of the interface, and can be expressed as

$$k = [[p_{\mathrm{el}}]] - [[p_{\mathrm{hyd}}]]/\gamma_{\mathrm{df}}. \tag{3.67}$$

The curvature of the interface can be extracted from Laplace law by determining the electrostatic pressure from the electric potential and field in the system and by determining the hydrodynamic pressure from the Navier-Stokes and continuity equations inside the microdroplet and the filler. Therefore, the concentration gradient can be written as

$$\frac{\partial \mathcal{C}_v}{\partial n}|_{i,j} = -(\mathcal{C}_{v0} - \mathcal{C}_{v\infty})\frac{p_{\mathrm{el},i+1,j} + p_{\mathrm{hyd},i+1,j} - p_{\mathrm{hyd},i-1,j}}{2\gamma_{\mathrm{df}}}. \tag{3.68}$$

Finally, the microdroplet evaporation rate can be obtained as

$$\frac{\mathrm{d}m}{\mathrm{d}t} = -\frac{2D_v}{\gamma_{\mathrm{df}}}(\mathcal{C}_{v0} - \mathcal{C}_{v\infty})\sum_j (p_{\mathrm{el},i+1,j} + p_{\mathrm{hyd},i+1,j} - p_{\mathrm{hyd},i-1,j})\Delta y. \tag{3.69}$$

The mass loss due to the evaporation can be related to the change in the microdroplet radius as

$$\frac{\mathrm{d}m}{\mathrm{d}t} = 2\rho_{\mathrm{droplet}}\pi RH\frac{\Delta R}{\Delta t}. \tag{3.70}$$

As it is shown in Figure 3.13, this change in the radius can be implemented into the numerical scheme. In each time step, first, microdroplet electrohydrodynamic deformation is calculated, and then the change in the microdroplet radius is implemented.

3.5 Dynamics

Finally, after calculating all the forces, the dynamic equation can be solved to find the microdroplet velocity. The dynamic equation can be written as

$$m\frac{\mathrm{d}v_{\mathrm{transport}}}{\mathrm{d}t} = F_{\mathrm{driving}} - F_{\mathrm{wall}} - F_{\mathrm{tpcl}} - F_{\mathrm{evp}} - F_{\mathrm{ads}}. \tag{3.71}$$

Using an explicit scheme, this equation can be solved to find the microdroplet velocity. The explicit scheme can be written as

$$m\frac{v^{n+1}_{\mathrm{transport}} v^{n}_{\mathrm{transport}}}{\Delta t} = F^{n}_{\mathrm{driving}} - F^{n}_{\mathrm{wall}} - F^{n}_{\mathrm{tpcl}} - F^{n}_{\mathrm{evp}} - F^{n}_{\mathrm{ads}}. \tag{3.72}$$

In the following chapter, the results of the developed model are presented and verified with experimental results, and it is shown that the model provides

an accurate representation of digital microfluidic transport. Moreover, an extensive parametric variation is used to derive the Maximum Actuation Switching Frequency for ranges of the microdroplet size, gap spacing between the top and bottom plates and electrode pitch size. As a result of this study, an adjustable force-based actuation switching frequency implementation is introduced, and it is shown that rapid microdroplet motion is obtained by in-situ adjusting of the switching frequency.

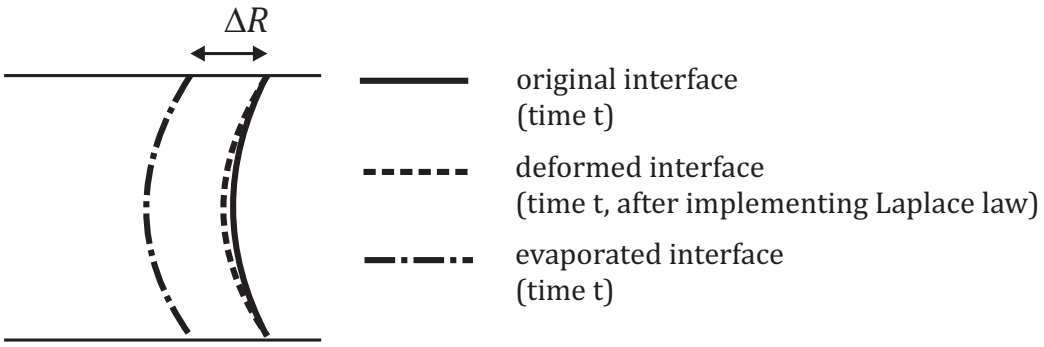

Figure 3.13: In each time step, microdroplet electrohydrodynamic deformation is calculated, and then the change in the microdroplet radius is implemented.

Chapter 4

Results and Discussion

In this chapter, the results obtained from the developed model are presented and discussed. As it was explained in the previous chapters, the developed numerical model has different submodules. To show the accuracy of the model and its submodules, the modeling results are compared to the experimental observations. After verifying and validating the results, the results obtained from different submodules of the numerical model are discussed. Finally, to show the application of the developed numerical model, the microdroplet motion in digital microfluidic systems is optimized, and using the model, a new algorithm is proposed to achieve higher microdroplet velocities.

4.1 Verification

To verify different submodules of the model, the effect of each phenomena has to be studied in isolation. First, a system including silicone oil as the filler fluid is modeled; thus, the effects of evaporation and adsorption are neglected. This will allow us to verify the electrohydrodynamic submodule of the model. After verifying the electrohydrodynamic results, a system which uses air as

filler fluid is modeled. For such a system, the effects of evaporation and adsorption become important. Therefore, these effects are included next, and the results are compared to the experimental observations.

4.1.1 Electrohydrodynamics

In this section, the results of the developed model are presented and verified with experimental results in the absence of evaporation and adsorption. The experimental setup introduced by Pollack et al. [14] is used here. The filler fluid is 1 cSt silicone oil. An 800 nm thick film of parylene C provides insulation over the control electrodes. Both the top and bottom plates have a 60 nm thick top-coating of Teflon AF 1600. The applied voltage is 26 V, and the dynamics of a 900 nl droplet of 0.1 M KCl solution with a diameter of D=1.9 mm in a system including an electrode pitch of $L = 1.5$ mm and gap spacing of $H = 0.3$ mm is modeled. The modeling results are compared to the experimental results [14].

Verification of the Model with Single Electrode Transport

The proposed model must be accurate in terms of both displacement and velocity, as the model will be applied to the actuation analyses of the motion across numerous electrodes. As it can be seen in Figures 4.1 and 4.2, the microdroplet displacement and velocity obtained from the model show strong agreement with the experimental results. The model displacement in Figure 4.1 closely follows the rising edge of the experimental displacement. The

model then shows complete transport over the 1.5 mm electrode pitch over 1.0 s. The experimental results in Figure 4.1 show nearly-complete transport over the electrode pitch, but the initial misalignment in the microdroplet position and insufficient voltage lead to a final displacement of 1.2 mm in 0.4 s.

Figure 4.2 shows that the microdroplet velocity obtained from the model is in excellent agreement with the experimental values. The sharp peak around the maximum driving force originates from the sudden change in the rate of the increase in the wetted area. The observed difference between the experimental and modeling values at the beginning of its motion is attributed to the hysteresis effects in the system [14] and the ideal nature of the model.

Application of the Model to Multiple Electrode Transport

The result in the previous section applied to transport over a single electrode system. Practical devices will, however, include multiple electrodes with the goal of achieving steady-state transport across many of these electrodes by applying appropriator switching frequencies. For this reason, it is important to understand the electrohydrodynamic effects and their relationship to the applied voltage switching frequencies. The switching frequencies deliver appropriately-timed voltages to the underlying electrodes, and it is important that the switching frequencies be optimized for the desired microdroplet average velocity. The relationship between these frequencies and the average velocity is studied in this subsection.

Figure 4.3 shows the arrival time for the microdroplet leading edge at various positions (i.e. displacements) across a three-electrode structure. Results are shown for four switching frequencies (2.5, 5, 10 and 15 Hz) and an applied voltage of 26 V. The optimal case for transport occurs with a switching frequency of approximately 13 Hz. It is immediately apparent from this figure that the increase in the frequency leads to shorter arrival times at the end of the third electrode: the 2.5 Hz case has an arrival time of 0.91 s; the 5 Hz case has an arrival time of 0.48 s; the 10 Hz case has an arrival time of 0.24 s. Note that this trend does not apply to the 15 Hz case (which is above the optimal frequency of 13 Hz), as the microdroplet does not successfully complete its transport over each individual electrode. Such a phenomenon has been observed before [14, 108] suggests that there is a Maximum Actuation Switching Frequency (MASF) that exist for each applied voltage. Figure 4.4 shows the MASFs over a range of voltages. The results from the proposed electrohydrodynamic model are compared to the experimental observations [14] and the results obtained from the explicit electrostatic and hydrodynamic modeling approach [15]. The ability of the proposed approach to follow the experimental data is readily apparent, and compared to the previous approach, the new methodology models the microdroplet dynamics with greater accuracy for both low and high transport velocities.

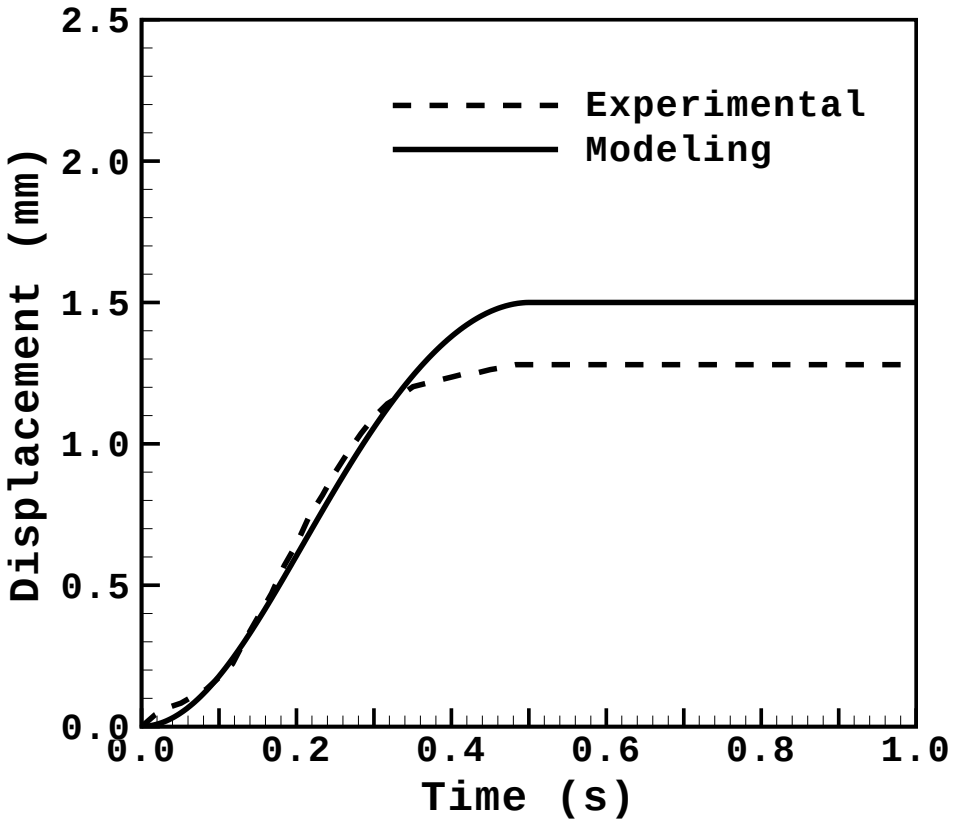

Figure 4.1: The displacement is compared to the experimental results [14]. The applied voltage is 26 V, and the results are shown for the transition of the microdroplet over one electrode.

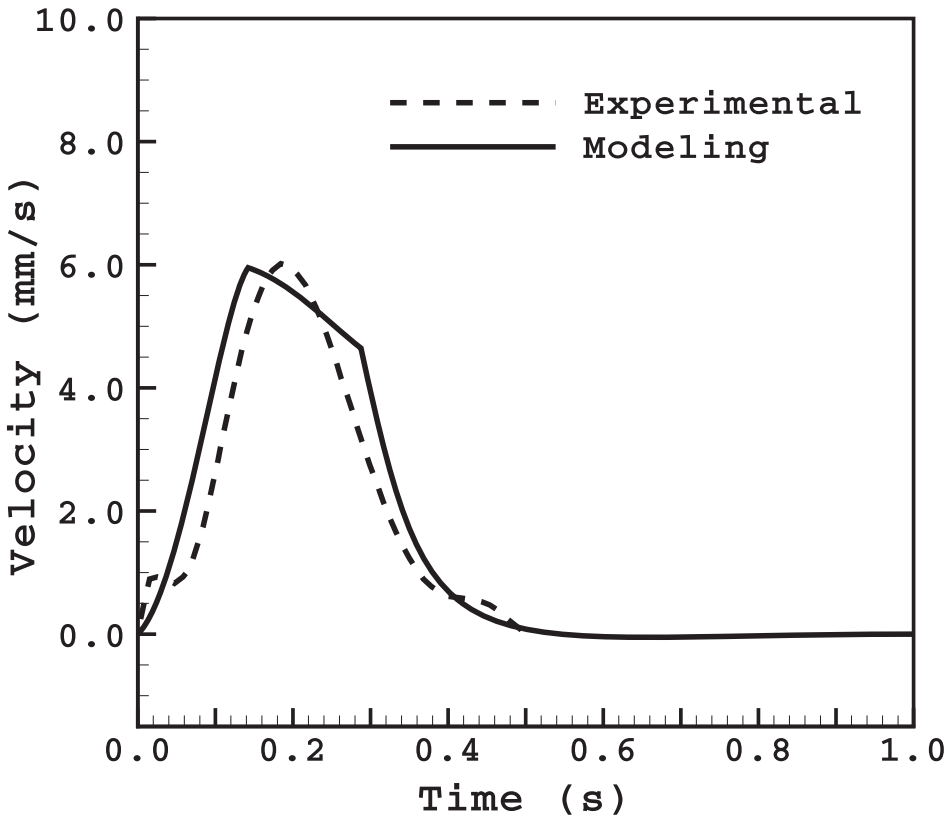

Figure 4.2: The velocity is compared to the experimental results [14]. The applied voltage is 26 V, and the results are shown for the transition of the microdroplet over one electrode.

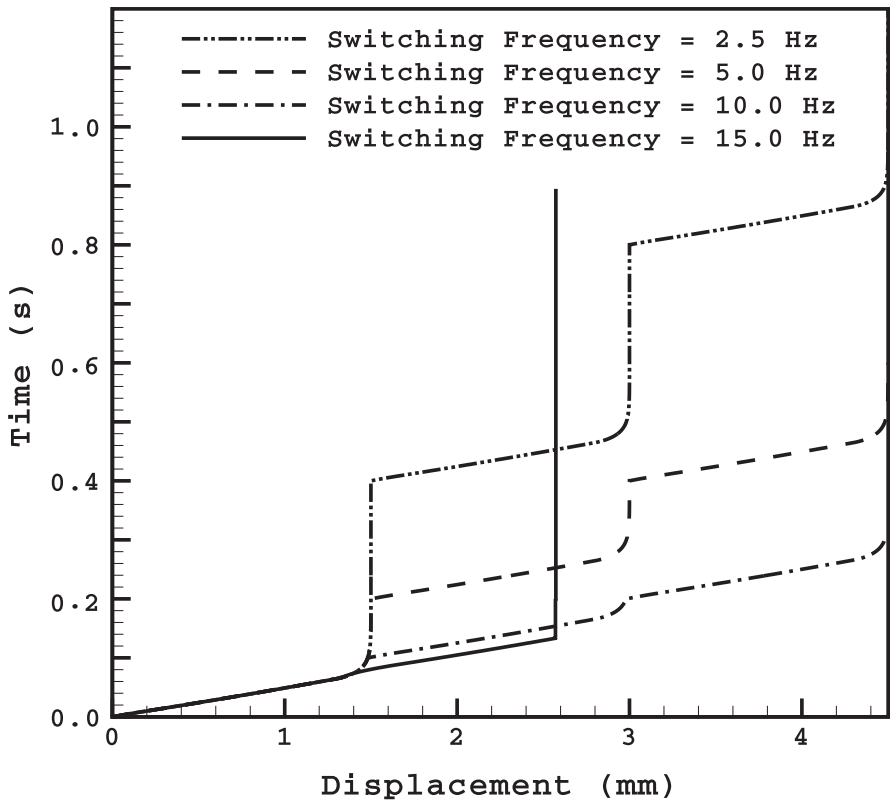

Figure 4.3: The arrival time for the microdroplet leading edge is shown for various positions (i.e. displacements) across a three-electrode structure. The applied voltage is 26 V, and the results of the model are shown for four switching frequencies (2.5, 5, 10 and 15 Hz).

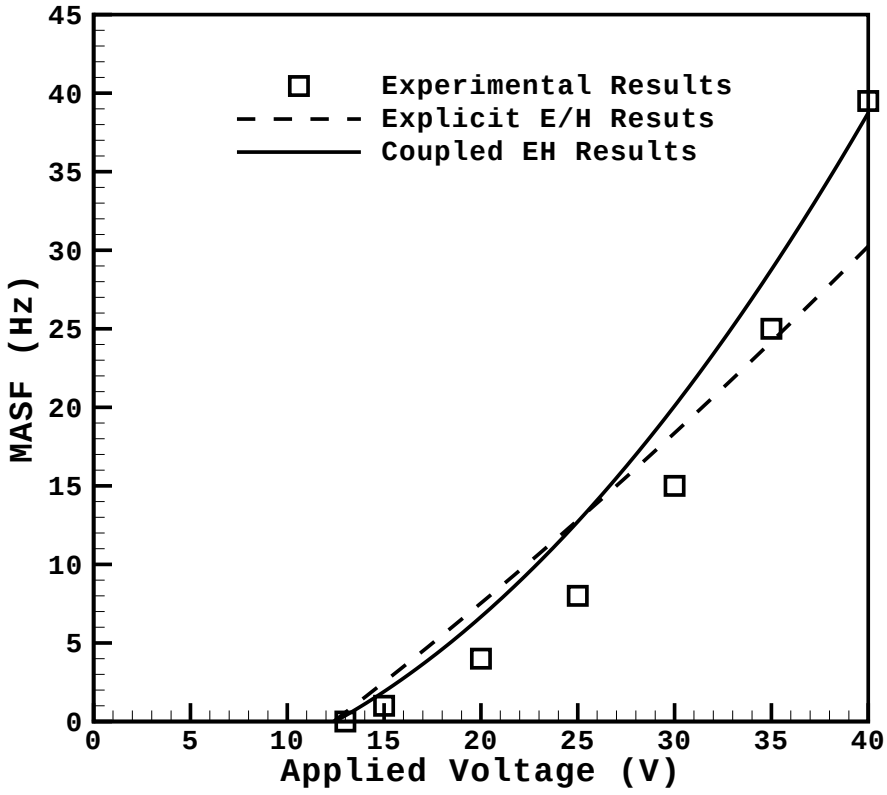

Figure 4.4: The maximum switching frequencies for the proposed coupled electrohydrodynamic (EH) model are shown for a range of voltages and compared to the explicit electrostatic and hydrodynamic modeling [15] and [14] experimental results. The filler fluid is 1 cSt silicone oil.

4.1.2 Evaporation

In this subsection the results are obtained for the system which uses air as a filler medium. The experimental setup introduced by Pollack et al. [14] is used here with air as the filler liquid, rather than oil.

Figure 4.5 shows the MASF values obtained from the experimental and modeling results over a range of voltages. It is apparent that the modeling results are in excellent agreement with the the experimental data, and the model successfully simulates the microdroplet motion in air-filler digital microfluidic systems.

4.1.3 Adsorption

To verify the accuracy of the adsorption submodule, the calculated capacitance is compared to the measured capacitance of the system. The experimental setup introduced by Yoon and Garrell [16] is used here. A 120 nm thick film of silicone oxide provides insulation over the control electrodes. Both the top and bottom plates have a 50 nm thick top-coating of Teflon AF 1600. The dynamics of a 5 μl droplet of 4 μg/ml BSA solution (pH of 6.5) is observed in this experimental system and compared to the proposed model. The comparison is shown in Figure 4.6.

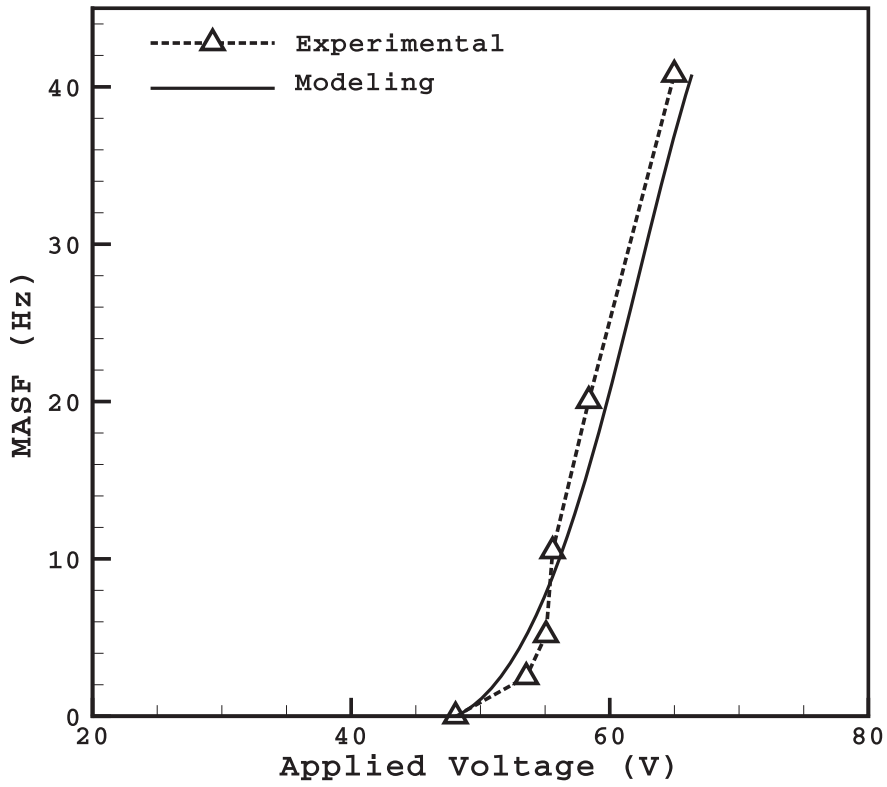

Figure 4.5: The maximum switching frequencies for the proposed model are shown for a range of voltages and compared to the experimental results [14]. The filler fluid is air.

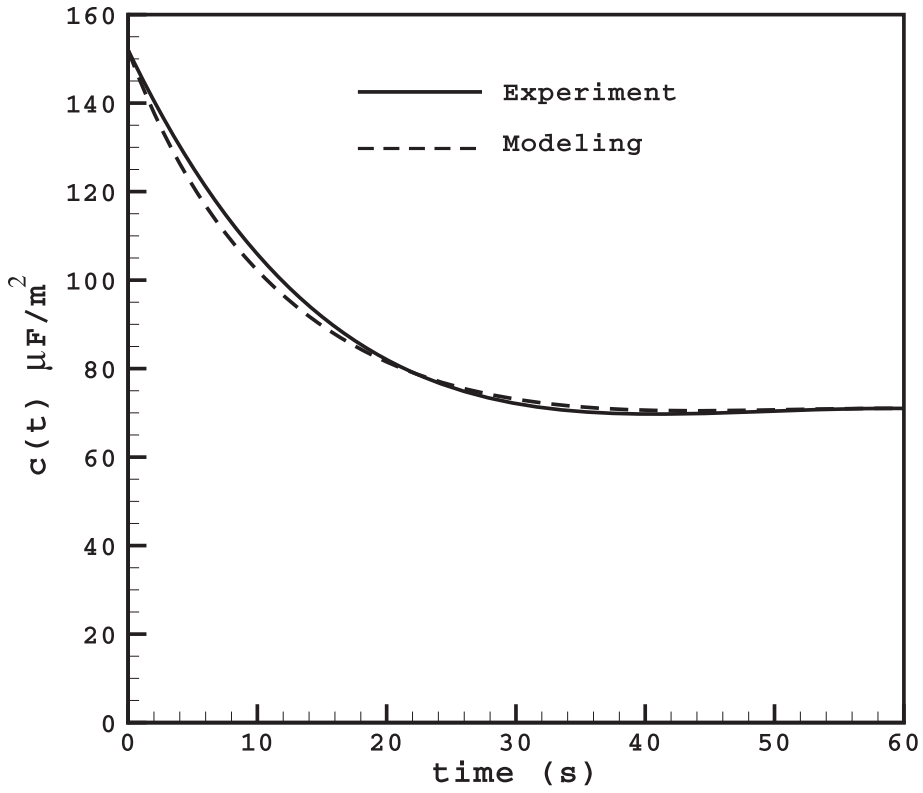

Figure 4.6: The capacitance values obtained from equation (3.61) are shown and seen to be in excellent agreement with the values calculated for the experimental results presented in [16].

4.2 Study of microdroplet dynamics

4.2.1 Liquid-filler systems

To gain insight into the switching frequency response, the model is applied to the case of transport with a 10 Hz switching frequency at 26 V, with a threshold voltage of 13 V. Solutions of the microdroplet hydrodynamics (inside) and electrostatics (outside) are shown at four different times in Figure 4.7. The relationship between the electrostatic and hydrodynamic equations is apparent as the microdroplet is transported from the uncharged left electrode to the charged right electrode. Figure 4.7a shows the system under the condition of no applied voltage for which all the contact angles are 104° (i.e. the contact angle value defined for 0.1 M KCl on Teflon [14]). Vortices form inside the microdroplet due to its motion [15]. These two-dimensional vortices in the x-y plane show that the flow inside the microdroplet is not one-dimensional, and hence the Hele-Shaw flow assumption used in current microdroplet hydrodynamics modeling is not an accurate assumption. This is an important observation in terms of pressure. The multi-dimensional nature of the microdroplet internal flow causes a hydrodynamic pressure gradient along the microdroplet faces which plays a crucial role in determining the microdroplet shape. The streamlines inside the microdroplet represent the microdroplet internal flow as seen by an observer sitting on a coordinate system moving with the microdroplet velocity. The streamlines can be used to calculate the velocity gradient and the wall (shear) force acting on the microdroplet, F_{wall}.

Coupled multiphysics equations of the model are numerically solved simultaneously and plotted in Figures 4.8-4.11 to characterize the electrohydrodynamics of the microdroplet motion. The results are shown as the microdroplet passes three electrodes. Figure 4.8 shows the values of different forces acting on the microdroplet. Since the gap spacing is relatively small ($H = 0.3$ mm) compared to the microdroplet diameter ($D = 1.9$ mm), the filler force, F_{filler}, has the smallest value among all the forces, whereas the wall force, F_{wall}, is more significant. Moreover, it is observed that the three-phase contact line force, F_{tpcl}, is the largest resistance force. This shows that molecular adsorption and desorption processes around the contact-line could not be accounted for by viscous effects of the microdroplet and filler. Finally, the electric potential distribution changes as the microdroplet passes the electrodes (as shown by the color map of Figure 4.7). This leads to the rising and falling of the driving force during transport.

The driving force increases from zero to a maximum value, then it dips to a local minimum value as the advancing face of the microdroplet reaches the next electrode. This change in the driving force represents the change in the electrostatic pressure, microdroplet voltage, and hence the microdroplet shape and contact angles. This observation is confirmed in Figure 4.9 which shows the voltage of the microdroplet as a function of its position. The voltage of the microdroplet increases as it passes each electrode, and its potential drops to zero as it reaches the next electrode. Figure 4.10 shows the advancing bottom, receding bottom and top contact angles of the microdroplet as

a function of position as it passes over three electrodes. The contact angle changes are due to the varying microdroplet voltages as it passes the electrodes: the advancing bottom static (and dynamic) contact angle increases from 70.6° (and 70.6°) to 75.9° (and 76.14°) as the microdroplet passes each electrode due to the increase in the microdroplet voltage from 0 V to 2.2 V (or the decrease in the voltage drop across the dielectric layer). Changes in the top contact angles follow a different trend, as the contact angle decreases due to the increase of the voltage difference across the 60nm Teflon AF top layer. Since the bottom layer is thicker than the top layer, the receding bottom contact angle does not change as much as the top contact angle. It is apparent that the model is capable of capturing the very small change in the contact angle due to the low applied voltage.

The presented multiphysics model simultaneously solves the dynamic equation of microdroplet motion and ultimately tracks the microdroplet. The transient velocity of the microdroplet is shown as a function of position in Figure 4.11. Jerky motion of the microdroplet motion is apparent here. The microdroplet starts its motion with zero velocity and quickly reaches its maximum velocity. Interestingly, the velocity of the microdroplet does not reach to zero as it approaches the next electrode due to its momentum. Since the force balance is changing (Figure 4.8), the minimum values are not the same for different electrodes, and the microdroplet is accelerating as it passes the electrodes. This is a very interesting observation which highlights the crucial role of the optimum switching frequency for achieving higher transport

velocities.

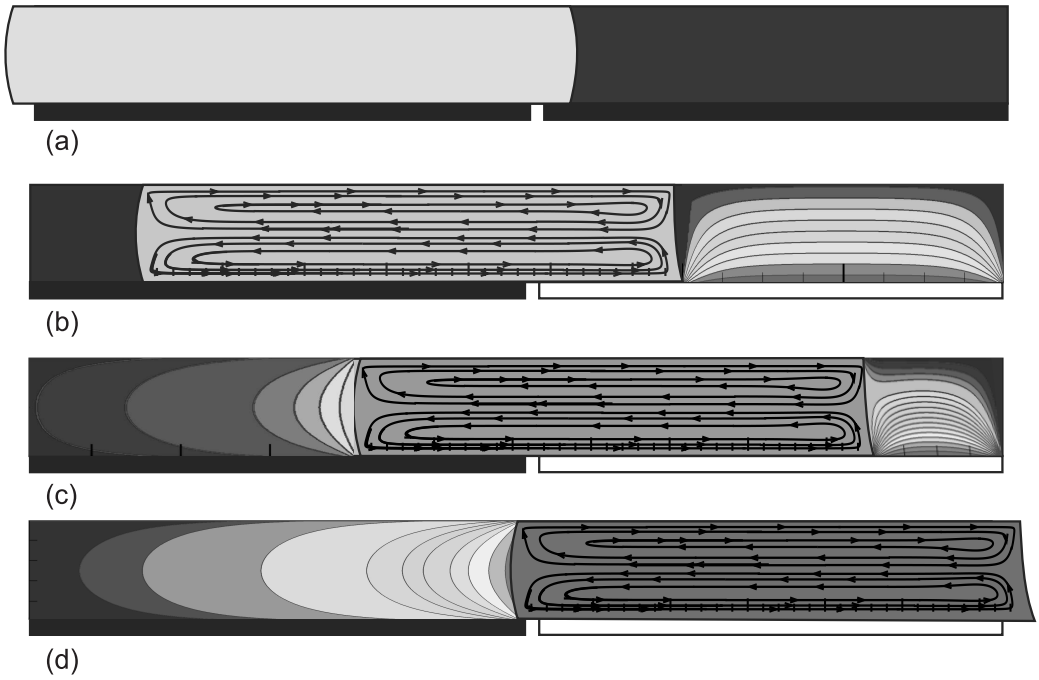

Figure 4.7: The modeling results for microdroplet hydrodynamics and electrostatics are shown at four instants: (a) time = 0 s (with no applied voltage), (b) time = 0.14 s, (c) time = 0.22 s and (d) time = 0.5 s.

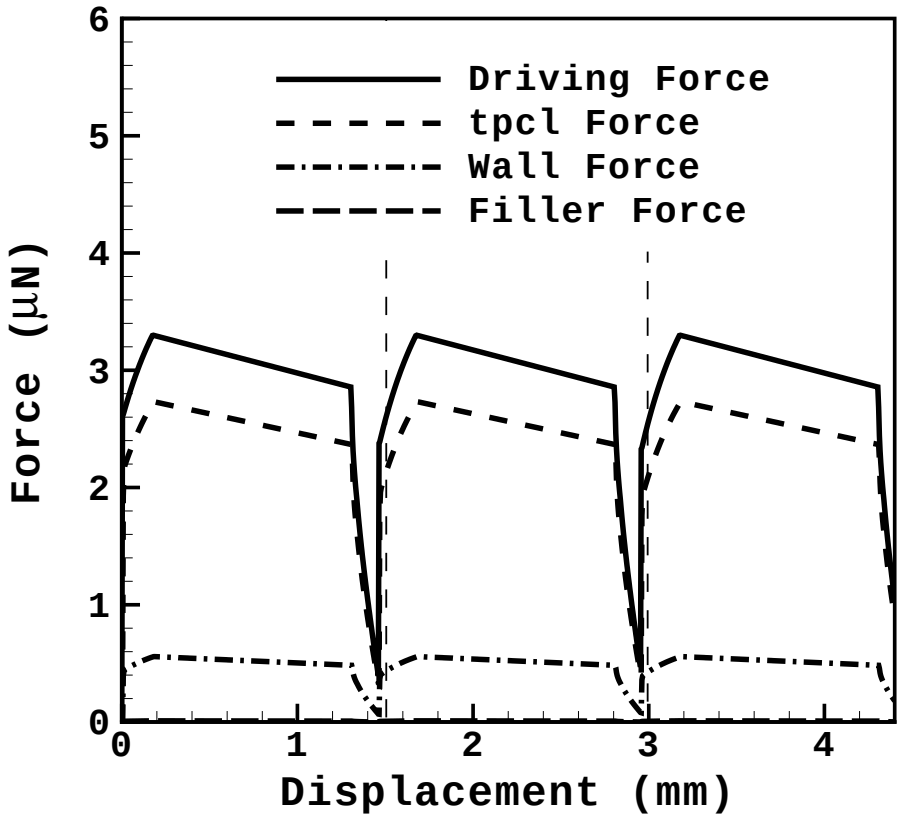

Figure 4.8: Driving, contact line, filler and wall forces are shown as functions of microdroplet position.

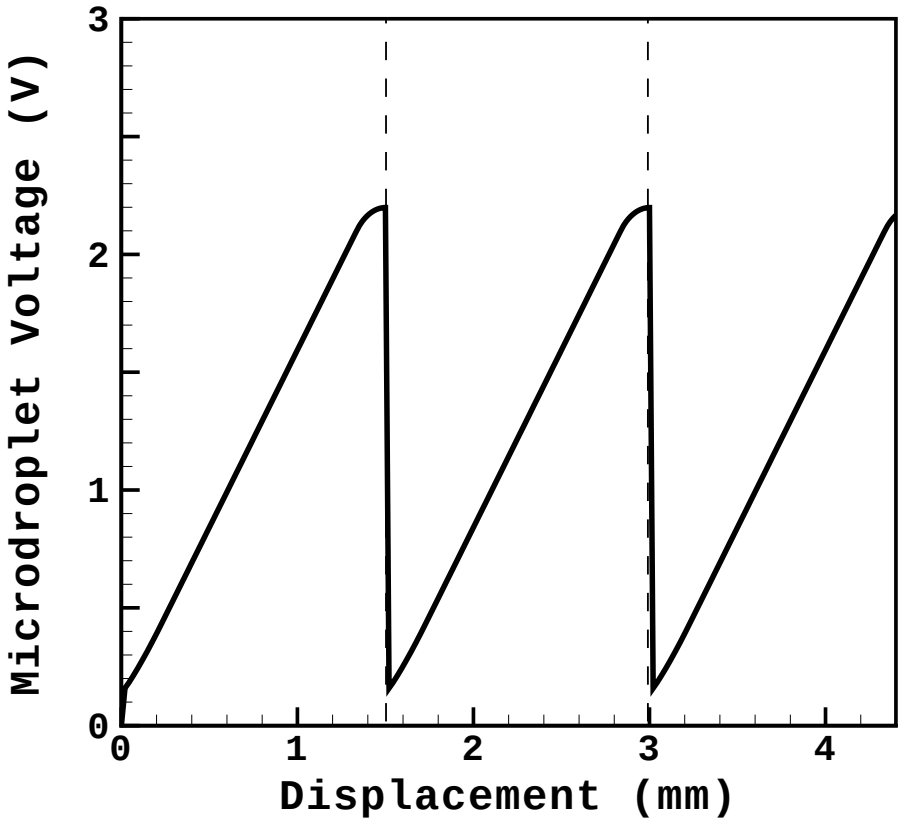

Figure 4.9: The microdroplet voltage is shown as a function of its position.

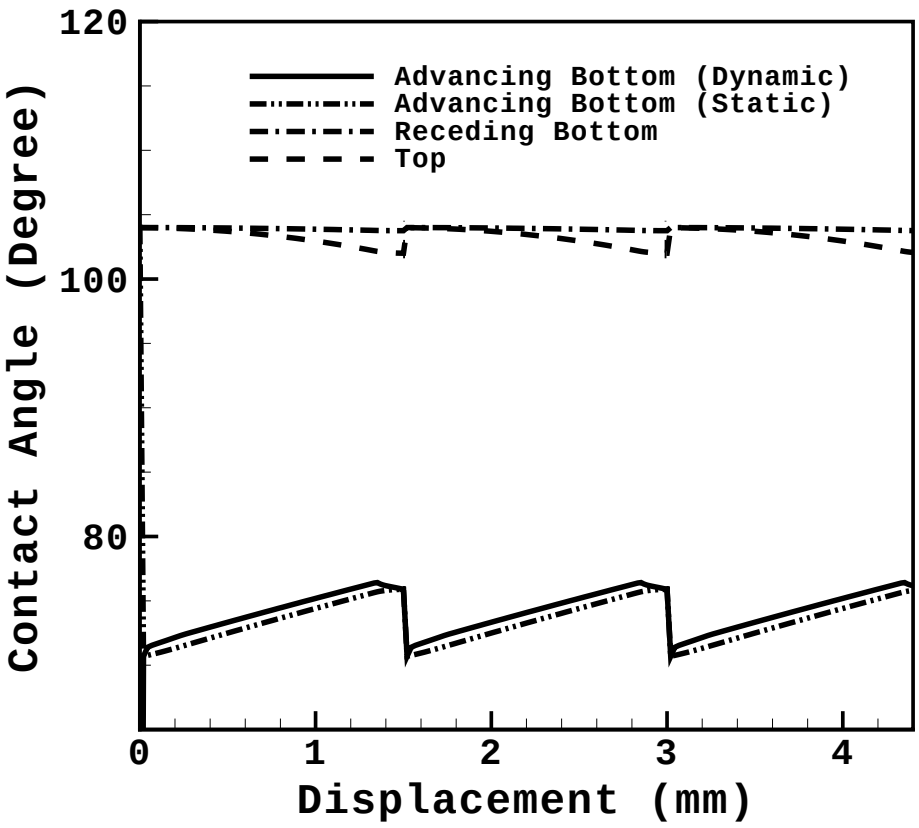

Figure 4.10: Microdroplet advancing bottom, receding bottom and top contact angles are shown as a function of position.

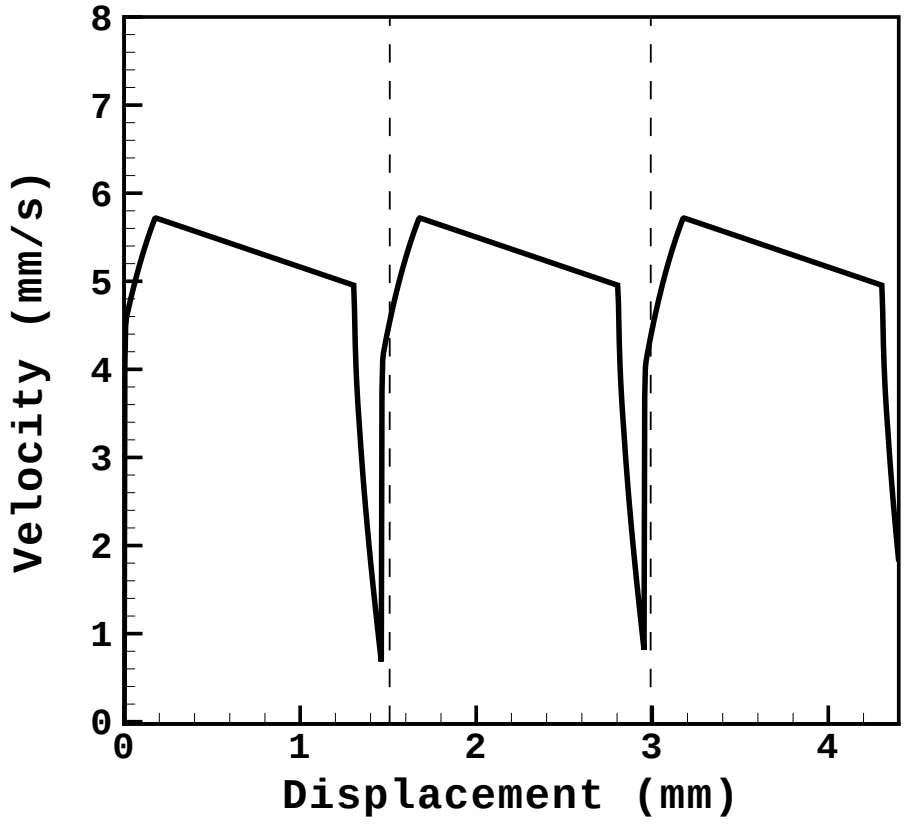

Figure 4.11: Transient velocity of the microdroplet is shown as a function of its position.

4.2.2 Air-filler systems

In this section, the effects of evaporation on the microdroplet dynamics are studied using the proposed model. The experimental setup introduced by Pollack et al. [14] is used here. The filler fluid is air with the relative humidity of 44% and temperature of 21°C. The actuation voltage is 55 V, and the threshold voltage is 47 V. The dynamics of a 900 nl droplet of 0.1 M KCl solution with a diameter of $D = 1.9$ mm studied on a device with an electrode pitch of $L = 1.5$ mm and gap spacing of $h = 0.3$ mm. The microdroplet diameter was calculated as a function of its displacement as it passes a single electrode (see Figure 4.12). The decrease in the microdroplet diameter from its original value, $D = 1.9$ mm, to $D = 1.65$ mm (13% decrease in the diameter as it moves over one electrode) shows the significance of evaporation in microdroplet dynamics. Evaporation can significantly affect the microdroplet transport which can only be achieved when the microdroplet diameter is larger than the electrode size. Thus, for the configuration used in this thesis, the drop diameter D =1.5 mm (i.e., the same as the electrode size) will be the critical value. For diameters smaller than the critical value, microdroplet will not complete its transport. Also, the change in the microdroplet diameter due to evaporation can significantly affect the force balance as the driving and resisting forces depend on the microdroplet size. Figure 4.13 shows the driving force, F_{driving}, as a function of its displacement. In essence, the driving force for the non-evaporating microdroplet is larger than that for the evaporating microdroplet. Since the microdroplet diameter

gets close to its critical value, $D = 1.5$ mm, the driving force for the evaporating microdroplet decreases drastically at the end of its transport.

The combined effects of the decrease in the microdroplet size and driving force can be seen in Figure 4.14 which presents the microdroplet velocity as a function of its displacement. The driving force is smaller for the evaporating microdroplet which which leads to a decrease in the velocity. However, the effect of mass loss and decrease in the diameter due to evaporation is initially more than that of the driving force. Thus, the microdroplet tends to accelerate, and hence, the evaporating microdroplet moves faster at the beginning of its motion. As the driving force for the evaporating microdroplet significantly decreases at the end of the electrode, the microdroplet decelerates and its velocity becomes smaller than that of the non-evaporating microdroplet. However, due to the competitive effects of mass loss and the reduced driving force, the time periods required for both evaporating and non-evaporating microdroplets to pass one electrode are very close, which is in agreement with the observed velocity trend (see Figures 4.14 and 4.15).

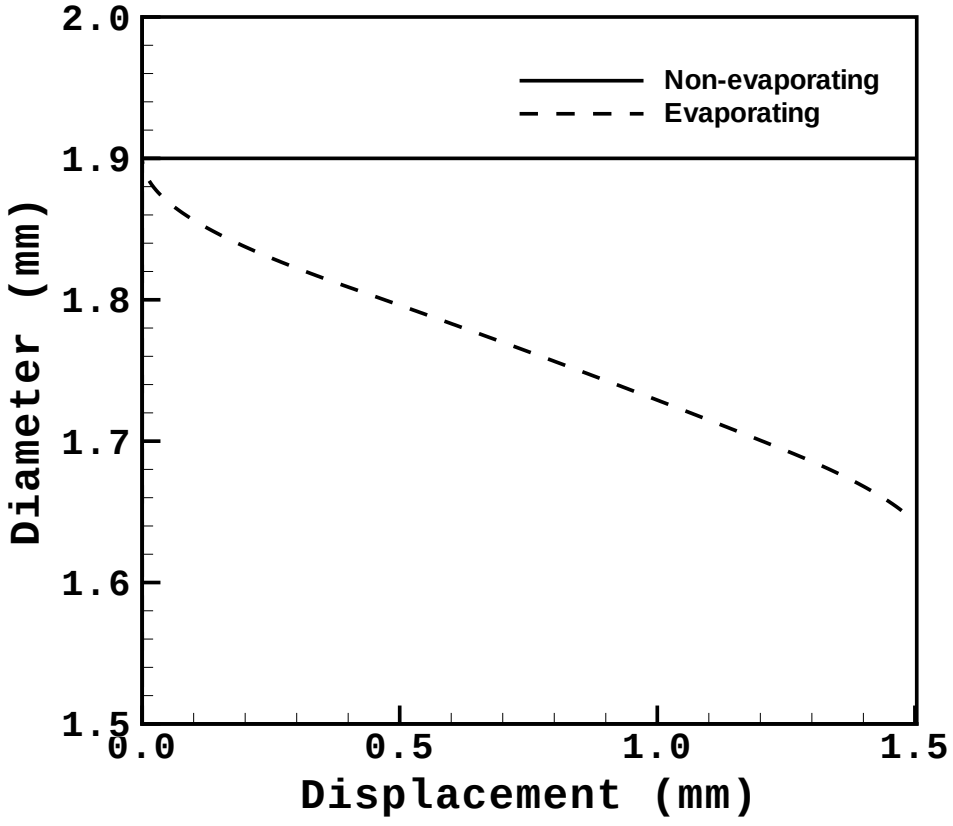

Figure 4.12: The microdroplet diameter is shown as a function of its displacement as it passes a single electrode.

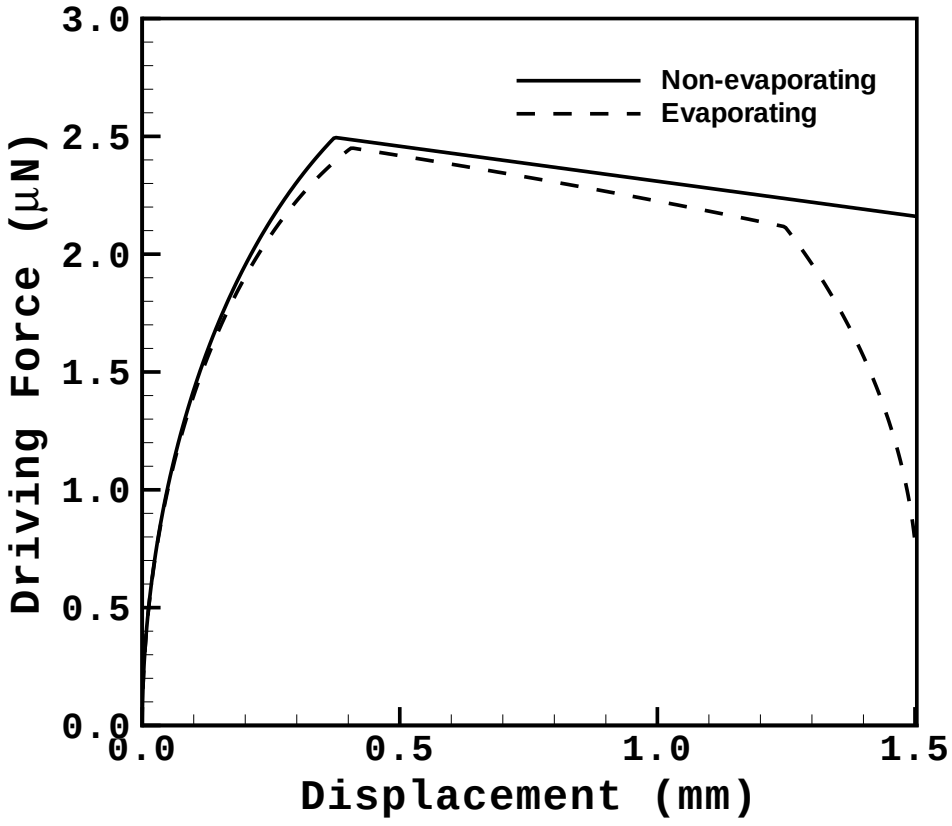

Figure 4.13: The driving force, F_{driving}, is shown as a function of its displacement.

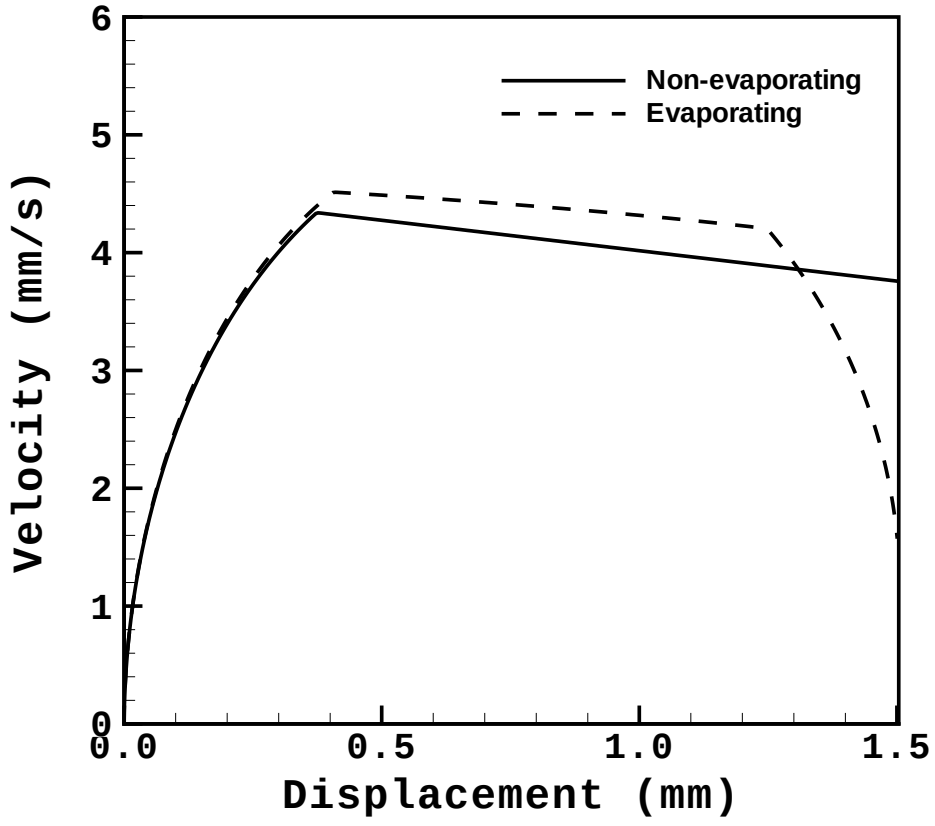

Figure 4.14: The microdroplet velocity is shown as a function of its displacement.

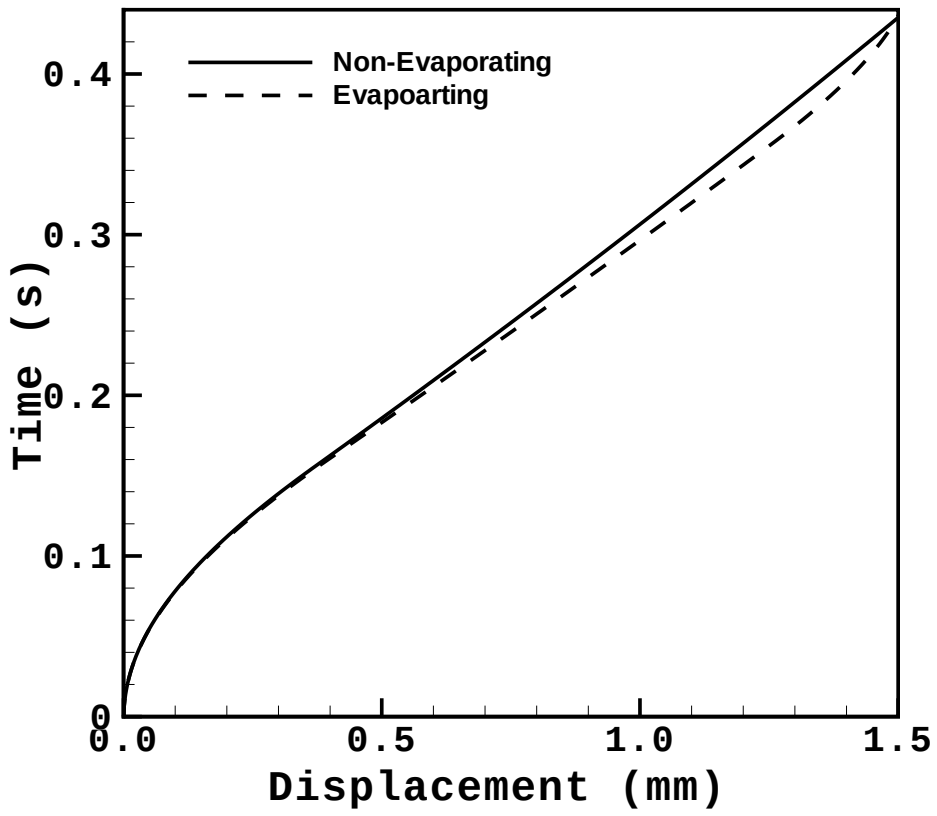

Figure 4.15: The time required for microdroplet transport is shown as a function of its displacement.

4.2.3 Adsorption

In this section the effects of the protein adsorption and evaporation are studied for the structure in the previous section. The total BSA concentration and pH of the solution are 5 μg/ml and 6.5, respectively. The BSA mass in the so-

lution is shown as a function of the microdroplet displacement in Figure 4.16. As it can be seen here, the BSA mass decreases due to the permanent protein adsorption to the solid surface. Since the microdroplet is moving, the solid-liquid interface constantly changes, and as a result, adsorbed to the surface will be left behind. The mass of the BSA decreases to the point at which all the molecules are adsorped onto the surface. This observation is confirmed in Figure 4.17 which shows the surface protein concentration at the solid-liquid interface as a function of the microdroplet displacement. As it can be seen here, the surface protein concentration increases from zero to a maximum value, 2.95 mg/m^2, and suddenly drops to zero when no more molecules in the bulk solution exist. The calculated surface protein concentration values are in good agreement with the experimental observations [34].

Finally, the combined effects of the evaporation and protein adsorption on the concentration of the BSA is shown in Figure 4.18. The BSA concentration initially increases due to the lower adsorption rate (Figure 4.17) and higher evaporation rate (Figure 4.16). As the adsorption rate increases, the BSA concentration decreases, despite the decrease in the volume, and finally reaches to zero. Therefore, adsorption and evaporation have competitive effects on determining the BSA concentration.

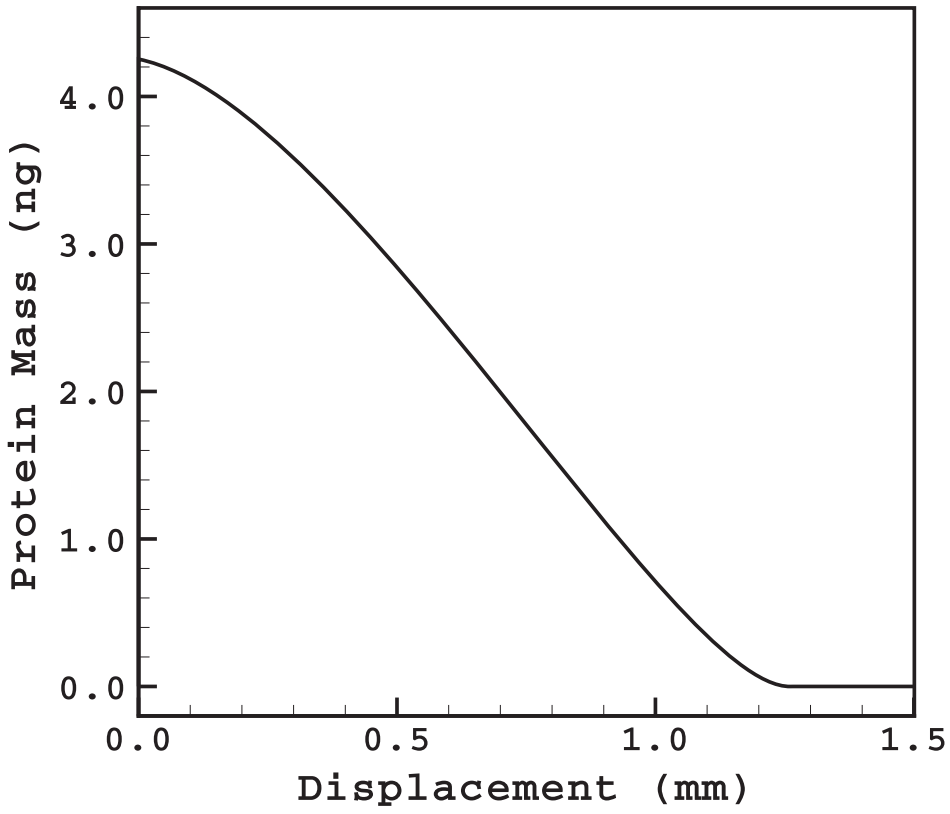

Figure 4.16: BSA mass is shown as a function of microdroplet displacement.

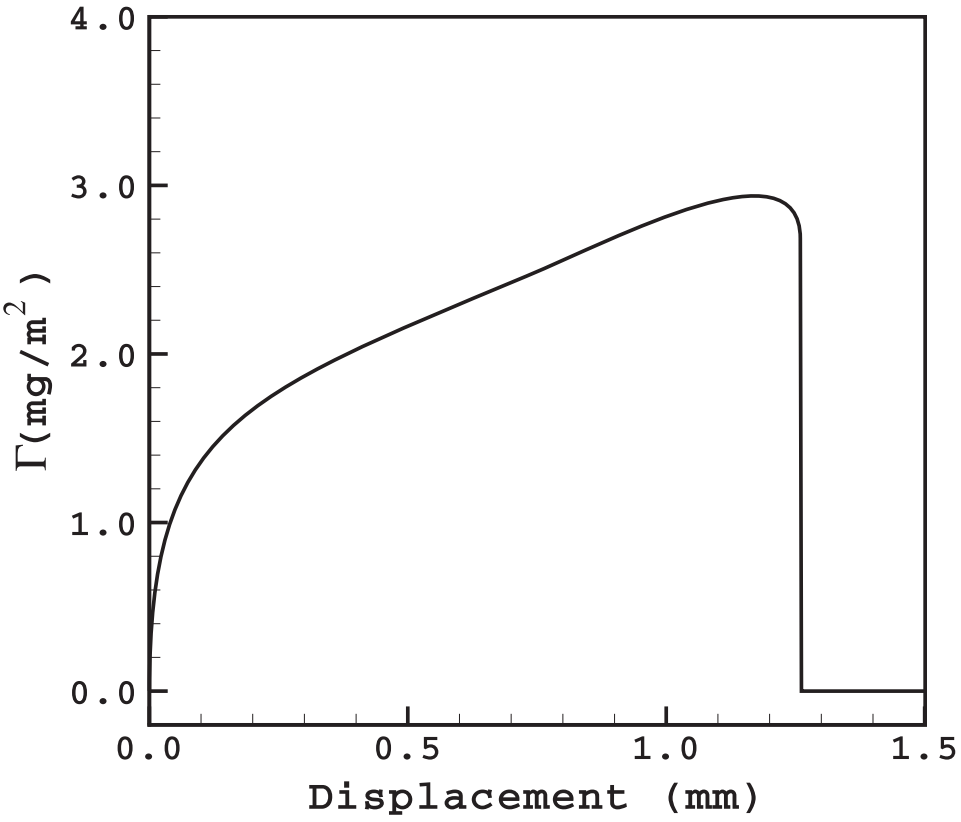

Figure 4.17: The protein surfaceconcentration is shown as a function of microdroplet displacement.

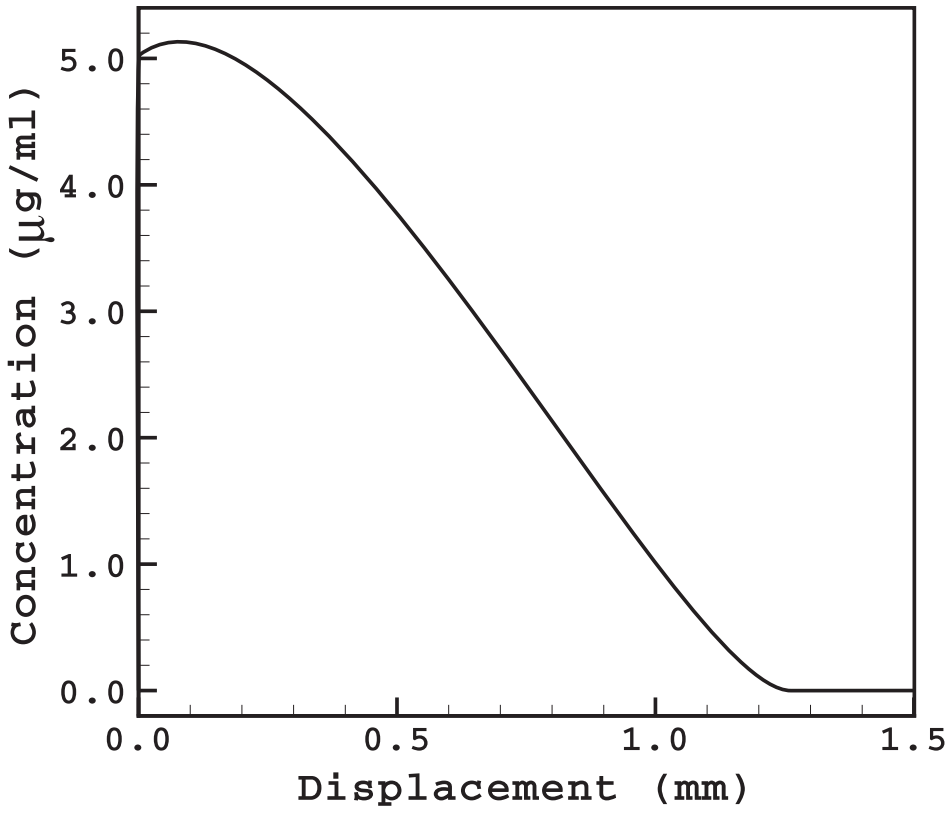

Figure 4.18: The BSA bulk concentration is shown as a function of microdroplet displacement.

4.3 Optimization

In this section, an extensive parametric variation is used to derive the Maximum Actuation Switching Frequency (MASF) for ranges of the microdroplet size, gap spacing between the top and bottom plates and electrode pitch

size. As a result, the scalability of microfluidic devices is investigated, and it is shown that the microdroplet transfer rates change inversely with the microdroplet size (measured based on the microdroplet diameter), and the microdroplet average velocity is nearly the same for different system scales. As a result of this study, an adjustable force-based actuation switching frequency implementation is proposed, and it is shown that faster microdroplet motion is obtained by in-situ adjusting of the switching frequency. Finally, it has been observed that the fastest microdroplet motion, despite similar studies conducted in the literature, is not achieved via actuating the next electrode as soon as the microdroplet touches it. Indeed, the switching frequency spectrum depends on the physical and geometrical properties of the system.

4.3.1 Effects of the microdroplet size

In this section the effects of the microdroplet size on the microdroplet electrohydrodynamics and the Maximum Actuation Switching Frequency (MASF) is studied. The microdroplet motion is modeled for its transport over three electrodes (with an electrode pitch size of $L = 1.5$ mm and gap spacing of $H = 0.3$ mm). The selected applied voltage is 35 V, which is between the upper and lower values of the voltages, 13 V and 40 V (see Figure 4.4). The numerical MASF value calculated for this selected voltage (35 V) is in good agreement with the experimental value. An arbitrary switching frequency of 15 Hz is used. Microdroplets with three different diameters of 1.6 mm, 2.25

mm, and 3 mm are modeled. The results of the model are presented in terms of the microdroplet displacement and driving and opposing forces during its motion. Figures 4.19 and 4.20 presents the behavior of the microdroplet with different sizes under the same actuation conditions. The leading edge position of the microdroplet is shown as a function of time in Figure 4.19. The difference in the initial positions is due to the fact that the microdroplet centre is aligned with the centre of the initial electrode. This is the most common initial position for a stationary microdroplet as it self-centres itself with the initial electrode after dispensing [92]. As it can be seen in Figure 4.19, the smallest microdroplet reaches the last electrode in the shortest time. However, since the same 15 Hz switching frequency is used, the average transport velocity is the same for all of the microdroplet sizes. The driving force for each microdroplet is shown in Figure 4.20 with respect to the leading edge position. The driving forces acting on the larger microdroplets are larger. On the other hand, the opposing forces (i.e., shear, drag and three-phase contact line) increase due to the increased microdroplet mass and surface area. Therefore, the microdroplets move slower as their sizes increase. The results presented reveal the fact that the microdroplet size is a key parameter in determining the microdroplet electrohydrodynamics.

To investigate the relation between the microdroplet size and MASF, transport of three different microdroplet sizes over six electrodes is studied (for the same system as before). Figure 4.21 shows the time required for completing the transport for three different microdroplet sizes as a function of

the switching frequency. For each size, the time required decreases as the switching frequency increases. However, the switching frequency cannot be increased above the defined MASF. Interestingly, MASF strongly depends on the microdroplet size (see Figure 4.21); smaller microdroplets allow for higher MASF values.

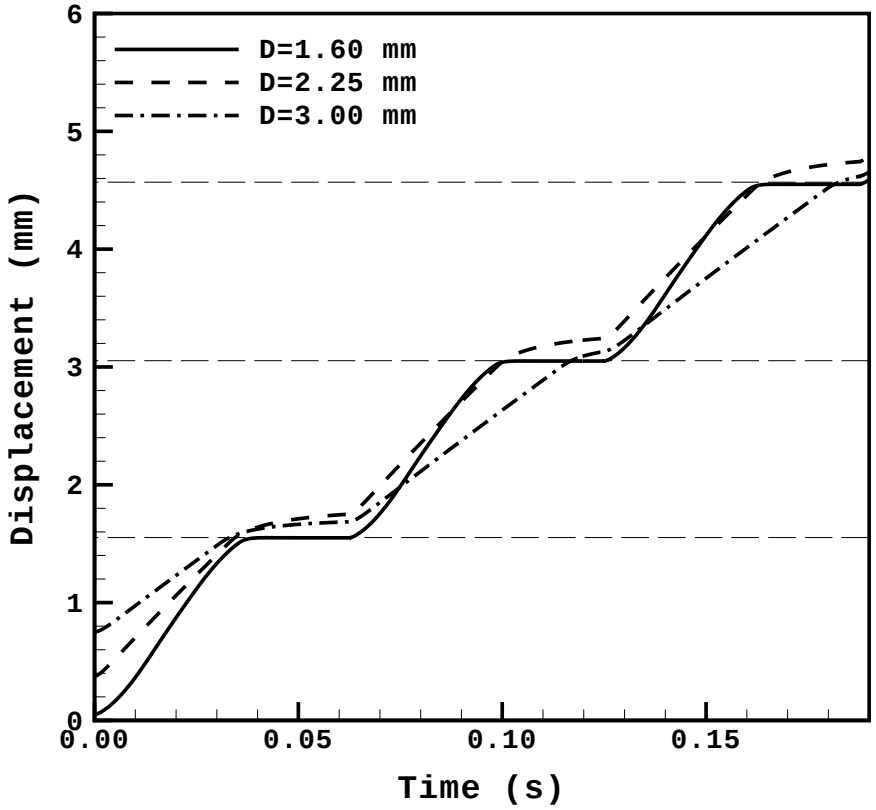

Figure 4.19: The effect of the microdroplet size on electrohydrodynamic properties is shown for three different diameters. The microdroplet leading edge position is shown as a function of time.

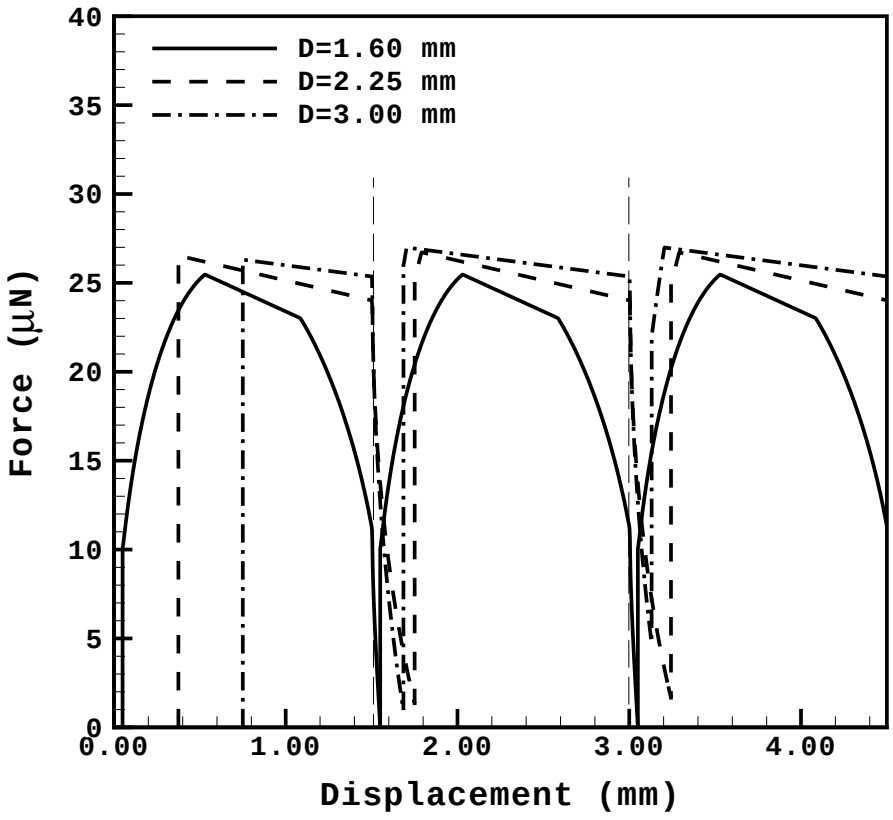

Figure 4.20: The effects of the microdroplet size on electrohydrodynamic properties are shown for three different diameters. The driving force is shown as a function of the microdroplet leading edge position.

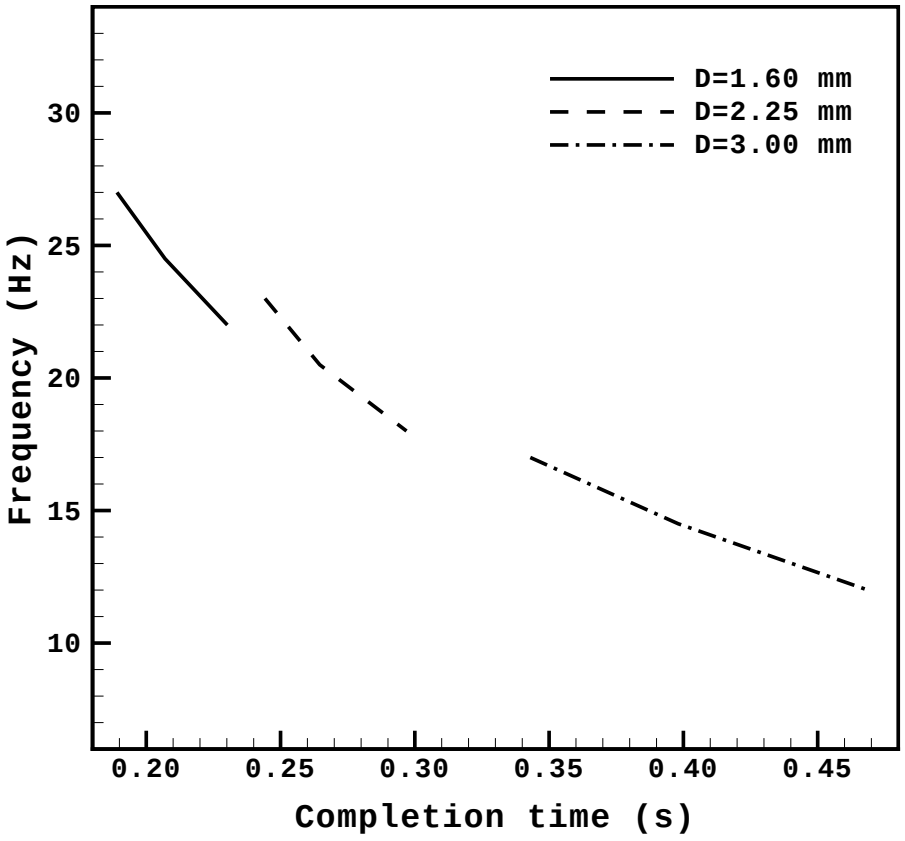

Figure 4.21: The time required to complete the transport over six electrodes is shown as a function of the switching frequency for microdroplets of three different diameters.

4.3.2 Effects of system architecture

The system architecture plays a crucial role in microdroplet dynamics. In essence, structural layers and geometric parameters of the device have the most important effects on the microdroplet motion [95]. In this section the ef-

fects of the gap spacing and electrode pitch size on the MASF are individually analyzed, and scalability of digital microfluidic architectures is investigated. Figure 4.22 shows the MASF versus microdroplet diameter for three different gap spacings (i.e., $H = 0.6$ mm, 0.3 mm and 0.15 mm). The electrode pitch size is kept constant as $L = 1.5$ mm. The results from Figure 4.22 confirm again that as the droplet diameter increases, the MASF value will decrease (for each gap spacing). However, for the same microdroplet diameter, decreases in the gap spacing lead to slower microdroplet motion, due to the resulting increase in the wall force. This is an interesting observation, as it shows that for pre-fabricated top and bottom plates, faster transport can be achieved simply by controlling the gap spacing and the microdroplet volume. The effect of the electrode pitch size on MASF is shown in Figure 4.23. The gap spacing is kept constant at $H = 0.3$ mm. The results show that by decreasing the electrode pitch size the system MASF increases. To determine the effect of the electrode pitch size on the transport velocity, a similar plot is shown in Figure 4.24. Interestingly, by decreasing the electrode pitch size and keeping the gap spacing constant, for the same diameter-electrode pitch size ratio, higher transport velocities can be achieved. This increase in the velocity can be due to the decrease in the shear force because of the reduction in the wetted area. It has been shown before that digital microfluidic structures are highly scalable [14]. The scalable nature of these systems is studied here. Two system designs are modeled: $L = 1.5$ mm and $H = 0.6$ mm; $L = 0.75$ mm and $H = 0.3$ mm. The size of the second design (i.e., the

size of the electrode pitch size and the gap spacing) is half of the size of the first design. Figure 4.25 shows the MASF values of these setups over a range of microdroplet diameter-electrode pitch size ratios (D/L). The MASF of the smaller system is larger than that of the larger system. However, the transport velocity of both systems is the same (see Figure 4.26). This is a very important observation which confirms the scalable nature of digital microfluidic systems.

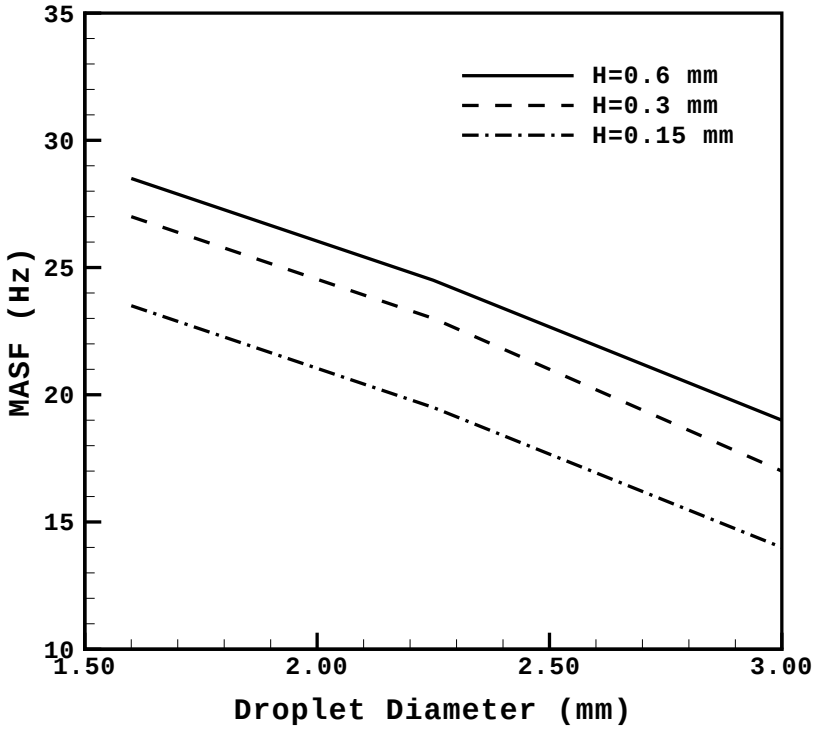

Figure 4.22: MASF is shown for three different gap spacings as a function of microdroplet diameter.

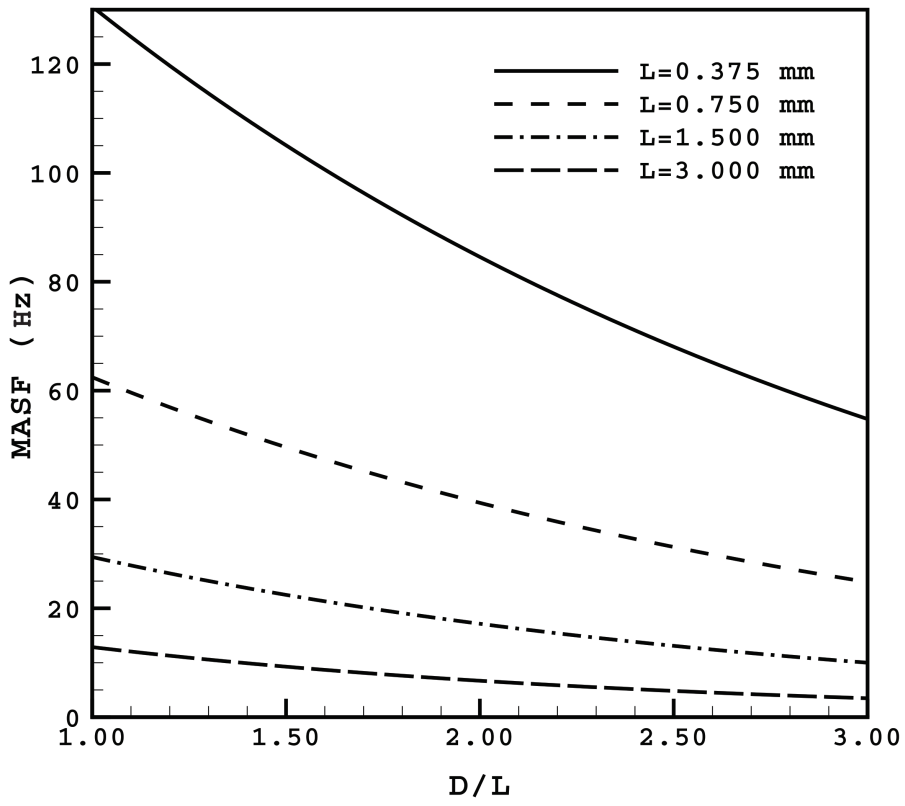

Figure 4.23: The effect of the electrode length on the system MASF is shown.

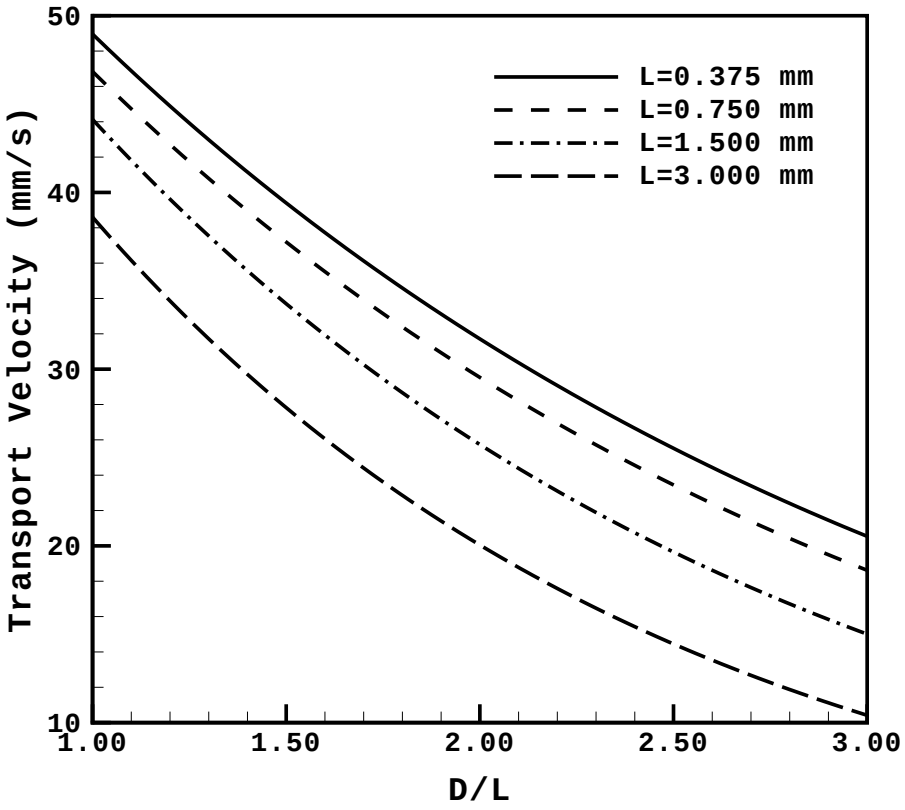

Figure 4.24: The effect of the electrode length on the microdroplet transport velocity is shown. The increase in the transport velocity due to the decrease in the wetted surface area is shown.

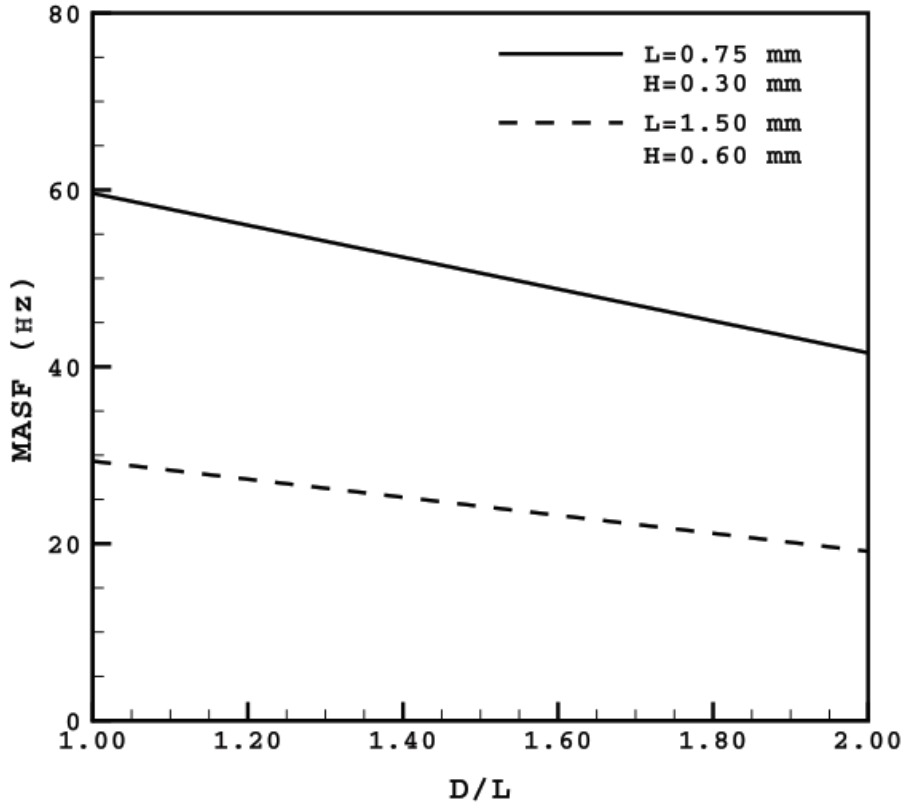

Figure 4.25: The MASF of two designs is shown over a range of microdroplet diameter-electrode pitch size ratios (D/L).

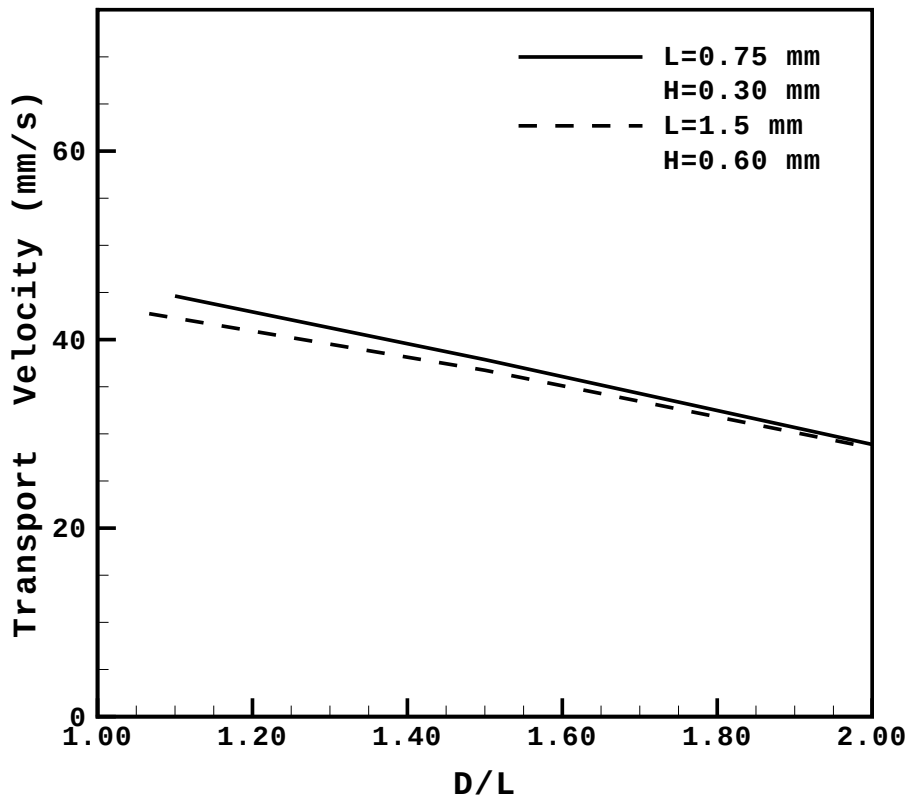

Figure 4.26: The microdroplet transport velocity of two designs over a range of microdroplet diameter-electrode pitch size ratios (D/L) is shown.

4.3.3 Adjustable force-based switching frequency implementation

Constant switching frequency implementation is the simplest actuation algorithm. However, by applying a constant frequency the device will not operate at its optimum throughput and maximum transport velocity. In Figure 4.27 the maximum number of electrodes in which the microdroplet can be transported is shown as a function of the actuation switching frequency. Depending on the constant switching frequency, the microdroplet will ultimately stop after completing its transport over a limited number of electrodes. Adjustable switching frequency algorithms have been proposed to address this issue [108, 109]. Arzpeyma et al. [108] showed that optimum actuation is achieved via actuating the next electrode as soon as the microdroplet touches it. This has been referred to as an adjustable position-based actuation algorithm. In this work a new electrode actuation algorithm is proposed in which actuation is based on finding the maximum force acting on the microdroplet (i.e., adjustable force-based actuation). As it can be seen in Figure 4.28, the proposed algorithm is based on a feedback control submodule which monitors the microdroplet location. After sensing the microdroplet position, the algorithm considers two potential actuation scenarios. This is demonstrated in Figure 4.29. After calculating the driving force using the electrohydrodynamic model for each scenario, the proposed algorithm chooses the optimum actuation scheme which leads to a higher velocity. The performance of the

proposed algorithm was examined with respect to the other methods available (i.e., constant frequency and adjustable position-based frequency). Figure 4.30 presents the results of this comparison. It shows the time required to complete transport over six electrodes as a function of the microdroplet leading edge position for three different algorithms: constant frequency, adjustable position-based frequency and adjustable force-based frequency. It is evident from the results that the adjustable force based frequency results in faster microdroplet motion. It should be noted that both adjustable position-based actuation and adjustable force-based actuation will lead to the same result for the case where the microdroplet diameter is equal to the electrode length.

The in-situ control of microdroplet motion in digital microfluidic systems is a crucial task. Depending on the size of the system, the most suitable switching frequency spectrum has to be found to achieve the highest transport velocity. The adjustable force-based actuation algorithm can achieve this rapid transport.

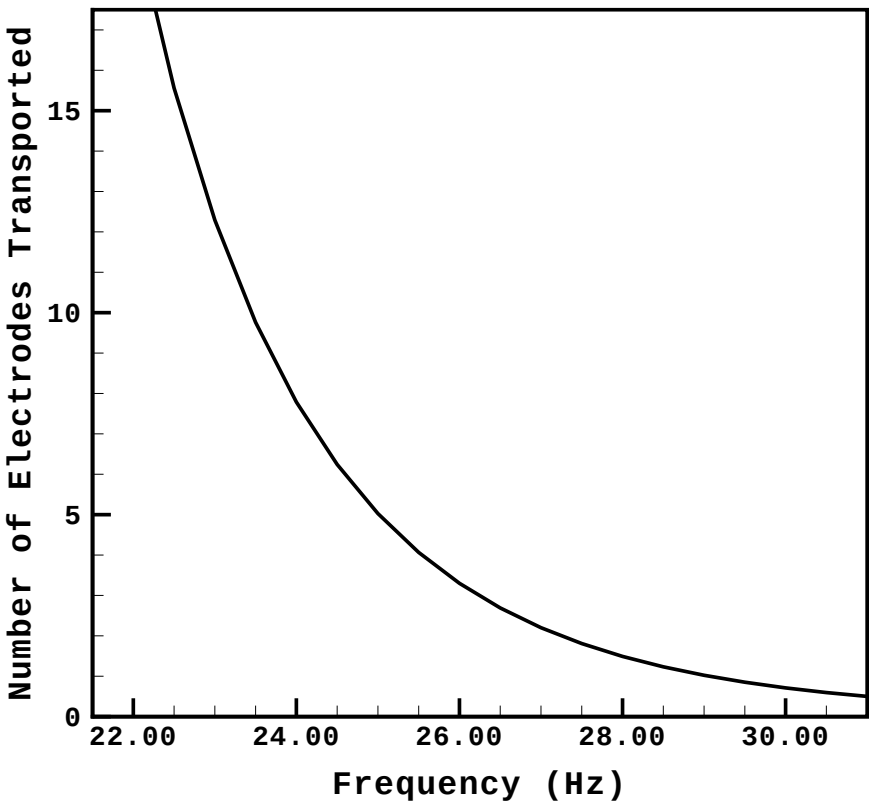

Figure 4.27: The maximum number of electrodes over which the microdroplet can be transported is shown as a function of the actuation switching frequency.

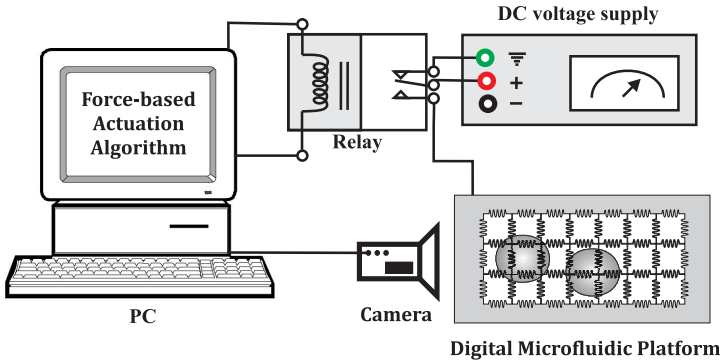

Figure 4.28: The proposed adjustable force-based algorithm is based on a feedback control submodule which monitors the microdroplet location.

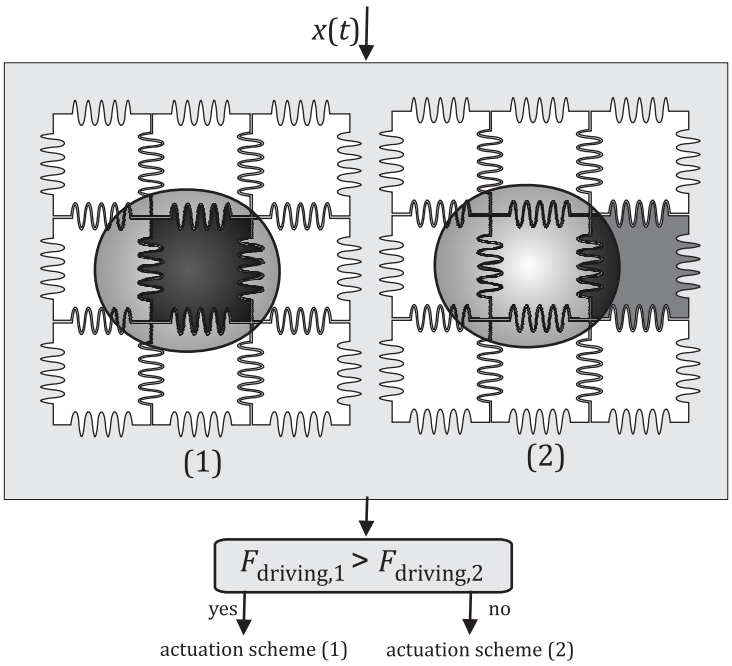

Figure 4.29: The algorithm considers two potential actuation scenarios. After calculating the driving force using the electrohydrodynamic model for each scenario, the proposed algorithm chooses the optimum actuation scheme which leads to a higher velocity.

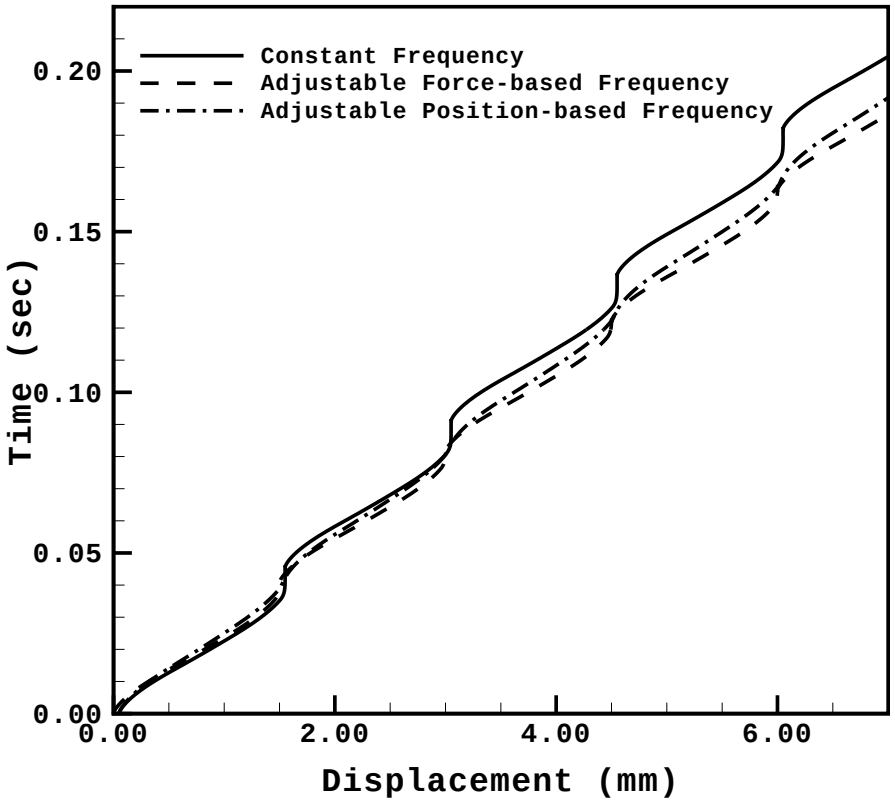

Figure 4.30: The time required to complete the transport over six electrodes is shown as a function of the microdroplet leading edge position for three different algorithms: constant frequency, adjustable position-based frequency and adjustable force-based frequency.

Chapter 5

Conclusions and Future Work

In this thesis, an electrohydrodynamic approach was used to model the microdroplet motion in electrocapillary-based digital microfluidic systems. Different physicochemical phenomena influencing the microdroplet dynamics such as electrostatics, hydrodynamics, evaporation and biomolecular adsorption, were accurately modeled, and the individual and combined effects of each phenomenon were investigated. Ultimately, the developed model was used to optimize the microdroplet motion and the overall design of the device.

5.1 Conclusions

- **Numerical scheme** - The Finite Voulme Method (FVM) has been extensively used in solving the fluid dynamic governing equations. In this thesis, the concepts of the FVM were employed to develop a new numerical scheme for solving the electrostatic and hydrodynamic equations inside the microdroplet and the filler fluid. The analysis provided important findings on the developed scheme are the electrostatic and hydrodynamic pressures as well as the velocity field.

- **Moving boundary** - The calculated electrostatic and hydrodynamic pressures were used to determine the microdroplet shape, and a new method based on the concept of Volume of Fluid (VOF) was developed to model the microdroplet moving boundary. Moreover, Frenkel-Eyring activated rate theory of transport in liquids was used to relate the static and dynamic contact angles, and correct the boundary conditions.

- **Hydrodynamics** - The developed electrohydrodynamic model is capable of capturing the hydrodynamic vortices inside a microdroplet which (despite the reports from similar studies in literature) highlights the multi-dimensional nature of the fluid flow inside a microdroplet. Moreover, a new method for calculating the filler force was developed which was based on integrating the hydrodynamic pressure along the microdroplet-filler interface.

- **Evaporation** - A new model based on the Fick's law was developed for simulating the microdroplet evaporation. The effects of the evaporation were included by considering an additional force term in the dynamic equation and the mass loss (and the resulting change in the microdroplet radius). The modeling results indicate that mass loss due to evaporation tends to accelerate the droplet, whereas the competitive effect of the reduced driving force decelerates it. It was observed that mass loss due to the evaporation plays a crucial role in determining the microdroplet dynamics.

- **Adsorption** - The effects of protein adsorption were modeled by adding a new force to the dynamic equation of the microdroplet motion. The Ward and Tordai equation was used to model the diffusion-controlled protein adsorption. The adsorption rate was then related to the change in the interfacial tensions and the capacitance of the underlying layers. Moreover, to obtain the saturated capacitance (which is a key parameter in the adsorption model), a new capacitance sampling procedure was proposed and successfully tested.

- **Optimization** - The proposed methodology provides a vital tool for the design and control processes and can be used for numerous applications that require optimum routing and high transport velocities. The modeling results shows that for prefabricated top and bottom plates, faster transport can be achieved simply by controlling the gap spacing and the microdroplet volume. It was also shown that constant switching frequency algorithms can lead the microdroplet to ultimately stop after completing its transport over a limited number of electrodes. Therefore, a force-based adjustable switching frequency was proposed and implemented. Compared to the constant frequency and adjustable position-based algorithms, the proposed adjustable forced-based algorithm provides higher velocities.

5.2 Future work

- It was observed that the three-phase contact line force, F_{tpcl}, is the largest resistance force, and a semi-empirical relation was used to estimate this force. This estimation can be improved in future work using molecular kinetic theory for an accurate estimation of this force.

- The pseudo-three-dimensional approach used in this thesis can be extended to a three-dimensional analysis. The three-dimensional analysis will be capable of predicting microdroplet boundaries and simultaneous motion of multiple microdroplets. Moreover, different microdroplet operations such as merging, mixing and splitting can be modeled using such a three-dimensional approach.

- Hysteresis effects play a crucial role at the verge of the microdroplet motion. Therefore, an accurate estimation of the hysteresis voltage for different systems can offer higher accuracy for future investigations.

- The developed model is capable of capturing the fluid motion inside the microdroplet. Substrate coating has been proposed as one of the potential applications of the digital microfluidic systems, and the quality of the coating operation depends on the internal fluid flow. The developed model can be used to optimize such coating processes. This task can be performed by controlling the microdroplet speed and the resulting internal flow.

- To avoid the trial-and-error design processes, the developed model can be used to predict the behavior of different materials and fluids (e.g., non-polar and low surface tension liquids).

- In this thesis the microdroplet was assumed to be conductive. However, the proposed model, with slight modification can be used for a wide array of fluid. In fact, one of the main advantages of the electyro-hydrodynamic approach is its applicability to be applicable to systems with dielectric droplets.

Bibliography

[1] A. Ahmadi, J. F. Holzman, H. Najjaran, and M. Hoorfar. Electrohydrodynamic modeling of microdroplet transient dynamics in electrocapillary-based digital microfluidic devices. *Microfluidics and Nanofluidics*, 10(5):1019–1032, 2011.

[2] A. Ahmadi, H. Najjaran, J. F. Holzman, and M. Hoorfar. Two-dimensional flow dynamics in digital microfluidic systems. *Journal of Micromechanics and Microengineering*, 19:065003–1–065003–7, 2009.

[3] J. Nichols, A. Ahmadi, M. Hoorfar, H. Najjaran, and J. F. Holzman. Micro-drop actuation using multiplexer structures. In *Proceedings of International Conference on Nanochannels, Microchannels, and Minichannels*, pages 1085–1092, 2008.

[4] A. Ahmadi, H. Najjaran, J. Holzman, and M. Hoorfar. Numerical modeling of microdrop motion on digital microfluidic multiplexer. In *Proceedings of Nanotech Conference*, volume 3, pages 561–564, Boston, USA, 2008 2008.

[5] A. Ahmadi, J. F. Holzman, H. Najjaran, and M. Hoorfar. Numeri-

cal multiphysics modeling of microdroplet motion dynamics in digital microfluidic systems. In *Proceedings of International Conference on Nanochannels, Microchannels, and Minichannels*, pages 30754–30754, 2010 2010.

[6] A. Ahmadi and M. Hoorfar. Dynamics of evaporating microdroplets in digital microfluidic biochips. In *Proceedings of 23rd Canadian Congress of Applied Mechanics*, June 2011 2011.

[7] A. Ahmadi and M. Hoorfar. Numerical investigation of the combined effects of biomlecular adsorption and microdroplet evaporation on the performance of the electrocapillary-based digital microfluidic systems. In *Proceedings of The Ninth International Conference on Nanochannels, Microchannels, and Minichannels*. ASME, 2011 2011.

[8] A. Ahmadi, K. D. Devlin, H. Najjaran, J. F. Holzman, and M. Hoorfar. Biomolecular adsorption phenomena in electrowetting-based digital microfluidic devices. In *Proceedings of Nanotech Conference*, volume 2, pages 452–455, Anaheim, USA, 2010 2010.

[9] A. Ahmadi, K. D. Devlin, and M. Hoorfar. Numerical study of the microdroplet actuation switching frequency in digital microfluidic biochips. *Microfluidics and Nanofluidics (DOI) 10.1007/s10404-011-0872-8*, 2011.

[10] A. Ahmadi, K. D. Devlin, H. Najjaran, J. F. Holzman, and M. Hoorfar.

In situ characterization of microdroplet interfacial properties in digital microfluidic systems. *Lab On a Chip*, 10(11):1429–1435, 2010.

[11] K. D. Devlin, A. Ahmadi, H. Najjaran, J. F. Holzman, and M. Hoorfar. Dynamic sampling in digital microfluidic devices. In *Proceedings of SPIE*, volume 7679, pages 7679–76790C, Orlando, USA, 2010 2010.

[12] J. Nichols, A. Ahmadi, M. Hoorfar, H. Najjaran, and J. F. Holzman. In situ digital microfluidic conductance sampling. *Sensors and Actuators: A.Physical*, 152(1):13–20, 2009.

[13] A. Ahmadi, J. Nichols, M. Hoorfar, H. Najjaran, and J. F. Holzman. Digital implementations for integrated microfluidic sensing. In *Proceedings of SPIE*, volume 7318, pages 73181C–1–73181C–9, Orlando, USA, 2009 2009.

[14] M. G. Pollack, A. D. Shenderov, and R. B. Fair. Electrowetting-based actuation of droplets for integrated microfluidics. *Lab on a Chip*, 2(2):96–101, 2002.

[15] A. Ahmadi, H. Najjaran, J. F. Holzman, and M. Hoorfar. Two-dimensional flow dynamics in digital microfluidic systems. *Journal of Micromechanics and Microengineering*, 19(6):065003, 2009.

[16] J. Y. Yoon and R. L. Garrell. Preventing biomolecular adsorption in electrowetting-based biofluidic chips. *Analytical Chemistry*, 75(19):5097–5102, 2003.

[17] S. Haeberle and R. Zengerle. Microfluidic platforms for lab-on-a-chip applications. *Lab on a Chip*, 7(9):1094–1110, 2007.

[18] C. D. Chin, V. Linder, and S. K. Sia. Lab-on-a-chip devices for global health: past studies and future opportunities. *Lab on a Chip*, 7(1):41–57, 2007.

[19] N. Bontoux, L. Dauphinot, T. Vitalis, V. Studer, Y. Chen, J. Rossier, and M. C. Potier. Integrating whole transcriptome assays on a lab-on-a-chip for single cell gene profiling. *Lab on a Chip*, 8(3):443–450, 2008.

[20] H. Minhas. Lab on a chip10 years and flowing strong. *Lab on a Chip*, 10(17):2189–2189, 2010.

[21] H. Becker and C. Grtner. Polymer microfabrication technologies for microfluidic systems. *Analytical and Bioanalytical Chemistry*, 390(1):89–111, 2008.

[22] D. B. Weibel, W. R. DiLuzio, and G. M. Whitesides. Microfabrication meets microbiology. *Nature Reviews Microbiology*, 5(3):209–218, 2007.

[23] T. Tsuchizawa, K. Yamada, H. Fukuda, T. Watanabe, J. Takahashi, M. Takahashi, T. Shoji, E. Tamechika, S. Itabashi, and H. Morita. Microphotonics devices based on silicon microfabrication technology. *IEEE Journal on Selected Topics in Quantum Electronics*, 11(1):232–240, 2005.

[24] D. Erickson and D. Li. Integrated microfluidic devices. *Analytica Chimica Acta*, 507(1):11–26, 2004.

[25] P. S. Dittrich and A. Manz. Lab-on-a-chip: microfluidics in drug discovery. *Nature Reviews Drug Discovery*, 5(3):210, 2006.

[26] P. Gravesen, J. Branebjerg, and O. S. Jensen. Microfluidics-a review. *Journal of Micromechanics and Microengineering*, 3:168–182, 1993.

[27] P. C. H. Li and P. H. Li. *Microfluidic Lab-On-A-Chip for Chemical and Biological Analysis and Discovery*. CRC Press, New York, 1st edition, 2006.

[28] S. Shojitt and M. Esashit. Microflow devices and systems. *Journal of Micromechanics and Microengineering*, 4:157–171, 1994.

[29] P. Tabeling. *Introduction to microfluidics*. Oxford University Press, New York, 2005.

[30] S. Y. Teh, R. Lin, L. H. Hung, and A. P. Lee. Droplet microfluidics. *Lab on a Chip*, 8(2):198–220, 2008.

[31] M. Washizu. Electrostatic actuation of liquid droplets for microreactorapplications. *Industry Applications, IEEE Transactions on*, 34(4):732–737, 1998.

[32] M. G. Pollack, R. B. Fair, and A. D. Shenderov. Electrowetting-

based actuation of liquid droplets for microfluidic applications. *Applied Physics Letters*, 77(11):1725–1726, 2000.

[33] J. Lee, H. Moon, J. Fowler, T. Schoellhammer, and C. J. Kim. Electrowetting and electrowetting-on-dielectric for microscale liquid handling. *Sensors and Actuators A: Physical*, 95(2-3):259–268, 2002.

[34] V. Srinivasan, V. K. Pamula, and R. B. Fair. An integrated digital microfluidic lab-on-a-chip for clinical diagnostics on human physiological fluids. *Lab on a Chip*, 4(4):310–315, 2004.

[35] A. R. Wheeler, H. Moon, C. A. Bird, R. R. O. Loo, C. J. Kim, J. A. Loo, and R. L. Garrell. Digital microfluidics with in-line sample purification for proteomics analyses with maldi-ms. *Analytical Chemistry*, 77(2):534–540, 2005.

[36] Y. H. Chang, G. B. Lee, F. C. Huang, Y. Y. Chen, and J. L. Lin. Integrated polymerase chain reaction chips utilizing digital microfluidics. *Biomedical Microdevices*, 8(3):215–225, 2006.

[37] H. Moon, A. R. Wheeler, R. L. Garrell, J. A. Loo, and C. J. Kim. An integrated digital microfluidic chip for multiplexed proteomic sample preparation and analysis by maldi-ms. *Lab on a Chip*, 6(9):1213–1219, 2006.

[38] R. B. Fair, A. Khlystov, T. D. Tailor, V. Ivanov, R. D. Evans, P. B. Griffin, V. Srinivasan, V. K. Pamula, M. G. Pollack, and J. Zhou.

Chemical and biological applications of digital-microfluidic devices. *IEEE Design and Test of Computers*, 24(1):10–24, 2007.

[39] K. P. Nichols and H. J. G. E. Gardeniers. A digital microfluidic system for the investigation of pre-steady-state enzyme kinetics using rapid quenching with maldi-tof mass spectrometry. *Analytical Chemistry*, 79(22):8699–8704, 2007.

[40] E. M. Miller and A. R. Wheeler. A digital microfluidic approach to homogeneous enzyme assays. *Analytical Chemistry*, 80(5):1614–1619, 2008.

[41] R. Sista, Z. Hua, P. Thwar, A. Sudarsan, V. Srinivasan, A. Eckhardt, M. Pollack, and V. Pamula. Development of a digital microfluidic platform for point of care testing. *Lab on a Chip*, 8(12):2091–Lab on a Chip, 2008.

[42] M. J. Jebrail and A. R. Wheeler. Digital microfluidic method for protein extraction by precipitation. *Analytical Chemistry*, 81(1):330–335, 2009.

[43] V. N. Luk and A. R. Wheeler. A digital microfluidic approach to proteomic sample processing. *Analytical Chemistry*, 81(11):4524–4530, 2009.

[44] Z. Hua, J. L. Rouse, A. E. Eckhardt, V. Srinivasan, V. K. Pamula, W. A. Schell, J. L. Benton, T. G. Mitchell, and M. G. Pollack. Mul-

tiplexed real-time polymerase chain reaction on a digital microfluidic platform. *Analytical Chemistry*, 82(6):2310–2316, 2010.

[45] L. Malic, D. Brassard, T. Veres, and M. Tabrizian. Integration and detection of biochemical assays in digital microfluidic loc devices. *Lab on a Chip*, 10(4):418–431, 2010.

[46] H. Moon, S. K. Cho, and R. L. Garrell. Low voltage electrowetting-on-dielectric. *Journal of Applied Physics*, 92(7):4080–4087, 2002.

[47] S. K. Cho, H. Moon, and C. J. Kim. Creating, transporting, cutting, and merging liquid droplets by electrowetting-based actuation for digital microfluidic circuits. *Journal of Microelectromechanical Systems*, 12(1):70–80, 2003.

[48] C. G. Cooney, C. Y. Chen, M. R. Emerling, A. Nadim, and J. D. Sterling. Electrowetting droplet microfluidics on a single planar surface. *Microfluidics and Nanofluidics*, 2(5):435–446, 2006.

[49] M. Abdelgawad, S. L. S. Freire, H. Yang, and A. R. Wheeler. All-terrain droplet actuation. *Lab on a Chip*, 8(5):672–677, 2008.

[50] A. R. Wheeler, H. Moon, C. A. Bird, R. R. O. Loo, C. J. Kim, J. A. Loo, and R. L. Garrell. Digital microfluidics with in-line sample purification for proteomics analyses with maldi-ms. *Analytical Chemistry*, 77(2):534–540, 2005.

[51] M. Abdelgawad and A. R. Wheeler. The digital revolution: a new paradigm for microfluidics. *Advanced Materials*, 21(8):920–925, 2009.

[52] M. W. L. Watson, M. Abdelgawad, G. Ye, N. Yonson, J. Trottier, and A. R. Wheeler. Microcontact printing-based fabrication of digital microfluidic devices. *Anal.Chem*, 78(22):7877–7885, 2006.

[53] M. Abdelgawad and A. R. Wheeler. Rapid prototyping in copper substrates for digital microfluidics. *Advanced Material*, 19:133–137, 2007.

[54] M. Abdelgawad and A. R. Wheeler. Low-cost, rapid-prototyping of digital microfluidics devices. *Microfluidics and Nanofluidics*, 4(4):349–355, 2008.

[55] S. K. Fan, C. Hashi, and C. J. Kim. Manipulation of multiple droplets on n/spl times/m grid by cross-reference ewod driving scheme and pressure-contact packaging. In *The Sixteenth Annual International Conference on Micro Electro Mechanical Systems*, pages 694–697, 2003 2003.

[56] J. Gong and C. J. Kim. All-electronic droplet generation on-chip with real-time feedback control for ewod digital microfluidics. *Lab on a Chip*, 8(6):898–906, 2008.

[57] P. Y. Chiou, Z. Chang, and M. C. Wu. Droplet manipulation with light on optoelectrowetting device. *Journal of Microelectromechanical Systems*, 17(1):133–138, 2008.

[58] B. S. Gallardo, V. K. Gupta, F. D. Eagerton, L. I. Jong, V. S. Craig, R. R. Shah, and N. L. Abbott. Electrochemical principles for active control of liquids on submillimeter scales. *Science*, 283(5398):57–60, 1999.

[59] K. Ichimura, S. K. Oh, and M. Nakagawa. Light-driven motion of liquids on a photoresponsive surface. *Science*, 288(5471):1624–1626, 2000.

[60] M. A. Burns, C. H. Mastrangelo, T. S. Sammarco, F. P. Man, J. R. Webster, B. N. Johnson, B. Foerster, D. Jones, Y. Fields, and A. R. Kaiser. Microfabricated structures for integrated dna analysis. *Proceedings of the National Academy of Sciences of the United States of America*, 93(11):5556–5561, 1996.

[61] T. S. Sammarco and M. A. Burns. Thermocapillary pumping of discrete drops in microfabricated analysis devices. *AICHE Journal*, 45(2):350–366, 1999.

[62] A. Wixforth. Acoustically driven planar microfluidics. *Superlattices and Microstructures*, 33(5-6):389–396, 2003.

[63] T. B. Jones, M. Gunji, M. Washizu, and M. J. Feldman. Dielectrophoretic liquid actuation and nanodroplet formation. *Journal of Applied Physics*, 89(2):1441–1448, 2001.

[64] M. Washizu. Electrostatic actuation of liquid droplets for micro-reactorapplications. *IEEE Transactions on Industry Applications*, 34(4):732–737, 1998.

[65] G. Beni and S. Hackwood. Electrowetting displays. *Applied Physics Letters*, 38:207–209, 1981.

[66] G. Beni and M. A. Tenan. Dynamics of electrowetting displays. *Journal of Applied Physics*, 52:6011–6015, 1981.

[67] E. Colgate and H. Matsumoto. An investigation of electrowetting-based microactuation. *Journal of Vacuum Science and Technology A: Vacuum, Surfaces, and Films*, 8:3625–3633, 1990.

[68] B. Berge. Electrocapillarite et mouillage de films isolants par l'eau. *Comptes rendus de l'Acadmie des sciences.Srie 2, Mcanique, Physique, Chimie, Sciences de l'univers, Sciences de la Terre*, 317(2):157–163, 1993.

[69] J. A. M. Sondag-Huethorst and L. G. J. Fokkink. Potential-dependent wetting of electroactive ferrocene-terminated alkanethiolate monolayers on gold. *Langmuir*, 10(11):4380–4387, 1994.

[70] M. Vallet, B. Berge, and L. Vovelle. Electrowetting of water and aqueous solutions on poly (ethylene terephthalate) insulating films. *Polymer*, 37(12):2465–2470, 1996.

[71] W. J. J. Welters and L. G. J. Fokkink. Fast electrically switchable capillary effects. *Langmuir*, 14(7):1535–1538, 1998.

[72] H. J. J. Verheijen and M. W. J. Prins. Reversible electrowetting and trapping of charge: Model and experiments. *Langmuir*, 15(20):6616–6620, 1999.

[73] V. Peykov, A. Quinn, and J. Ralston. Electrowetting: a model for contact-angle saturation. *Colloid and polymer science*, 278(8):789–793, 2000.

[74] C. B. Gorman, H. A. Biebuyck, and G. M. Whitesides. Control of the shape of liquid lenses on a modified gold surface using an applied electrical potential across a self-assembled monolayer. *Langmuir*, 11(6):2242–2246, 1995.

[75] B. Berge and J. Peseux. Variable focal lens controlled by an external voltage: An application of electrowetting. *The European Physical Journal E-Soft Matter*, 3(2):159–163, 2000.

[76] M. W. J. Prins, W. J. J. Welters, and J. W. Weekamp. Fluid control in multichannel sructures by electrocapillary pessure. *Science*, 291(5502):277–280, 2001.

[77] E. Seyrat and R. A. Hayes. Amorphous fluoropolymers as insulators for reversible low-voltage electrowetting. *Journal of Applied Physics*, 90:1383–1386, 2001.

[78] C. Quilliet and B. Berge. Electrowetting: a recent outbreak. *Current Opinion in Colloid and Interface Science*, 6(1):34–39, 2001.

[79] B. Berge. lectrocapillarit et mouillage de films isolants par l'eau= electrocapillarity and wetting of insulator films by water. *Comptes rendus de l'Acadmie des sciences*, 317(2):157–163, 1993.

[80] M. Vallet, B. Berge, and L. Vovelle. Electrowetting of water and aqueous solutions on poly (ethylene terephthalate) insulating films. *Polymer*, 37(12):2465–2470, 1996.

[81] J. Lee and C. J. Kim. Surface-tension-driven microactuation based on continuous electrowetting. *Journal of Microelectromechanical Systems*, 9(2):171–180, 2000.

[82] F. Mugele and J. C. Baret. Electrowetting: from basics to applications. *Journal of Physics: Condensed Matter*, 17(28):R705–R774, 2005.

[83] S. K. Cho, S. K. Fan, H. Moon, and C. J. Kim. Towards digital microfluidic circuits: Creating, transporting, cutting and merging liquid droplets by electrowetting-based actuation. In *The Fifteenth IEEE International Conference on Micro Electro Mechanical Systems*, pages 32–35, Las Vegas, NV , USA, 2002.

[84] V. N. Luk, G. C. H. Mo, and A. R. Wheeler. Pluronic additives: A solution to sticky problems in digital microfluidics. *Langmuir*, 24(12):6382–6389, 2008.

[85] Y. H. Chang, G. B. Lee, F. C. Huang, Y. Y. Chen, and J. L. Lin. Integrated polymerase chain reaction chips utilizing digital microfluidics. *Biomedical Microdevices*, 8(3):215–225, 2006.

[86] A. R. Wheeler, H. Moon, C. J. Kim, J. A. Loo, and R. L. Garrell. Electrowetting-based microfluidics for analysis of peptides and proteins by matrix-assisted laser desorption/ionization mass spectrometry. *Analytical Chemistry*, 76(16):4833–4838, 2004.

[87] I. Barbulovic-Nad, H. Yang, P. S. Park, and A. R. Wheeler. Digital microfluidics for cell-based assays. *Lab on a Chip*, 8(4):519–526, 2008.

[88] J. Zhou, L. Lu, K. Byrapogu, D. Wootton, P. Lelkes, and R. Fair. Electrowetting based multi-microfluidics array printing of high resolution tissue construct with embedded cells and growth factors. *Virtual and Rapid Manufacturing*, page 265, 2007.

[89] S. K. Fan, P. W. Huang, T. T. Wang, and Y. H. Peng. Cross-scale electric manipulations of cells and droplets by frequency-modulated dielectrophoresis and electrowetting. *Lab on a Chip*, 8(8):1325–1331, 2008.

[90] R. S. Sista, A. E. Eckhardt, V. Srinivasan, M. G. Pollack, S. Palanki, and V. K. Pamula. Heterogeneous immunoassays using magnetic beads on a digital microfluidic platform. *Lab on a Chip*, 8(12):2188–2196, 2008.

[91] F. Su, W. Hwang, and K. Chakrabarty. Droplet routing in the synthesis of digital microfluidic biochips. In *Proceedings of the conference on Design, automation and test in Europe: Proceedings*, pages 323–328, Munich, Germany, 2006 2006. European Design and Automation Association.

[92] R. B. Fair. Digital microfluidics: is a true lab-on-a-chip possible? *Microfluidics and Nanofluidics*, 3(3):245–281, 2007.

[93] B. Bhattacharjee and H. Najjaran. Simulation of droplet position control in digital microfluidic systems. *Journal of Dynamic Systems, Measurement, and Control*, 132(1):014501–3, 2010.

[94] E. Baird, P. Young, and K. Mohseni. Electrostatic force calculation for an ewod-actuated droplet. *Microfluidics and Nanofluidics*, 3(6):635–644, 2007.

[95] H. Ren, R. B. Fair, M. G. Pollack, and E. J. Shaughnessy. Dynamics of electro-wetting droplet transport. *Sensors and Actuators B: Chemical*, 87(1):201–206, 2002.

[96] V. Bahadur and S. V. Garimella. An energy-based model for electrowetting-induced droplet actuation. *Journal of Micromechanics and Microengineering*, 16(8):1494–1503, 2006.

[97] N. Kumari, V. Bahadur, and S. V. Garimella. Electrical actuation of

dielectric droplets. *Journal of Micromechanics and Microengineering*, 18(8):5018, 2008.

[98] M. Vallet, M. Vallade, and B. Berge. Limiting phenomena for the spreading of water on polymer films by electrowetting. *The European Physical Journal B-Condensed Matter*, 11(4):583–591, 1999.

[99] E. S. Baird and K. Mohseni. A unified velocity model for digital microfluidics. *Nanoscale and microscale thermophysical engineering*, 11(1-2):109–120, 2007.

[100] D. Chatterjee, H. Shepherd, and R. L. Garrell. Electromechanical model for actuating liquids in a two-plate droplet microfluidic device. *Lab on a Chip*, 9(9):1219–1229, 2009.

[101] J. S. Kuo, P. Spicar-Mihalic, I. Rodriguez, and D. T. Chiu. Electrowetting-induced droplet movement in an immiscible medium. *Langmuir*, 19(2):250–255, 2003.

[102] S. W. Walker, B. Shapiro, and R. H. Nochetto. Electrowetting with contact line pinning: Computational modeling and comparisons with experiments. *Physics of Fluids*, 21:102103–1–102103–16, 2009.

[103] RB Fair. Scaling fundamentals and applications of digital microfluidic microsystems. *Microfluidics Based Microsystems*, pages 285–304, 2010.

[104] S. W. Walker and B. Shapiro. Modeling the fluid dynamics of elec-

trowetting on dielectric (ewod). *Journal of Microelectromechanical Systems*, 15(4):986–1000, 2006.

[105] L. Clime, D. Brassard, and T. Veres. Numerical modeling of electrowetting processes in digital microfluidic devices. *Computers and Fluids*, 2010.

[106] L. Clime, D. Brassard, and T. Veres. Numerical modeling of electrowetting transport processes for digital microfluidics. *Microfluidics and Nanofluidics*, 8(5):599–608, 2010.

[107] Z. Keshavarz-Motamed, L. Kadem, and A. Dolatabadi. Effects of dynamic contact angle on numerical modeling of electrowetting in parallel plate microchannels. *Microfluidics and Nanofluidics*, 8(1):47–56, 2010.

[108] A. Arzpeyma, S. Bhaseen, A. Dolatabadi, and P. Wood-Adams. A coupled electro-hydrodynamic numerical modeling of droplet actuation by electrowetting. *Colloids and Surfaces A: Physicochemical and Engineering Aspects*, 323(1-3):28–35, 2008.

[109] H. SadAbadi, M. Packirisamy, A. Dolatabadi, and R. Wuthrich. Effects of electrode switching sequence on ewod droplet manipulation: a simulation study. In *Proceedings of the ASME FEDSM-ICNMM*, volume 31212, pages 1–6, 2010.

[110] T. B. Jones. On the relationship of dielectrophoresis and electrowetting. *Langmuir*, 18(11):4437–4443, 2002.

[111] K. H. Kang. How electrostatic fields change contact angle in electrowetting. *Langmuir*, 18(26):10318–10322, 2002.

[112] J. Berthier. *Microdrops and digital microfluidics*. William Andrew Publishing, 2008.

[113] S. Afkhami and M. Bussmann. Height functions for applying contact angles to 2d vof simulations. *International Journal for Numerical Methods in Fluids*, 57(4):453–472, 2008.

[114] TD Blake and J. De Coninck. The influence of solidliquid interactions on dynamic wetting. *Advances in Colloid and Interface Science*, 96(1-3):21–36, 2002.

[115] K. S. Birdi, D. T. Vu, and A. Winter. A study of the evaporation rates of small water drops placed on a solid surface. *The Journal of physical chemistry*, 93(9):3702–3703, 1989.

[116] A. F. H. Ward and L. Tordai. Timedependence of boundary tensions of solutions i. the role of diffusion in timeeffects. *The Journal of chemical physics*, 14:453–461, 1946.

[117] T. B. Jones. An electromechanical interpretation of electrowetting. *Journal of Micromechanics and Microengineering*, 15(6):1184–1187, 2005.

[118] E. M. Lifshitz, L. D. Landau, and L. P. Pitaevskii. *Electrodynamics of continuous media*. Pergamon Press, 1984.

[119] S. K. Thamida and H. C. Chang. Nonlinear electrokinetic ejection and entrainment due to polarization at nearly insulated wedges. *Physics of Fluids*, 14:4315–4328, 2002.

[120] J. Buehrle, S. Herminghaus, and F. Mugele. Interface profiles near three-phase contact lines in electric fields. *Physical Review Letters*, 91(8):86101, 2003.

[121] H. Lomax, T. H. Pulliam, and D. W. Zingg. *Fundamentals of Computational Fluid Dynamics*. Springer, Berlin, 2001.

[122] J. Zeng and T. Korsmeyer. Principles of droplet electrohydrodynamics for lab-on-a-chip. *Lab on a Chip*, 4(4):265–277, 2004.

[123] M. Bussmann, J. Mostaghimi, and S. Chandra. On a three-dimensional volume tracking model of droplet impact. *Physics of Fluids*, 11:1406–1417, 1999.

[124] W. Vegt, H. C. Mei, H. J. Busscher, and W. Norde. ph dependence of the kinetics of interfacial tension changes during protein adsorption from sessile droplets on fep-teflon. *Colloid and Polymer Science*, 274(1):27–33, 1996.

[125] W. van der Vegt, W. Norde, H. C. van der Mei, and H. J. Busscher. Kinetics of interfacial tension changes during protein adsorption from sessile droplets on fep-teflon. *Journal of colloid and interface science*, 179(1):57–65, 1996.

[126] G. Serrien and P. Joos. Dynamic surface properties of aqueous sodium dioctyl sulfosuccinate solutions. *Journal of colloid and interface science*, 139(1):149–159, 1990.

[127] J. Benjamins, J. A. Feijter, MTA Evans, DE Graham, and MC Phillips. Dynamic and static properties of proteins adsorbed at the air/water interface. *Faraday discussions of the Chemical Society*, 59:218–229, 1975.

[128] K. B. Song and S. Damodaran. Influence of electrostatic forces on the adsorption of succinylated. beta.-lactoglobulin at the air-water interface. *Langmuir*, 7(11):2737–2742, 1991.

[129] J. Fukai, H. Ishizuka, Y. Sakai, M. Kaneda, M. Morita, and A. Takahara. Effects of droplet size and solute concentration on drying process of polymer solution droplets deposited on homogeneous surfaces. *International Journal of Heat and Mass Transfer*, 49(19-20):3561–3567, 2006.

[130] R. A. Meric and H. Y. Erbil. Evaporation of sessile drops on solid surfaces: Pseudospherical cap geometry. *Langmuir*, 14(7):1915–1920, 1998.

[131] H. Hu and R. G. Larson. Evaporation of a sessile droplet on a substrate. *The Journal of Physical Chemistry B*, 106(6):1334–1344, 2002.

[132] L. Gao and T. J. McCarthy. Contact angle hysteresis explained. *Langmuir*, 22(14):6234–6237, 2006.

[133] H. W. Lu, F. Bottausci, J. D. Fowler, A. L. Bertozzi, C. Meinhart, and C. J. Kim. A study of ewod-driven droplets by piv investigation. *Lab on a Chip*, 8(3):456–461, 2008.

[134] M. Hoorfar and A. Neumann. Axisymmetric drop shape analysis (adsa) for the determination of surface tension and contact angle. *Journal of Adhesion*, 80(8):727–743, 2004.

[135] A. Bateni, S. S. Susnar, A. Amirfazli, and A. W. Neumann. A high-accuracy polynomial fitting approach to determine contact angles. *Colloids and Surfaces A: Physicochemical and Engineering Aspects*, 219(1-3):215–231, 2003.

[136] X. Fan and G. L. Brown. Probe for measurements of density/conductivity in flows of conducting fluids. *Review of Scientific Instruments*, 77:045104–1–045104–4, 2006.

[137] D. R. Lide. *CRC handbook of chemistry and physics*. CRC press, Internet version, 88th edn. edition, 2008.

[138] N. T. Nguyen and S. T. Wereley. *Fundementals and applications of microfluidics*. ARTECH HOUSE, Norwood, USA, 2nd edn. edition, 2006.

[139] A. Volanschi, W. Olthius, and P. Bergveld. Design of a miniature electrolyte conductivity probe using isfets in a four point configuration. *Sensors and Actuators B: Chemical*, 19(1-3):404–407, 1994.

[140] S. K. Fan, C. Hashi, and C. J. Kim. Manipulation of multiple droplets on n m grid by cross-reference ewod driving scheme and pressure-contact packaging. In *Micro Electro Mechanical Systems, 2003. MEMS-03 Kyoto. IEEE The Sixteenth Annual International Conference on*, pages 694–697. IEEE, 2003.

Appendix A

Contact Angle Measurement

Accurate measurement of microdroplet contact angles is important for characterizing the interfacial properties of microfluidic systems. Different methods have been developed for this purpose. The choice of a particular method depends on the geometry of the system as well as the materials involved. Currently, the most frequently used methods for contact angle measurement are the conventional goniometer method and drop shape techniques, such as Axisymmetric Drop Shape Analysis (ADSA) [134]. In the goniometer method the contact angle is measured by aligning a tangent to the droplet profile at the point where the three phases meet (i.e., at the base of the droplet). The main drawback of the goniometer method is that it is subjective, and the results largely depend on the experience of the operator. In ADSA, an image of a droplet is obtained, and the droplet profile is extracted using image processing techniques. The experimental droplet shape is fitted to the Laplace equation of capillarity which defines the balance between the gravity and interfacial forces applied to an axisymmetric droplet. The contact angle is calculated from the slope of the theoretical curve at the contact point. Although ADSA is widely used and accurate, it is not applicable to a number

of specific systems including non-axisymmetric drops, covered systems, and where an electric field is applied to the droplet. Therefore, ADSA (or other droplet shape techniques) cannot be used for digital microfluidic systems as they can present one or more of these characteristics.

Recently, the automated polynomial fitting (APF) approach has been introduced for the measurment of the contact angles that cannot be obtained using ADSA. The original APF scheme consists of two steps: first, the experimental drop profile is obtained from the image of the drop using image analysis techniques. Then, a polynomial curve is fitted to a part of the experimental profile near the contact point, and the contact angle is calculated using the slope of the theoretical curve. In the APF method, highly magnified images, acquired at the vicinity of the contact points, are used. The camera is slightly tilted to capture the reflection of the droplet. This reflection is required to detect the contact point which is critical for accurate measurement of the contact angle. In the next step, a series of coordinate points are selected, starting at the contact point, and a polynomial is fitted to the selected pixels. Different numbers of points and different orders of the polynomial were examined [135]. A third-order polynomial fitted to 130 points, which resulted in the highest correlation coefficient (R^2), was used for all the images with the Laplacian of Gaussian (LOG) edge detection method. Then, the contact angle was computed from the first derivative of the polynomial at the contact point.

In the present work, the original APF method was enhanced for digital microfluidic contact angle measurements, for which the entire microdroplet profile is desired. This resulted in Canny edge detection which was found to be with greater efficiency compared to LOG in the original APF method. Figure A.1 presents the extracted profiles for two microdroplet images using the Canny method (acquired before and after applying voltage). Different orders of polynomials were examined. The third-order polynomial was also used since it produces the highest correlation coefficient. However, it has been found that the optimum number of points for fitting depends on the pixel to radius ratio and magnification ratio of the microdroplet in the image. Unlike the original APF method, which uses 130 coordinate points for all the images (acquired with different magnifications), the new program calculates the optimum number of the points for every image based on the correlation coefficient which makes the calculation independent from the image resolution and magnification ratio. Figures A.2 (a) and (b) show the steps taken to select the number of coordinate points.

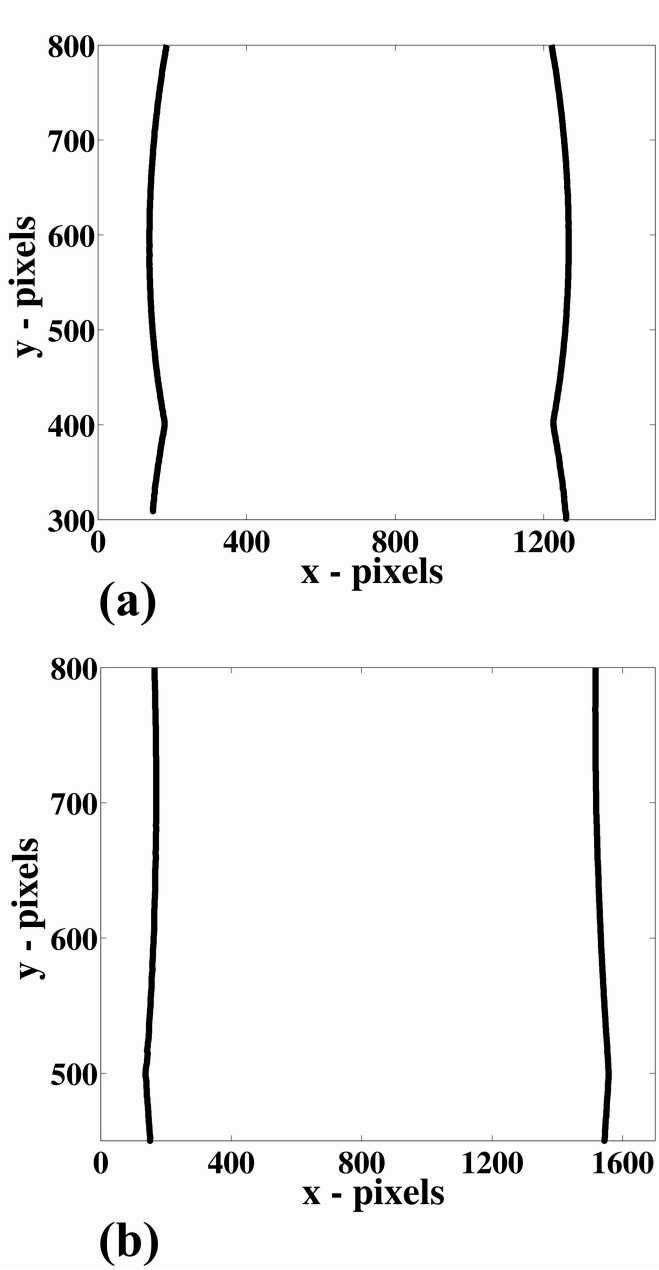

Figure A.1: The extracted profiles for two microdroplet images acquired (a) before and (b) after applying voltage. The Canny edge detection method is used.

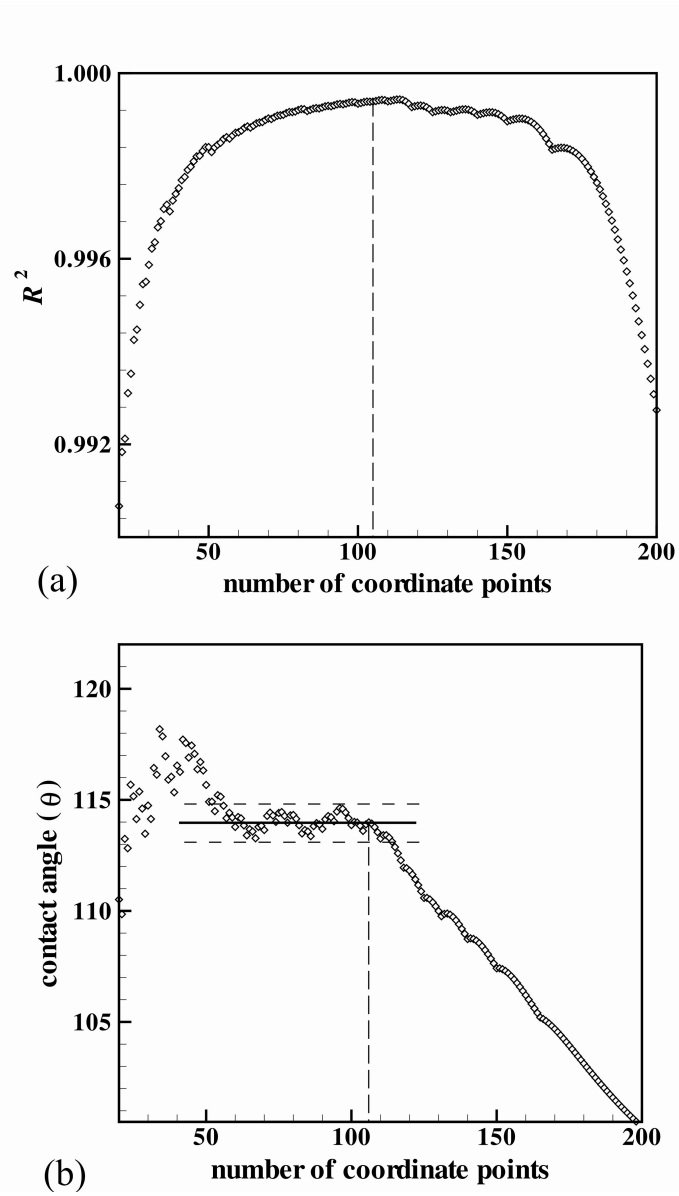

Figure A.2: The (a) number of coordinate points is determined by the maximum value of R^2, and the (b) contact angle is determined for the obtained number of coordinate points.

Appendix B

Conductance Sampling

Conductance sampling provides an inherently sensitive probe to the spatial distribution of conductive fluids in digital structures as its sensitivity is set by the local conductance-per-unit-area. Localized conduction and measurement sensitivity both increase drastically as the ion concentration increases, as changes in conductivity between fluidic states can range by as much as six orders of magnitude (typically varying for fluids from $\sigma = 10^{-5}$ S/m to $\sigma = 10$ S/m [136, 137]). This dynamic range dominates over that of other sampling processes (capacitance sampling for example [138]) as ionic conduction avoids dielectric saturation.

Conductivity sampling has proven to be a particularly useful tool in the characterization and measurement of isolated electrolytic solutions [139]. The technique introduced in this research is equally important for probing the spatial distribution of fluids in a digital microfluidic structure. The key design issue for the proposed system relates to the achievable spatial resolution, since the conductance state under investigation is inherently frequency-independent, and multi-frequency sampling algorithms for probing scales below the structural dimensions are not possible [92]. With this in mind, a digi-

tal multiplexer structure [140] is investigated here. The multiplexer structure incorporates two overlapping and mutually perpendicular linear electrode arrays between which lies the microfluidic control plane. Differential signals are acquired between the m underlying row electrodes (x-electrodes) and overlying n column electrodes (y-electrodes). Such a configuration provides a greatly simplified level of addressability (with only $m + n$ signal inputs) when compared to standard single-layered two-dimensional electrode matrices (with $m*n$ signal inputs). Furthermore, such a system can be more easily scaled down to small electrode widths as the need to independently address numerous individual electrode elements in the two-dimensional grid without crossing, overlapping, or electrical shorting does not apply. A theoretical model for the microdroplet-conductance within such a system is presented here, and a MATLAB-based sampling algorithm is applied to a digital microfluidic multiplexer prototype to verify the proposed technique.

Sampling algorithm

As the underlying fluid dynamics and motion within digital microfluidic multiplexers have been analyzed elsewhere [34], it is the intent here to analyze the capability of these electrical/fluid control structures for sampling of the spatial state of internal microdroplets. A SolidWorks schematic of such a digital microfluidic multiplexer is shown in Figures B.1(a) and (b). The structure is comprised of an underlying x-channel linear electrode array and an overlying y-channel linear electrode array. The orientations of these arrays

are made to be perpendicular, such that (with electrowetting-based systems, for example) x-channel voltages can create net surface tensions on droplets perpendicular to the x-electrodes, and y-channel voltages can create net surface tensions on droplets perpendicular to the y-electrodes. The conductive electrodes are fabricated on insulating substrates and have a width (w) and a periodic centre-to-centre pitch (p) as shown in the figure. This bi-layer configuration is shown magnified in Figure B.1(b).

The multiplexer gap between the electrode arrays forms the region in which microdroplet sampling, actuation, and control can be carried out. The spatially-dependent differential conductance associated with arbitrary fluid distributions are measured using the linear electrode arrays, as the regions of overlap between x- and y-electrodes without electrolyte will exhibit negligible conductance with

$$G_{\min} = 0, \tag{B.1}$$

whereas, the regions of overlap between x- and y-electrodes with electrolyte will exhibit higher levels of conductance. The maximum possible conductance,

$$G_{\max} = \frac{\sigma w^2}{d}, \tag{B.2}$$

is obtained when the fluid fully covers the w^2 area of intersecting xy electrodes. An arbitrary xy multiplexer location will have a conductance varying between these minimum and maximum values, and these conductance values can be used to map out the profile of the microdroplet.

For digital microdroplet routing algorithms it is necessary to have an effective means of extracting both droplet positions and sizes. Such a system is demonstrated here by way of a numerical area-weighting algorithm using circular microdroplet profiles. This simplified system can be characterized by a total of $3N$ parameters for a system of N microdroplets. The algorithm takes as its input the measured two-dimensional discrete conductance distribution G_{xy} and computes an output consisting of each microdroplet's: i. centre (x_0,y_0) location and ii. radius r_0. These quantities are defined here as unitless values on the grid having been normalized with respect to the electrode pitch p. A numerical series sum over all y-channels is executed for each x-electrode conductance, producing a one-dimensional array of the total conductance of each x-channel,

$$G_x = \sum_{y=1}^{n} G_{xy} = \frac{\sigma w}{d} \cdot L_x = G_{\max} \cdot \frac{L_x}{w}. \tag{B.3}$$

Similarly, a numerical series sum over all x-channels is carried out for each y-channel conductance, producing a one-dimensional array of y-channel summed conductances,

$$G_y = \sum_{x=1}^{m} G_{xy} = \frac{\sigma w}{d} \cdot L_y = G_{\max} \cdot \frac{L_y}{w}. \tag{B.4}$$

The total conductance associated with the microdroplet is given by

$$G_t = \sum_{x=1}^{m} G_x = \sum_{y=1}^{n} G_y = G_{\max} \cdot \frac{A_t}{w^2}. \tag{B.5}$$

In these expressions, L_x and L_y, when multiplied by w, give the areas of overlap between the microdroplet and the respective x- or y-electrode, and A_t is the total microdroplet area covering the regions of overlapped electrodes. The numerical execution is simplified by introducing dimensionless and normalized summed conductances defined for each circular microdroplet as

$$g_x = \frac{G_x}{G_{\max}}, \tag{B.6}$$

$$g_y = \frac{G_y}{G_{\max}}, \tag{B.7}$$

and

$$g_t = \frac{G_t}{G_{\max}}. \tag{B.8}$$

Having collected the discrete two-dimensional grid of differential conductances G_{xy} and calculated the normalized summed conductances g_x, g_y, and g_t from this grid, the numerical algorithm is completed with the computation of the microdroplet centre and radius from

$$x_0 = \sum_{x=1}^{m} x \cdot \frac{g_x}{g_t}, \tag{B.9}$$

$$y_0 = \sum_{y=1}^{n} y \cdot \frac{g_y}{g_t}, \tag{B.10}$$

and

$$r_0 = \sqrt{\frac{1}{\pi} \cdot g_t}, \tag{B.11}$$

respectively. The centre location is found here from weighted positional averages of the x- and y-channel normalized summed conductances g_x and g_y, in proportion to the total normalized conductance g_t, and the radius is calculated from the normalized area of the circular microdroplet. As before, locations are defined in terms of unit-multiples of pitch p with integer positions corresponding to the middle of each respective electrode. With these definitions the (x_0,y_0) and r_0 results are recorded as generalized and unitless quantities, as the overlapping electrode area w^2 cancels in the g_t normalization process, and unit-multiples of the pitch p give an effective conducting area of $p^2 = 1$.

Execution of the algorithm described above may be complicated by complexity issues relating to the presence of multiple microdroplets in the system. The algorithm described above incorporates weighted positional averages which, in the presence of multiple drops, will give erroneous intermediate centralized averages. To overcome this, a pre-processing step is added to the algorithm after the collection of the measured two-dimensional conductance grid G_{xy} and before the calculation of conductance sums. In this a priori

step, the nonmonotonic nature of the measured data sets is investigated, and the presence of peaks and troughs in the microfluidic conductance is used as a decisional factor in sectioning the G_{xy} data into separate two-dimensional conductance grids. A G_{xy} grid is created for each individual microdroplet in isolation, and the subsequent algorithm steps are independently applied to each of these microdroplet G_{xy} grids. The complete algorithm is shown in Figure B.2.

The operation of the conductance sampling algorithm is presented in Figure B.3(a) for a hypothetical microfluidic system incorporating two microdroplets. The first microdroplet has a radius of $r_{01} = 5$ and centre at (x_{01},y_{01}) = (22,8), while the second microdroplet has a radius of $r_{02} = 3$ and centre at (x_{02},y_{02}) = (10,30). A cylindrical profile is used to represent the physical microdroplet area in the model, and the theoretical discrete conductance values, G_xy, are calculated for the two-dimensional grid. Each G_{xy} value gives a proportional measure for the degree of microdroplet area overlap at that position, and the resulting discrete conductance distribution is shown. The two G_{xy} grids (each associated with one of the two microdroplets) are then processed by the conductance sampling algorithm, and the weighted positional averages are calculated. The centres and radii of each microdroplet, with (x_{01},y_{01}) = (22,8) and $r_{01} = 5$ for the first droplet and (x_{02},y_{02}) = (10,30) and $r_{02} = 3$ for the second of droplet, are equal to the initial values of these hypothetical microdroplets (within a 2% accuracy). These theoretical model results, shown in Figure B.3(b), are in good agreement with the

initial microdroplet attributes.

Sampling structure

The bottom (x-channel) layer of the constructed digital microfluidic multiplexer structure is shown isolated in the photographs of Figure B.4(a) and (b). The structure is comprised of periodic copper electrodes with a width of $w = 200$ μm and a centre-to-centre pitch of $p = 400$ μm fabricated on an insulating epoxy substrate. The identical top (y-electrode) layer is positioned on top of the bottom layer in a perpendicular orientation with a central gap of $d = 150$ μm separating them. The electrode patterns are designed such that the copper electrode lines transition easily to the copper contact pads. The copper contact pads are made to be of a sufficient length to protrude from the overlapping central multiplexer region, and electrical contacts are established from each contact pad to the electrical sampling system. Conductance sampling is carried out through the measurement of conductance at each differential xy channel pair, and the resulting discrete two-dimensional G_{xy} conductance grid is recorded.

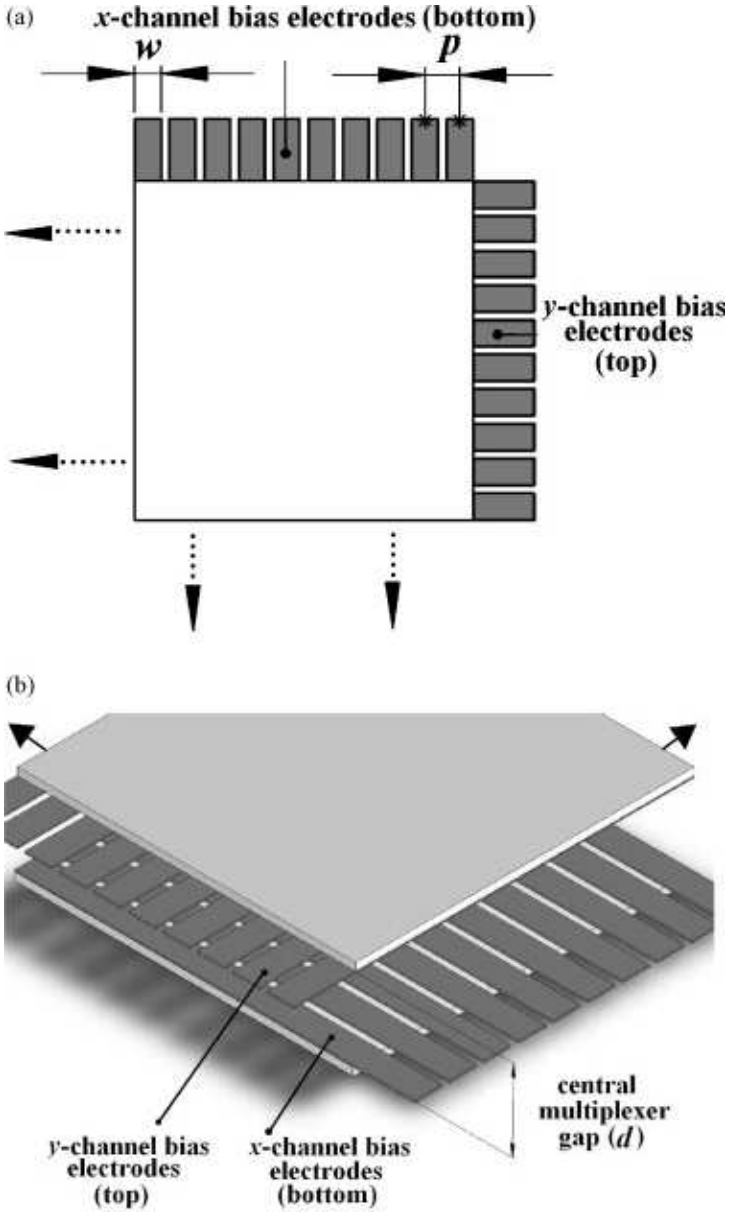

Figure B.1: SolidWorks schematic views of a portion of the proposed digital microfluidic multiplexer design with an (a) orthographic projection and (b) magnified isometric.

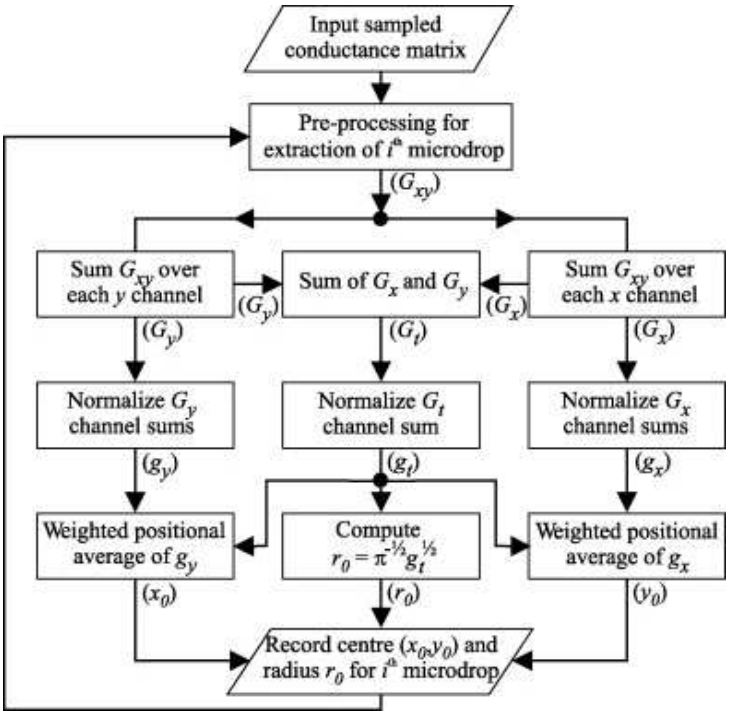

Figure B.2: Flowchart for the employed conductance sampling algorithm.

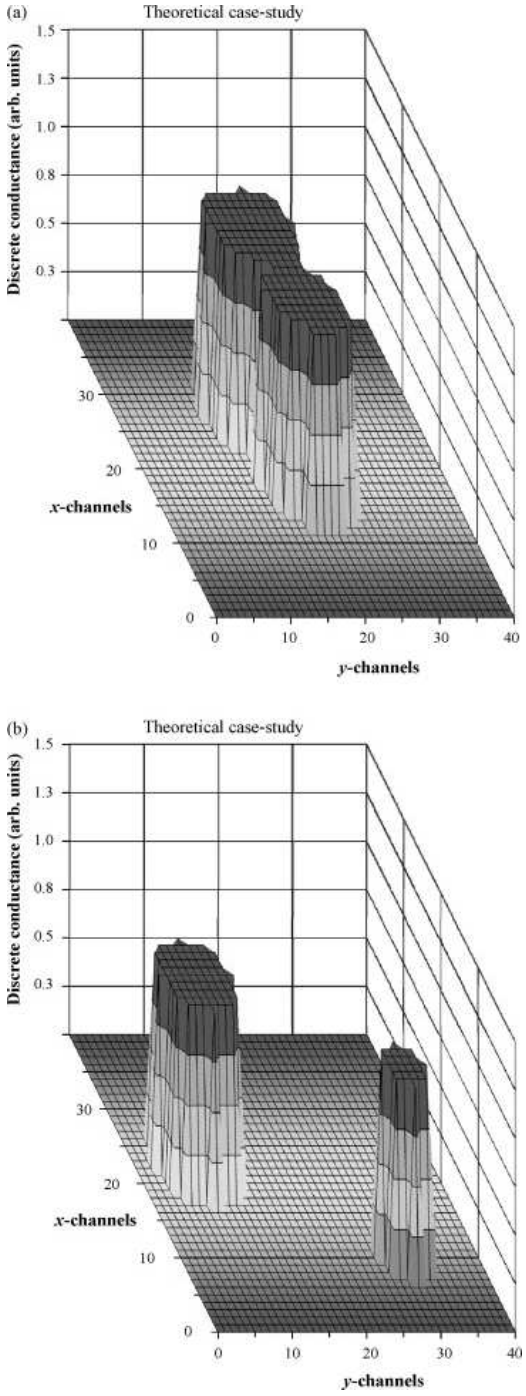

Figure B.3: Theoretical results for hypothetical microdroplet fluid profiles with (a) an arbitrary fluid distribution and (b) two separated microdroplets in the digital microfluidic multiplexer.

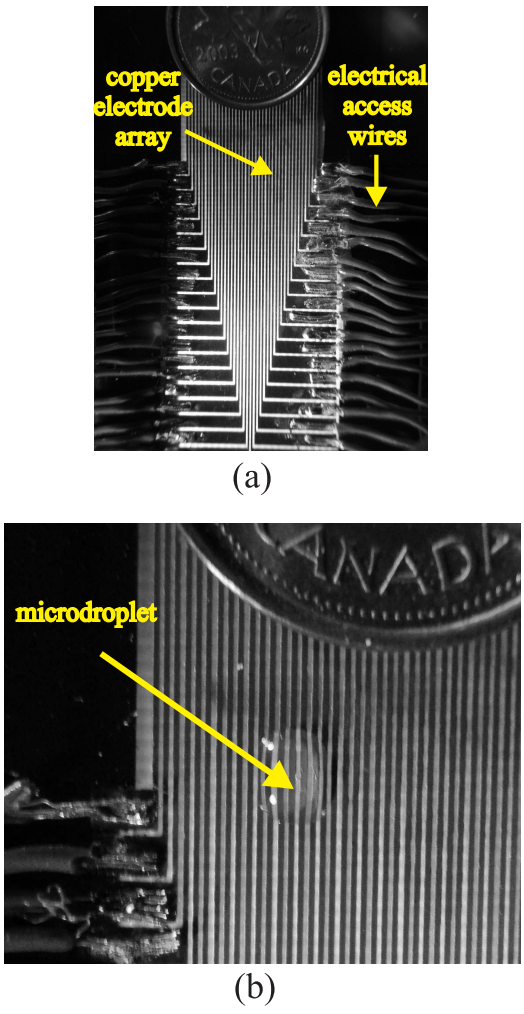

Figure B.4: Photographs of (a) the bottom (x-channel) electrode layer and (b) a microdroplet on this layer.

Conductance sampling results

The conductance sampling process within the digital microfluidic multiplexer is tested first for a system with one microdroplet. The microdroplet is com-

prised of an NaCl electrolytic solution with a 2.8 M electrolyte concentration (with a conductivity measured to be approximately $\sigma = 0.2$ S/m). The microdroplet is dispensed between the perpendicular x- and y-electrode plates, and conductance sampling of the differential G_{xy} combinations is carried out. The discrete experimental sampling results are shown in Figure B.5(a) as a function of x- and y-channel indices. The distribution here shows a definitive nonmonotonic profile at the location of the microdroplet, with conductance values in the two-dimensional array varying from the background minimum value $G_{\min} = 0$ (below the 0.1 μS measurable limit of our apparatus) to the maximum value at the center of the microdroplet, $G_{\max} = 40$ μS. The algorithm introduced in the previous section is then applied to the discrete sampled values, and the normalized summed conductances are used to extract the location and size of the microdroplet. The measured results are shown visually in Figures B.5(b) and (c). The measured microdroplet is characterized by a location of $(x_0,y_0) = (30.0,26.6)$ and a radius of $r_0 = 3.6$, and these experimental results are in qualitative agreement with overhead observations of the investigated microdroplet. As described in the introduction, these overhead measurements are particularly challenging in multi-layered architectures and limited in accuracy due to the presence of the overlying metal electrode array. The conductance sampling process demonstrated here will have an ultimate measurement resolution that is set by the transverse dimensions of the multiplexer structure (ie. the electrode width w and pitch p).

A subsequent investigation is carried out with the proposed conductance sampling method for a system containing two separate microdroplets. The microdroplets are dispensed into the central gap of the digital microfluidic multiplexer, and electrical sampling is carried out to extract the two-dimensional conductance grid G_{xy}. The discrete experimental sampling results are shown in Figures B.6(a)-(c). Nonmonotonic profiles are again exhibited in the regions of the microdroplets shown here, as the conductance values range from a background of $G_{\min} = 0$ to maximum values of $G_{\max1} = 34.5$ μS and $G_{\max2}$ = 40.0 μS at the centres of each of the two microdroplets. The results are pre-processed and separate sampling algorithms are carried out for the microdroplets to give the resulting locations and radii. For the first (lower maximum conductance) microdroplet a centre location of (x_{01},y_{01}) = (9.5,10.5) and radius of $r_{01} = 2.4$ are determined, and for the second (higher maximum conductance) microdroplet a centre location of (x_{02},y_{02}) = (17.4,10.8) and radius of $r_{02} = 2.6$ are determined. As was the case for Figure B.5, the experimental results here are in qualitative agreement with overhead imaging observations, though the challenges of imaging through the top metal electrode array (being a major motivation for this work) again limit the accuracy of these visual observations.

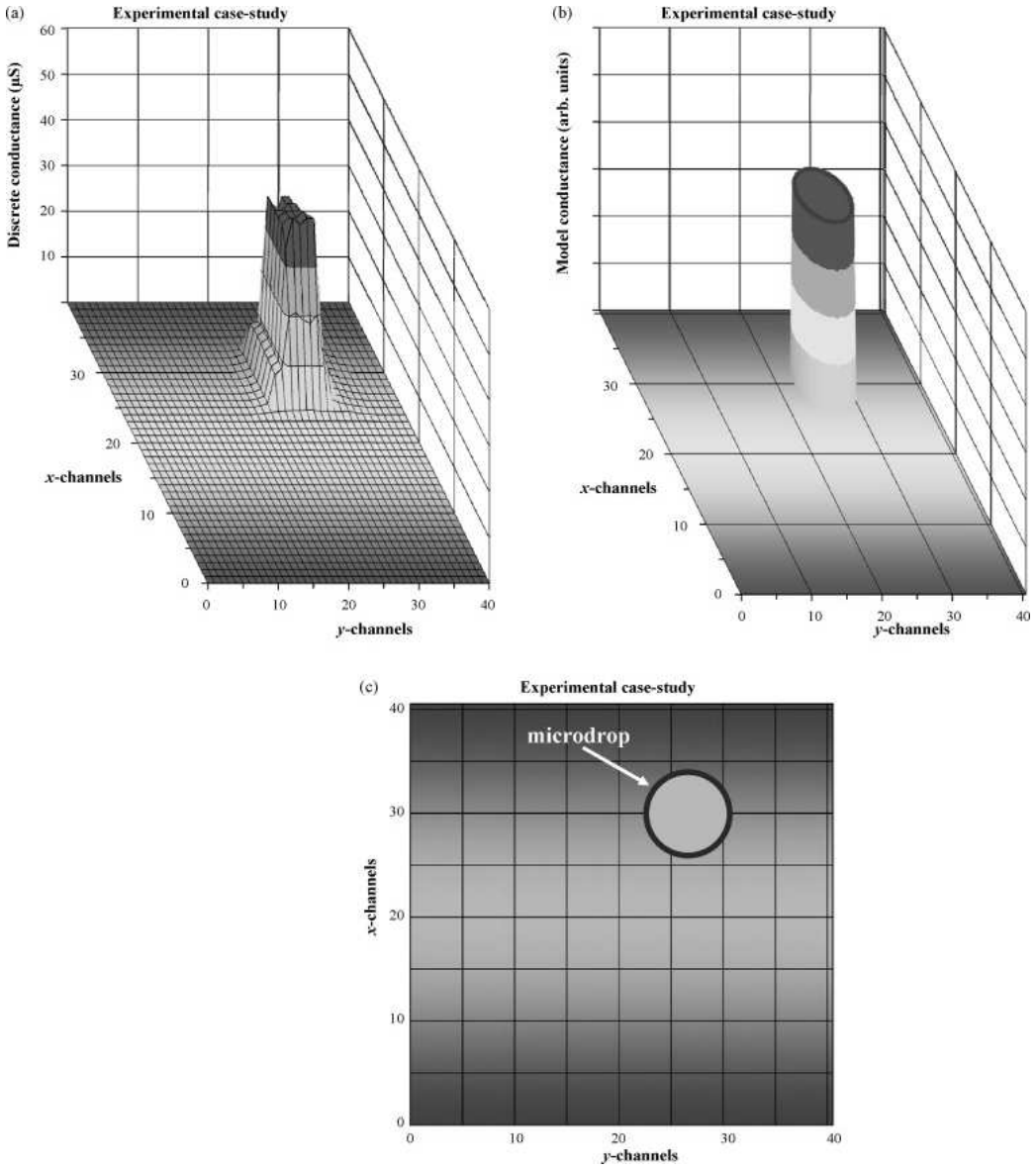

Figure B.5: Experimental results for a single microdroplet within the digital microfluidic multiplexer as a (a) discrete conductance surface, (b) extracted microdroplet model surface, and (c) extracted microdroplet model overhead view.

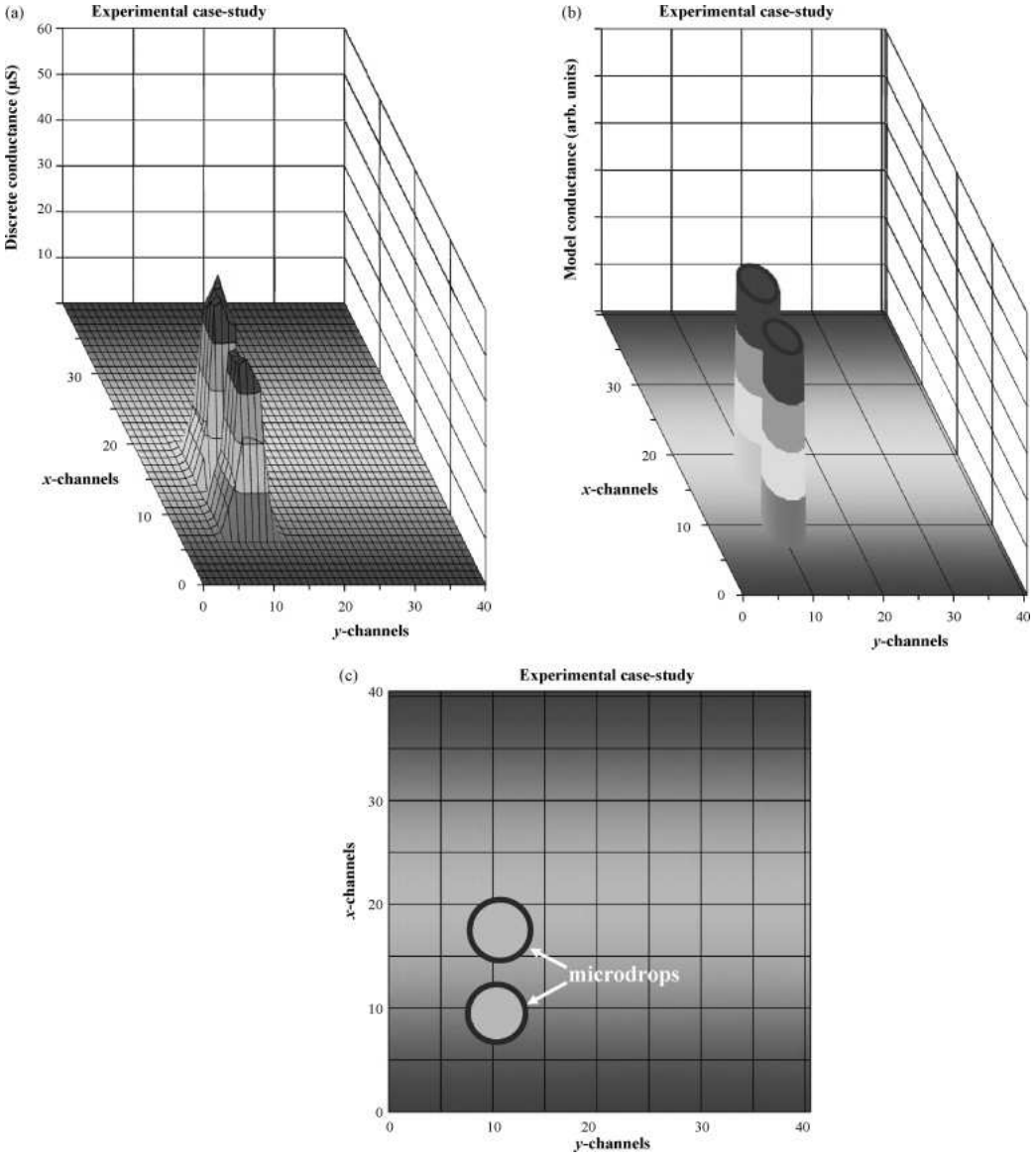

Figure B.6: Experimental results for two microdroplets within the digital microfluidic multiplexer as a (a) discrete conductance surface, (b) extracted microdroplet model surface, and (c) extracted microdroplet model overhead view.